INTERFACE FRACTURE CHARACTERIZATION AND AN IMPROVED MULTIPHYSICS MODEL FOR RECHARGEABLE BATTERIES

By

Akshay Shailendra Pakhare

A DISSERTATION

Submitted to
Michigan State University
in partial fulfillment of the requirements
for the degree of

Mechanical Engineering—Doctor of Philosophy

2023

ABSTRACT

The capacity and energy density of the current rechargeable batteries are not sufficient to meet the future energy storage demands. One of the strategies to solve this issue is to replace the existing electrode material with high performance materials. The commercial electrodes are composites which consist of active material particles (that are responsible for energy storage), a polymer binder with conductive additives which holds all the particles together and provides electrical network. Both the negative (i.e., anode) and positive (i.e., cathode) electrodes are composites. Graphite is the conventional active material in the anode, and the high performance materials such as Si, Sn, Ge are being considered as a replacement for graphite due to their energy density. For example, Si offers nearly 10 times more capacity compared to graphite (i.e., 3579 mAh/g compared to 372 mAh/g). However, these high-performance materials exhibit poor cyclic performance and undergo significant capacity fade, i.e., reduction of usable capacity with cycling. To address these issues, the dissertation has two broad goals: 1) to develop novel experimental methods for interface fracture characterization in batteries and 2) to develop a comprehensive multiphysics model for rechargeable batteries.

Capacity fade occurs in batteries mainly due to two different mechanisms: chemical and mechanical processes. The chemical process involves loss of active ions due to irreversible reaction resulting in the formation of a passivation layer called the solid electrolyte interphase (SEI). The mechanical process involves fracture of active material particles or failure of the interface between binder and active material particles. In this work, the focus is on the mechanical process and especially the failure of binder/active material interfaces in the negative electrode (i.e., anode). Although the binder/active material interfaces exist in both anode and cathode, large volume changes of anode materials make the interface failure a critical issue for anodes. For example, the most promising next generation anode material Si undergoes nearly 270% volume change during electrochemical cycling. This level of volume change causes interface failure and loss of electrical network in the electrode resulting in capacity fade. In spite of its importance, there is a lack of understanding on the interface failure in rechargeable batteries. In this study we developed a novel

experimental method to characterize the interface failure behavior in lithium-ion battery system. Specifically, PVdF polymer was used as a binder and Si as active material in this model system. Samples for fracture characterization were prepared by depositing PVdF on Si substrate followed by a series of nanofabrication processes. The blister test samples fabricated in this process were tested in a novel electrochemical cell in conjunction with an in-house optical system based on Michelson interferometer principle. The samples were pressurized until the PVdF film delaminated from Si substrate. The mechanical response of the pressurized film was measured, and the PVdF/ Si interface fracture was characterized in terms of critical energy release rate Gc. The effect of thermal oxide (i.e., SiO₂) on the interface failure behavior was investigated. Further, the same setup was used to determine the effect of galvanostatic electrochemical cycling of Si on the interface failure behavior.

The significant volume change behavior of the next generation high-performance materials during electrochemical cycling can generate stresses as high as 1 GPa. These high stresses in high-performance material undergoing large deformation affects the diffusion of ions in active material particle, affects the voltage of a battery, and also affects the electrochemical kinetics at the electrode/electrolyte interface. Theoretical models are necessary to develop high energy density and durable batteries for future energy storage demands. The current battery models account for the stress-potential coupling but assume steady state electrochemical kinetics. However, transient electrochemical kinetics are required to capture rate dependent electrochemical behavior usually observed in batteries during operation, i.e., when current is drawn at various rates during discharge process of a battery. Also, the existing models were developed based Li-ion batteries, and there is a need to extend the models to other battery systems (i.e., other chemistries such as Na-ion). Therefore, we have developed a theory for Li-ion and Na-ion electrode active materials. A diffusion-deformation model with transient electrochemical kinetics was developed and implemented in a finite element package.

By combining the experimental and modeling tasks outline above, this dissertation successfully characterized and simulated the failure behavior of binder/active material interface.

Copyright by AKSHAY SHAILENDRA PAKHARE 2023

ACKNOWLEDGEMENTS

For this journey of Ph.D. dissertation I would acknowledgement the contribution for many. Firstly I would like to give deepest gratitiude my advisor and mentor Prof. Siva Nadimpalli without him nothing would be possible especially his support during transition from universities (NJIT to MSU) and during pandemic. His constant encouragement allowed me to explore various areas and gain new knowledge for this I am indebted for him. I would also give my gratitude to my mentors Dr. Vijay Sethuraman and Dr. Shawn Chester for their support, advice and guidance throught my Ph.D. My thanks also goes to my collaborators Dr. Amir Ameli and Dr. Karun Kalia for allowing my to work with them on new areas. I also thank my Ph.D. committee Prof. Thomas Pence, Dr. Ricardo Mejia-Alvarez and Dr. Joerg Petrasch for their evaluation, feedback and guidance.

The Ph.D. program in would not have been possible without my lab mates seniors Dr. Rajasekhar Tripuraneni and Dr. Subhajit Rakshit during my early days of Ph.D. for their support in studies, guidance and living in a new country. My lab mates Igor Bezsonov, Abdulrahman Alfadhali, Martina Borges, and Dr. Amit Chanda for their support during experimentation, their valuable feedback and support outside lab was immense. I am thankful to them and the work would not be possible. My colleagues form Dr, Shawn Chester group, Dr. Shuolun Wang, Dr. Nikola Bosnjak, Dr. Suman Jaiswal, and Keven Alkhoury for the guidance and support in exploring the computational area. Their company made me feel like home.

The dissertation work would not have been possible without guidance from Dr. Jorge Barreda at Lurie Nanofabrication lab (Univ. of Michigan) for his guidance in micro and nanofabrication process. Also, my thanks to Dr. Per Askland at composite material science center at MSU who helped my immensly with the material characterization process.

The Ph.D. program would not have been possible with support for my parents Mr. Shailendra Pakhare, Mrs. Anuradha Pakhare, and my sister Ms. Sneha Pakhare and their constant encouragement and love from family and I would like to dedicated this dissertation to them.

TABLE OF CONTENTS

LIST OF TA	ABLES v	⁄ii
LIST OF FI	GURES	ix
CHAPTER 1.1 1.2 1.3 1.4	1 INTRODUCTION	1 1 3 6 9
CHAPTER		
		11
2.1	1 1	11
2.2	- 1 1	13
2.3		14
2.4		19
2.5	Experimental Setup and test procedure for interface failure under electrochemical condition	24
CHAPTER	3 INTERFACE FAILURE RESULTS UNDER DRY CONDITIONS	28
3.1	Mechanical response and crack tip condition of PVdF/Si samples	28
3.2		31
3.3	Characterization of PVdF/SiO ₂ Interface Failure	33
3.4	=	37
3.5	Effect of thermal oxide on the adhesion of PVdF to Si	39
3.6		41
3.7	Conclusion	44
CHAPTER		
4.4		47
4.1	, e	47
4.2 4.3	Effect of electrolyte on the pressure-deflection and interface failure behavior	47 51
4.3	* *	53
CHAPTER	5 MODELING THE CONSTITUTIVE BEHAVIOR OF ELECTRODES .	56
5.1		5 6
5.2		66
5.3		68
5.4		76
5.5	•	77
CHAPTER	6 CONCLUSION AND FUTURE PLAN	80
6.1	Conclusion	80

6.2	Future	Work		 •			 		•	•			•			•	 •	84
BIBLIOGR	APHY																	90

LIST OF TABLES

Table 2.1	Mechanical properties of materials used in finite element simulation	23
Table 3.1	The chemical composition in at% on the PVdF film, bare Si surface and on the fracture surface of PVdF/Si	32
Table 3.2	The pressure at the onset of delamination and the corresponding critical energy release rate (G_c) values of PVdF/SiO ₂ interface measured from seven circular blister tests. As this is a mixed-mode fracture property, the phase angle ψ_G corresponding to these measurements is 43^o	38
Table 3.3	Energy release rate (G_c) for all circular samples measured along with crack initation pressure	38
Table 3.4	Composition at Various interfaces	39
Table 3.5	Comparision of critical pressure value of rectangular PVdF films on SiO_2 substrate measured from experiments and the from the FE predictions using $G = G_c$ failure criterion	44
Table 5.1	Material parameters for Na-Ge calibration.	72
Table 5.2	Material parameters for Li-Ge calibration	75

LIST OF FIGURES

Figure 1.1	Ragone plot showing Specific Energy and Specific Power for different battery chemistries [1]	1
Figure 1.2	Shows of a composite lithium ion battery	3
Figure 1.3	a) The reduction in capacity with cycle number i.e. capacity fade of a Si composite electrode[2], b) Schematic of SEI formation mechanism on the surface of an electrode[3] c) Fracture of a 100 nm Si thin electrode due to electrochemical cycling. The channel cracks are formed due to large tensile stress 1 GPa that was developed during electrochemical cycling[4]	4
Figure 1.4	Show the schematic of interface between a-Si (amorphous silicon) and electrolyte interface with an intermediate solid electrolyte interface (SEI) layer formed due to degradation of electrolyte(The dotted line between electrolyte and SEI is shown for clarity). The charge distribution at the interface between a-Si and electrolyte forms a double layer	8
Figure 2.1	a) Schematic of the PVdF/Si sample showing various system parameters, b) the sample preparation process, and c) axisymmetric sample with 1200 μ m diameter for PVdF/Si interface fracture property (G_c) measurement	12
Figure 2.2	a) Schematic of the PVdF/SiO ₂ sample showing various system parameters, b) the sample preparation process, and c) axisymmetric sample with 1000 μ m diameter for PVdF/SiO ₂ interface fracture property (G_c) measurement	15
Figure 2.3	Showing the Pressure vs Time when test cell was kept at 250 KPa showing leak free clamping	16
Figure 2.4	a) Schematic of the experimental setup for characterization of binder/active material interface fracture, and b) the details of the interferometer used for the measurement of out-of-plane displacements of pressurized PVdF film. The synchronization of data from the pressure transducer and images obtained from the camera enable identification of the critical pressure at the onset of delamination.	17
Figure 2.5	a) An axisymmetric sample with typical interference pattern formed on the surface is shown prior to delamination where the symbol 'x' indicates a pixel (at the center of the circular region) chosen for further analysis, and b) shown the sample after some delamination of PVdF from SiO ₂ surface, with a portion of delamination or crack front highlighted with a dotted-line for clarity	18
	of detailment of elack from inglingmed with a dotted line for elacity	10

Figure 2.6	Intensity of the pixel (or point) indicated as 'x' in Fig.2.5a is plotted as a function of time during the experiment. The triangle symbol (corresponding to intensity peaks) represent the out-of-plane deflection of the point 'x' as a function of time. In this example, the total out-of-plane displacement is 2.75 µm (as 10 peaks passed the point in 200 s)	20
Figure 2.7	The Mises stress magnitude as function of radial distance where the stress goes to zero within 100 μ m of radial distance	21
Figure 2.8	Finite element mesh and boundary conditions of the blister test sample. The inset shows the mesh details near the crack tip and a typical contourd used to evaluate J-integral	22
Figure 2.9	a) Shows the setup of electrochemical cell to lithiate the Si and form LixSi at the interface. The sample prepared according to section 2.1 is adhered using epoxy a 2 mm thick stainless steel plate (not shown here) and the plate is adhered to the electrochemical cell. A celgard separators is placed above the sample and lithium counter/reference electrode is placed above to provide the Li+ ion flux. b) The same electrochemical cell is used for interface fracture test where the celgard separator and lithium foil is removed. During interface fracture test Ar is introduced to induce interface fracture	25
Figure 2.10	Typical pressure-central deflection (in blue) of a sample along with sample stiffness $\frac{dw_0}{dP}$ (in black). The red x marks the crack initiation point which is obtained from the minimum of $\frac{dw_0}{dP}$	27
Figure 3.1	a) Prescribed pressure loading on the PVdF film on Si substrate. (the critical pressure associated with onset of delamination is indicated with "x"). b) The Pressure-Central Deflection of the PVdF film from a typical sample of PVdF/Si (blue open circles) along with FE simulation	28
Figure 3.2	a) The crack front propagation identified by contrast difference between PVdF and Si (Note: the scale bar on bottom right is $200 \mu \text{m}$). b) Shows the schematic showing crack extension (δa) and corresponding change in central deflection (ΔW_0) due to crack extension	29
Figure 3.3	The plot of ratio of Pressure-deflection plotted against deflection square show that the y-intercept can be used to obtain the residual stress in the film provided that the film is flat and behaves elastically during the experiment	30
Figure 3.4	The energy release rate (G_c) for axisymmetric and plane strain sample obtain using J-integral in FE simulation at the crack initiation point. The slight difference is due to phase angle which for plane strain is higher compare to axisymmetric	32

Figure 3.5	(a) The profile of circular PVdF film measured under zero applied pressure, (b) the cross section of free-standing PVdF film obtained by FIB milling, (c) prescribed pressure loading on the film (the critical pressure associated with onset of delamination is indicated with "x"), (d) comparison of experimentally measured film profiles at various levels of pressure with those obtained from finite element analysis, and (e) comparison of pressure-central deflection response (p-wo) of the film measured from experiments and those obtained from analytical and finite element models	34
Figure 3.6	Schematic of multibeam optical sensor setup (MOSS) showing the method the to measure residual stress. The residual stress is measured by recording the curvature of the 2-in Si wafer before and after PVdF deposition	35
Figure 3.7	Deformed mesh of the circular membrane at the critical pressure is shown along with the equivalent (von Mises) stress contour near the center of the film (inset on the left side) and the equivalent plastic strain near the crack tip (inset on the right side). This confirms that the PVdF film remains nominally elastic prior to onset of delamination, i.e., existence of small scale yielding conditions	36
Figure 3.8	Scanning electron microscope backscatter image of the fracture surface (i.e., surface after free standing PVdF delaminated from SiO2). The table shows the atomic weight fractions of elemental C, O, F, and Si obtained from the XPS analysis showing nearly identical stoichiometry of bare SiO2 and delaminated region (with some fluorine on the surface)	40
Figure 3.9	Comparison of the energy release rate obtain through finite element by J-integral for PVdF/Si and PVdF/SiO ₂ interface	40
Figure 3.10	a) Show the Raman spectroscopic analysis of Si surface (dash dot blue) and SiO ₂ (dashed black line) surface where the peak at 975 cm ⁻¹ corresponds to Si-OH group. The relative intensity comparisons show that the concentration Si-OH is higher on SiO ₂ compared to Si. The b) and c) are the XPS spectra focusing on O1s peak conducted on bare Si (solid blue) and SiO ₂ (dashed black) surface. Here the Si-OH peak (at 533 eV) deconvoluted from the O1s peak of survey scan is and compared for both Si and Si surface. The figs. d) and e) are the schematic showing the likely mechanism of adhesion between PVdF binder to Si surface with native oxide, and thermal oxide SiO ₂ on Si surface.	42
Figure 3.11	Rectangular PVdF film sample prepared following the fabrication process outlined above	43
Figure 3.12	(a) The initial profile of rectangular sample (b) Comparing the obtained total deflection to finite element simulation and analytical solution	44

Figure 4.1	a) shows the potential vs time of a typical PVdF/Si sample subjected to electrochemical cycling. The inset shows an enlarged region of Potential-Time curve at 0.25 h showing undercooling effect which indicates phase formation. b) Shows the top view of actual PVdF/Si sample after being subjected to lithiation. c) Schematic showing the lithiaition of (100) Si sample.	48
Figure 4.2	a) Shows the pressure-time behavior of a typical axisymmetric (dashed blue) and plane strain (dotted black) sample subjected to pressure due to argon. (b) The pressure-central deflection response of the typical axisymmetric sample (dashed blue) and FE simulation (dashed dot curve). c) The pressure-central deflection response of a typical plane strain same (dotted curve) along with FE simulations.d)Shows the schematic of the sample after failure where the presence of electrolyte at the interface affects propagation. e) An actual axisymmetric sample which shows crack initiation	50
Figure 4.3	a) show the axisymmetric and plane strain energy release rate of electrolyte soaked PVdF/LixSi interface. b) The comparison of energy release rate of soaked PVdF/LixSi interface with dry PVdF/Si showing that soaking of electrolyte and lithiating Si reduces weaken the interface	52
Figure 4.4	a) show the axisymmetric and plane strain energy release rate of electrolyte soaked PVdF/LixSi interface. b) The comparison of energy release rate of soaked PVdF/LixSi interface with dry PVdF/Si showing that soaking of electrolyte and lithiating Si reduces weaken the interface	53
Figure 4.5	a) Shows that PVdF is likely to bond to via. van der walls forces of attraction, the polymer chain bonds to the -OH (hydroxyl) radicals present on Si surface. b) Here we present a simplified macroscopic representation of PVdF polymer chains attached to Si substrate. c) When PVdF absorbs electrolyte, is swells and polymer chains are redistributed. The swelling also causes interfacial stress at the surface which decreases the adhesion strength. The uptake of electrolyte which contains constituent such as EC, DC, and DMC which are polar and non-polar solvent can affect the charge distribution at the interface. d) Due to electrochemical reaction at the interface, the Li ions diffuse into Si and intercalates to form alloy of Si i.e. LixSi complete saturation of Si forms Li3.75Si. The interface can get roughened due to formation of diffusion pathways also at the interface due to decomposition of electrolyte, SEI forms at the interface which degrades the interface between swollen PVdF binder and LixSi interface	54
Figure 5.1	Comparing True Stress vs True Strain at 3 different normalized concentration (\bar{c}) a) 0.025 b) 0.1 c) 0.5 with data from 1-D Matlab and single element U3D8 at $\dot{\epsilon} = 0.001$	67
Figure 5.2	Comparing True Stress vs True Strain at 3 different strain rate($\dot{\epsilon}$) a) 0.001 b) 0.01 c) 0.1 with data from 1-D Matlab and single element U3D8 at $\bar{c} = 0.5$	67

Figure 5.3	UEL and 1D diffusion equation	69
Figure 5.4	hows the mesh to simulate the thin film in-situ stress experiment	70
Figure 5.5	Calibrating the Model to experimental data a) True stress vs time and b) True stress vs Capacity for Na-Ge	71
Figure 5.6	Calibrating the Model to experimental data a) Voltage vs time and b) Voltage vs Capacity for Na-Ge	72
Figure 5.7	Calibrating the Model to experimental data a) True stress vs time and b) True stress vs Capacity for Li-Ge	74
Figure 5.8	Calibrating the Model to experimental data a) Voltage vs Time and b) Voltage vs Capacity for Li-Ge	75
Figure 5.9	Shows the a) Voltage vs time, b) Voltage vs Capacity, c) True Stress vs Time, and d) True stess vs capacity for Li-Ge. Here the dotted black curve is the experimental data, solid black is the simulation with the side reaction and dash dotted curve shows the simulation without side reaction. The inclusion of side reaction allow to match the capacity, account for charge lost, and capture potential change during OCP	77
Figure 5.10	Shows the a) Voltage vs Capacity, b) Stess vs Capacity, c) Voltage vs Time, and d) stress vs time during OCP for Li-Ge. Here we compare the effect of double layer capacitance on potential and stress. The double layer capacitance allows to capture accurately the shape of potential and stress during galvanostatic flux change.	78
Figure 6.1	(a) shows the rectangular plane strain sample of PVdF thin film on Si substrate (b)Shows the Pressure-time curve of a rectangular PVdF thin film (750 nm) (c) show the corresponding pressure-central deflection during the loading and unloading (d) show the stress and plane strain in the central deflection region where the red line is a linear fit to the stress-strain during unloading	86
Figure 6.2	(a)Shows the schematic of rechargeable battery with composite electrode. The inset shows the zoomed in view of a binder attached to Si particle. The inset is a FE mesh representing the quarter of the particle with symmetry boundary conditions.(b)Actual active material particle with binder[5]	87
Figure 6.3	Typical traction separation relation with linear softening.	88

Figure 6.4	(a)Show the potential vs time evolution of the single active material particle	
	with PVdF binder Fig.7.1 subjected to galvanostatic lithiation and delithiation	
	(b) Show the corresponding damage evolution (D) at three different points on	
	the potential-time curve	89

CHAPTER 1

INTRODUCTION

1.1 Rechargeable batteries and associated challenges

Rechargeable batteries play a key role in automotive, defense, aerospace, and biomedical applications due to their ability to store and deliver energy on demand. Lithium ion batteries (LIBs) are the primary choice as energy storage devices owing to their high energy and power density compared to other battery chemistries as shows in Fig. 1.1. LIBs have seen exponential growth in recent years due to sustainability and clean environment goals of US and many other countries. As a result of the increased demand and dwindling lithium metal reserves, cost of LIBs is increasing. This has prompted an intense focus on the development of other battery chemistries such as Na-ion, Mg-ion, Al-ion, Li-air etc. The development of LIBs and other chemistries is driven by the goal of enhancing energy and power density. In the case of LIBs, one of the strategies being pursued at the moment is to replace conventional electrode materials with high performance alternatives. This approach poses several challenges that needs to be addressed. In this chapter, a brief background of LIBs is presented first along with the challenges associated with replacing conventional materials, and finally we state the objectives of this research.

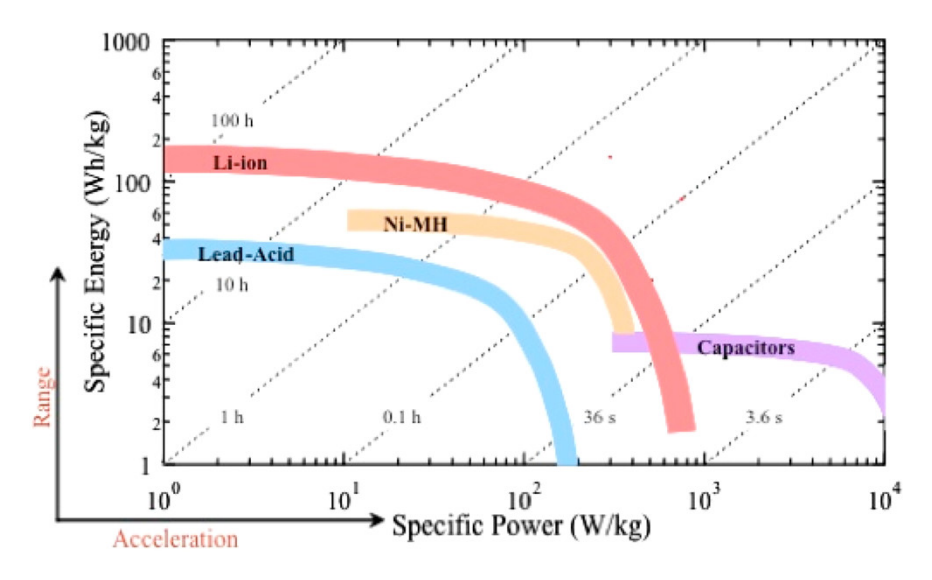


Figure 1.1 Ragone plot showing Specific Energy and Specific Power for different battery chemistries [1].

The commercial Li-ion batteries consist of four main components: (1) anode, (2) electrolyte, (3) cathode, and (4) separator as shown in 1.2. The electrolyte consists of a salt of a Li-ion (e.g., 1 M lithium hexafluorophosphate (LiPF₆) dissolved in non-aqueous solvents such as ethylene carbonate(EC), diethyl carbonate(DEC), dimethyl carbonate DMC) and provides the pathway for ion transport between electrodes. The positive ion (e.g. Li⁺) move between cathode and anode via. the electrolyte during charge and discharge process while electrons move through the external circuit. The separator (typically a thin membrane made of polymer) physically separates the two electrodes to prevent electrical short circuit between them.

The commercial Li-ion battery electrodes (i.e. anode and cathode) are composites consisting of a mixture of active material particles bonded together by polymeric binder as shown in Fig. 1.2. Typically, a polymeric material such as polyvinylidene fluoride (PVdF) or carboxymethyl cellulose (CMC) is used as a binder, and conductive additives (carbon black) are added to it to impart electrical conductivity. To fabricate electrodes (anode and cathode shown in Fig.1.2), the mixture of binder and active particles (graphite particles in anode and LiCoO₂ particles in cathode) is cast onto a sheet of current collector (Cu for anode and Al for cathode). It can be noted from Fig. 1.2 that the conductive binder network between the particles provides the means for electron transfer throughout an electrode.

The specific capacity of the state-of-the-art anode material, i.e., graphite, is 372 mAh/g. This however, does not meet the requirement of the current and future energy storage demands of electric vehicles, where capacities of 2 to 5 times higher are required [6]. One way to achieve this is to replace graphite with high performance electrode materials such as Group IV elements (viz. Sn, Si, Ge). For example, replacing Si with graphite increases the theoretical capacity of LIB by more than 30% [7]. This is because the theoretical capacity associated with Li_{3.75}Si formation is 3569 mAh/g[7], i.e., when Li reacts with Si during electrochemical cycling, which is 10 times higher capacity than that of graphite. One of the main roadblocks preventing the widespread use of Si or other high-performance electrode materials is their poor cyclic life, i.e., rapid the capacity fade during cycling[8, 9].

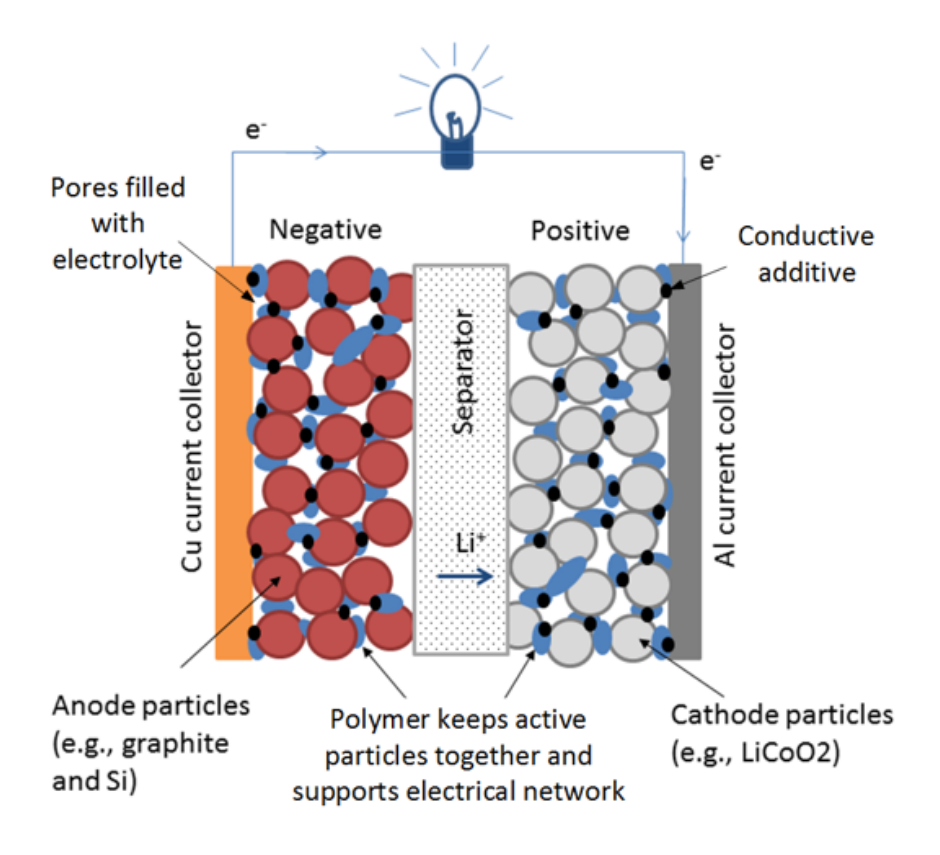


Figure 1.2 Shows of a composite lithium ion battery.

1.2 The challenge of interface failure in batteries

Capacity fade is defined as the decrease in the capacity of a battery after multiple charge-discharge cycles; Fig. 1.3a shows the capacity fade in a Si composite electrode. Capacity fade occurs due to chemical and mechanical processes that occur during battery operation. In the chemical process, a passive layer called solid electrolyte interphase (SEI) forms on fresh electrode surfaces and consumes the available lithium in the electrode [10]. Fig.1.3b shows the schematic of SEI formation process which occurs when electrolyte solvent reacts with active Li ion and an electron from conductive surface such as the active particles. As the passive SEI layer becomes too thick, it impedes the Li⁺ ion transport and the associated SEI formation reactions on the surface of the anode.

Besides the chemical process, mechanical degradation becomes an important capacity fade mechanism for new higher performance electrodes due to their large volume change behavior [11]. For example, upon reacting with Li, Si active material (particle, film, or nanotube) expands by

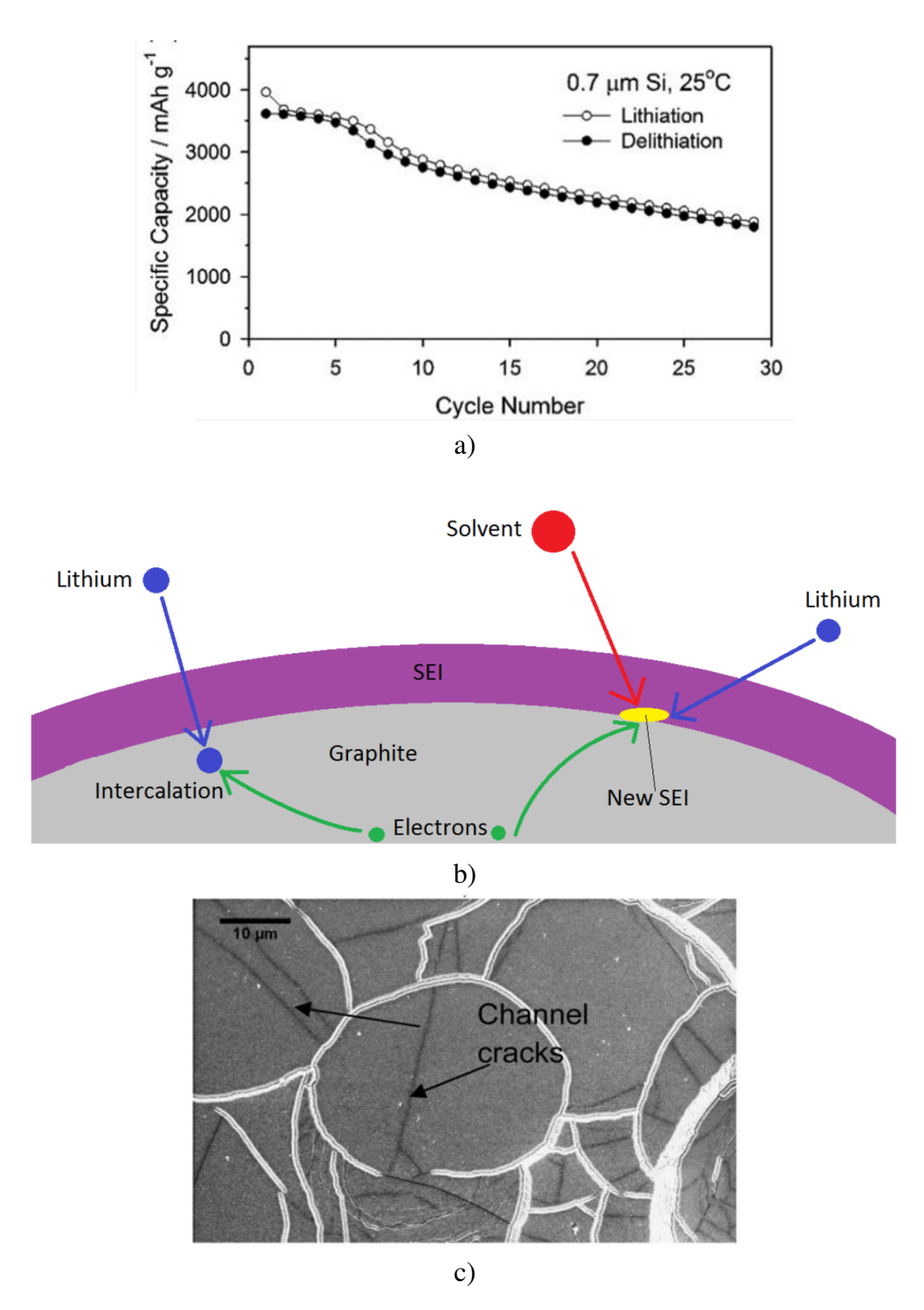


Figure 1.3 a) The reduction in capacity with cycle number i.e. capacity fade of a Si composite electrode[2], b) Schematic of SEI formation mechanism on the surface of an electrode[3] c) Fracture of a 100 nm Si thin electrode due to electrochemical cycling. The channel cracks are formed due to large tensile stress 1 GPa that was developed during electrochemical cycling[4].

more than 300% [12]. This level of expansion when constrained generates significant amount of stress in the lithiated Si. Sethuraman et al.[13] found that the stress level in Si thin film could be as high as 1.5 GPa when reacting with Li. Similar stress magnitudes have been observed for Sn [14], Ge [15, 16] and for Ge anodes in Na ion battery [?]. This level of electrode stresses will eventually lead to fracture of electrodes (particles and thin films) Fig. 1.3c [4, 17] or the failure of polymer binder/particle interfaces [18]. The fracture of Si thin film anode has been studied by Nadimpalli et al. [4] and Pharr et al [17]. However, the fracture of polymer binder/active material interface, which is responsible for electrical network in the electrode, has not been studied before in a systematic way. This thesis will focus on the failure of the polymer binder/active material interface.

In a composite electrode, the polymer binder not only holds the particles together but it provides electrical network necessary for sustaining chemical reactions [8, 19, 20, 21, 22, 23, 9]. When the stress level at the active material/binder interface reaches a limit, the binder delaminates from the surface of active particle causing electrical isolation of particles, which leads to capacity fade. The electrical isolation of active particles due to polymer/active particle interface failure is one of the leading mechanisms of capacity fade. For a battery to operate successfully, a strong and stable polymer/active material interface is needed and is critical for achieving longer cyclic life of batteries.

Studies on composite electrodes [24, 18, 8, 19, 25, 26, 27, 28] showed that a stronger bonding between binder and active particles (i.e., a stronger binder/active material interface) improved the cyclic performance of the electrodes. Similarly, in situ stress measurements in composite electrodes by Sethuraman et al., [28] demonstrated, experimentally, that polyvinylidene fluoride (PVdF) binder, when used in Si-based composite electrodes, showed poor cyclic performance compared to carboxymethyl cellulose (CMC), and it was attributed to the nature of bonding. Hence, understanding the interface failure behavior of battery electrodes is critical for improving the durability of high-performance battery electrodes.

In spite of the importance, very few studies [25, 28, 29] exist on the binder/active material

interface failure and all of them are qualitative in nature. For example, scratch tests [24, 30, 31], and peel test [8, 32, 33, 34, 35] can only provide relative ranking of interface strength and do not measure fundamental mechanical properties that can be used to predict the failure of the interfaces under other configurations or loading conditions. More recently, Müller et al.[36] carried out X-ray imaging of composite electrodes to understand the interface degradation mechanisms. However, a systematic study on the direct measurement of fundamental mechanical property that characterizes the interface failure in battery electrodes is still missing. The challenges associated with measurements on micro or nanoscale samples (typical dimension of binder bridges in composite electrodes) and the lack of mechanical characterization of active materials [37, 38, 39, 28] and polymer binders [40, 22, 26, 27, 41] until recently, could be one reason for the lack of systematic study on the interface failure characterization. Therefore, in this study our objective is to experimentally characterize as prepared and cycled Si/polymer binder interfaces failure.

1.3 Multiphysics model for designing high performance electrodes

A comprehensive multiphysics model that can account for damage in electrodes is essential for durable and high energy density electrode designs. This is due to the strong coupling between electrochemical and mechanical phenomena in the next generation electrode materials such as Si. For example, it was observed that a 1 GPa of stress in (Si) electrode could change the voltage of the electrode by 0.64 V vs. Li/Li+ [42]. Similarly, stress also affects the solid state diffusion of ions; Tripuraneni et al.[43], observed that the diffusion of Li-ion was enhanced under tensile stress and was impeded under compressive stress. Battery models should be able to account for this strong coupling between mechanical and electrochemical phenomena.

Some of the earliest battery models to include stress were developed by [44, 45, 46]; there were able to study the fracture of linear elastic electrode particles. Analytical model for single particle electrodes were developed by [47], and later they extended the model to large volume changing electrodes [48]. Models were also developed for nanowires which included surface energy and surface stress [49], cohesive zone mode for thin film fracture [50], and multiscale model which included microscopic (e.g. particle-particle interaction) and macroscopic effects(e.g.

electrochemical kinetics, deformation) [51, 52, 53]. However, all these models assumed that the electrodes are linear elastic materials, which is a plausible assumption for cathode materials (e.g. LiCoO₂) or anode materials such as graphite which expand only few percent upon cycling [54, 55] and not for high performance future electrode materials, especially negative electrode materials.

The large volume expansion group IV elements undergo extensive plastic deformation [4, 17, 13, 56, 57]. Plastic deformation of electrodes contributes to energy losses, and Sethuraman et al. showed that, for thin film electrodes, it is nearly 50% of total battery losses for amorphous Si electrode and similar observations have been made for Ge electrodes in Li and Na-ion batteries [39]. Hence, it is important to model the plastic deformation of electrode materials. In addition, the battery models need to account for diffusion in the volume expanding materials as the recent high-performance electrode expand nearly 300%. Therefore, a model with coupled diffusion and large deformation kinematics which can also treat plasticity of electrode particles is needed to design durable and efficient electrode microstructures.

The coupled diffusion and large deformation models in literature which include plasticity were developed by Bower et al. [58, 59, 60, 61] and Anand et al.[62, 63]. In addition to treating the plasticity of electrode particles, their formulation includes a stress-potential coupling, which was numerically implemented in a finite element framework. For example, in their formulation, the chemical potential of the electrode is a function of the stresses in the electrode. The stress and potential are obtained simultaneously in this formulation as they influence each other, resulting in proper mechanical and electrochemical coupling which previous models lack. Although this is a major advancement in the electrochemo-mechanical modeling of energy storage materials, these models did not include transient kinetics at the electrode particle/electrolyte interface, i.e., the effect of double layer is not considered in these models.

A double layer of charge exists at the electrode particle/electrolyte interface due to the accumulation of charged particles [64] as shown in the schematic Fig. 1.4. The behavior of this electric double layer is similar to that of a capacitor. The charged particles setup up a capacitance which controls the charge transfer reaction, i.e., ions entering/leaving electrolyte or electron enter-

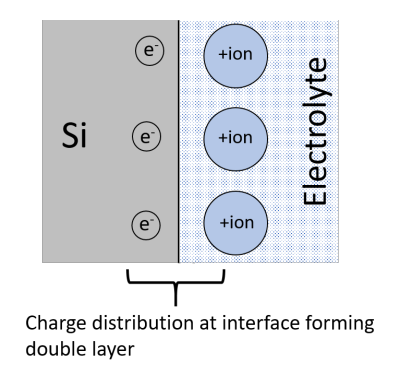


Figure 1.4 Show the schematic of interface between a-Si (amorphous silicon) and electrolyte interface with an intermediate solid electrolyte interface (SEI) layer formed due to degradation of electrolyte(The dotted line between electrolyte and SEI is shown for clarity). The charge distribution at the interface between a-Si and electrolyte forms a double layer.

ing/leaving the electrode. This capacitance buffers any sudden change in potential or current and provides a smoother transition to any step changes in potential or current and imparts a transient nature, i.e., time dependent behavior, to the interfacial kinetics.

The lithiation/delithaition reaction, i.e., redox(reduction-oxidation) reaction is governed by Butler-Volmer kinetics which describes the relation between the current and the potential difference between active material particle and the electrolyte. Similarly, Tafel kinetics which govern the current for loss reaction i.e. SEI formation is also related to the potential difference. The current and potential difference in both Butler-Volmer and Tafel kinetics are exponentially related allowing it to be numerically solved. Except Bucci et al. [61], numerical implementation of steady state electrochemical kinetics was not observed in large deformation theory.

Here we implement a simple double layer capacitance model relating the current associated with double layer charging to the rate of change of potential; the proportionality constant will be the double layer capacitance. A similar description was used by [65, 66]. This implementation will allow accurate prediction of the potential and stress evolution in electrodes even when the battery is not being charged or discharge, i.e., under open circuit condition. This model being developed will describe the potential change during open circuit potential which was neglected in large deformation electrode models. Further, most of the existing models, i.e., large deformation kinematics coupled with diffusion and electrochemistry was developed based on lithium-ion battery

electrode materials. Since there is significant need for the advancement of rechargeable batteries with other chemistries including Na-ion, Mg-ion, S-ion etc., we not only implement the transient kinetics to the existing models but extend the model to sodium ion battery electrodes.

1.4 Objectives of the thesis

The two major objectives of this work are:

- 1. Provide a framework for experimental characterization of interface failure between binder/active material interface.
 - a) Develop a new optical setup based on interferometry principle to measure deflection and identify fracture in real-time.
 - b) Design and fabricate new electrochemical cell design to enable measurements.
 - c) Design and fabricate novel interface fracture samples.
 - d) Develop testing methodology and overcome all the challenges associated with it.
- Develop a continuum mechanics model for coupled diffusion-deformation and electrochemical behavior of high energy density rechargeable battery electrodes. This objective will be achieved with the following tasks.
 - a) Formulate a coupled diffusion-deformation and electrochemical theory.
 - b) Numerically implement the theory in ABAQUS finite element software. This will involve developing new user element subroutine (UEL) for axisymmetric, plane-strain and 3D elements.
 - c) Verification of the code with solutions based on classical diffusion theories and largedeformation plasticity theories.
 - d) Calibration of the finite element code with two different battery chemistries (Na-Ge and Li-Ge systems) to prove robustness.

The rest of the document is organized as follows. Chapter 2 explains interface fracture characterization methods with the description of sample fabrication, electrochemical cell assembly, experimental setup, and finite element and analytical analysis. Chapter 3 and 4 Describes the results and observations of interface fracture experiments. Chapter 5 describes theoretical formulation, numerical implementation, verification, and calibration. Chapter 6 describes the conclusion and future work.

CHAPTER 2

EXPERIMENTAL METHOD TO CHARACTERIZE THE INTERFACE FAILURE

In this chapter, we will describe the procedure to prepare interface degradation samples, an experimental setup constructed to measure delamination, and procedure to obtain energy release rate.

2.1 PVdF/Si Sample Preparation

To characterize PVdF/Si interface failure, a sequence of micro and nanofabrication processes shown in Fig. 2.1b were used to fabricate the samples. First, a single side polished (100) Si wafer (4 in diameter, 550 µm thickness) was rinsed with acetone and isopropyl alcohol to remove any contaminants on the surface and BHF (Buffered Hydrofluoric acid) dipped to remove any surface oxide. This transition from hydrophilic to hydrophobic nature was shown by the water droplets which confirms the removal of oxide. The 4 in wafer was then spin coated with a uniform solution of 10 wt% PVdF (Polyvinylidene fluoride) in NMP (1-Methyl-2-pyrrolidone) at 600 rpm for 30 s using a spin coater (VTC-100 A, MTI Corp.) and dried at 100°C for 8 hrs. in vacuum oven to obtain a 6.8 ± 1.232 µm PVdF film on the Si surface. This process was performed on polished side of the wafer.

Using a standard photolithography process (Karl Suss MA/BA6 mask aligner) and SPR220 photoresist, a circular (1000 µm diameter) patterns were created on rough side of the wafer. The exposed circles were etched using Si using Deep Reactive ion etching (DRIE) to create a trench 500 µm deep. This was followed by through etching using XeF2 to create a free-standing area of PVdF film. The two-step etching process was conducted so the DRIE plasma does not attack the PVdF film also, PVdF is known to be passive against XeF2. The Wafer was cleaned using DI water to remove any contaminants. Note, acetone and Isopropyl alcohol clean was avoided for cleaning due to film wrinkling and delamination. Since the PVdF film is translucent, a 100 nm Cu was sputter deposited on the lower surface of PVdF, also seen in Fig. 2.1c, to enable light reflection and optical measurements.

The interface fracture sample prepared (fig. 2.1c) shows two distinct regions in free standing

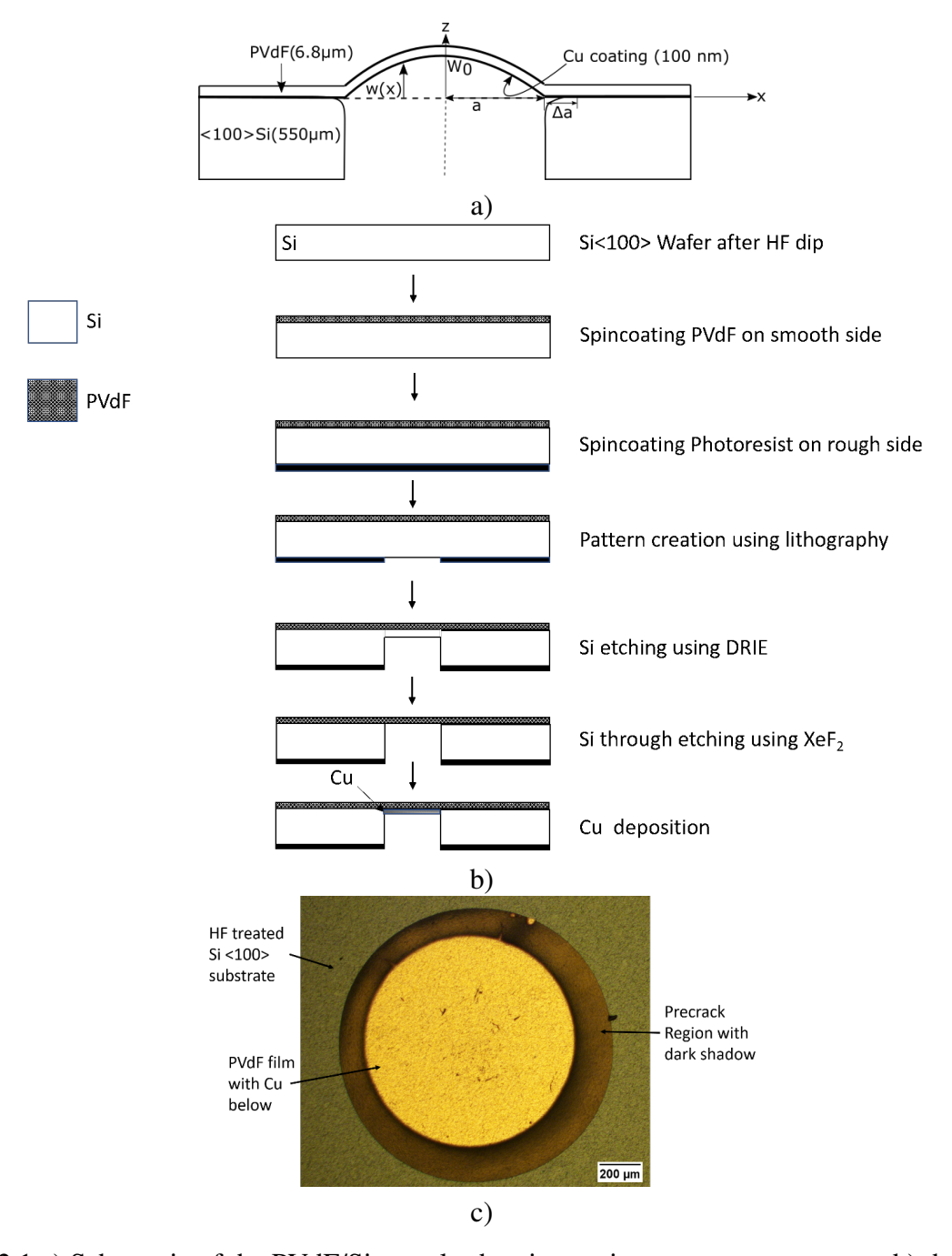


Figure 2.1 a) Schematic of the PVdF/Si sample showing various system parameters, b) the sample preparation process, and c) axisymmetric sample with 1200 μ m diameter for PVdF/Si interface fracture property (G_c) measurement.

area of the film a bright region surrounded by a dark ring. The bright region is illuminated by the Cu beneath the film and the dark region is a region below PVdF where there is no Cu deposited. The dark region exists on top of the Si surface where there is a microscopic gap present between PVdF film and Si surface i.e. the dark region is referred as the pre-crack and is represented as Δa in Fig. 2.1a. A focused ion beam cut (FIB) of the sample verifying the presence of pre-crack. The pre-crack formation occurs during XeF₂ etching as the sample is subjected to excess exposure time to remove any remnant Si below PVdF. During this process, etching occurs in x-direction along with z-direction as XeF2 is an isotropic etch process unlike DRIE which is anisotropic where the etch rate in z-direction is significantly higher than x-direction. A sample with pre-crack is ideal for interface failure investigation allowing crack to propagate at the interface.

2.2 PVdF/SiO₂ Sample Preparation

Figure 2.2a shows a schematic of the interface fracture sample which consists of a uniform thin film of PVdF bonded to SiO₂ surface, and the schematic in Fig. 2.2b shows a sequence of micro and nanofabrication processes used to fabricate the samples. An optical micrograph of the actual (axisymmetric or circular) sample is shown in Fig. 2.2c. First, a single side polished Si wafer (4 in diameter, 550 µm thickness) with a 500 nm of thermally grown SiO₂ layer was rinsed with acetone and isopropyl alcohol to remove any contaminants on the surface. Using a standard photolithography process (Karl Suss MA/BA6 mask aligner) and SPR220 photoresist (MegapositTM), a circular (1000 µm diameter) pattern was created on the rough side of the wafer. The exposed circular areas of SiO₂ were etched using inductively coupled plasma-reactive ion etching (ICP-RIE, SPTS Technologies) to remove the oxide; this was followed by through etching of Si using deep reactive ion etching (DRIE, SPTS Technologies) to create the trench below free-standing area of the film. After these etching steps, the samples were thoroughly cleaned with acetone, isopropyl alcohol, and nanostrip (a stabilized mixture of sulfuric acid and hydrogen peroxide) to remove any organic residue on surface of SiO₂ (on the polished side of the wafer) that will be bonded to PVdF.

A uniform solution of 10 wt% PVdF in NMP (1-Methyl-2-pyrrolidone) was spin coated on the

free-standing SiO2 surface at 600 rpm for 30 s using a spin coater (VTC-100 A, MTI Corp.) and dried at 100° C for 1 hr to obtain a 6.0 ± 1.0 µm PVdF film on the SiO₂ surface. The free standing SiO2 film supporting the PVdF was removed using reactive ion etch (or RIE etch, Nordson March RIE-1701) to create a free standing PVdF film as shown in Fig. 2.2c. Since the PVdF film is translucent, a 130 nm Cu was sputter deposited on the lower surface of PVdF, also seen in Fig. 2.2c, to enable light reflection and optical measurements.

2.3 Experimental setup and test procedure

Figure 2.4a shows the schematic of the experimental setup which consists of four components: 1) blister test cell, 2) pressure transducer, 3) mass flow controller, and 4) an interferometer. All these components are controlled and monitored by a computer via a LabView program; the program controls the sensors, records the data, acquires images, and synchronizes the data with images obtained during fracture test. The samples (prepared as per section 2.2 and shown in Fig. 2.2) were placed in the custom-made blister test cell and clamped with gaskets above and below the sample to prevent leak. The current cell design and clamping method produced a leak free cell up to a pressure of 250 kPa (Fig.2.3), which is significantly higher than the critical pressures expected in the current experiments.

The free standing PVdF film was pressurized using ultra-high purity Ar gas through an orifice located below the freestanding film area as shown in Fig. 2.4a. A constant mass flow rate of $0.8 \text{ cm}^3/\text{min}$ (SCCM) of Ar gas was maintained throughout the test using a mass flow controller (Alicat MC-1SCCM-D) which can control the flowrate to within 1% of the setpoint value. This mass flowrate resulted in a constant 0.43 kPa/min of pressure loading on the PVdF film during the test. The pressure in the test cell chamber was measured using a pressure sensor (Omega PX309-050a5v) with a resolution of 1 kPa. The pressure on the film was increased monotonically until the film completely delaminated from the SiO₂ surface. Images of the pressurized film were captured (using an optical system with a 5μ m resolution) at an interval of 400 ms throughout the test. The pressure value corresponding to a 50 μ m (of crack) delamination is considered as the crack initiation pressure (Pc). Figure 2.5b shows an example of a delaminated zone observed in

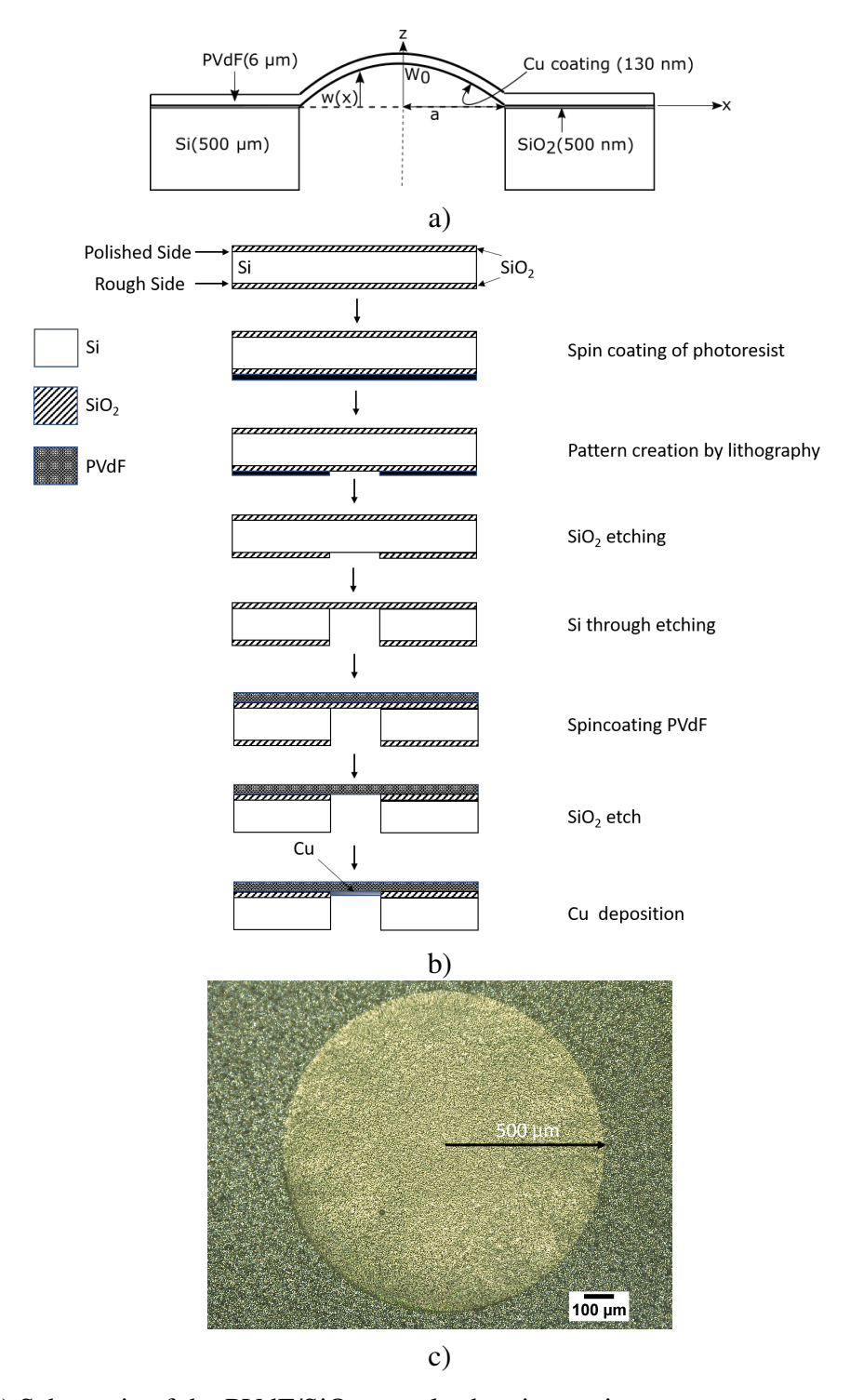


Figure 2.2 a) Schematic of the PVdF/SiO₂ sample showing various system parameters, b) the sample preparation process, and c) axisymmetric sample with 1000 μ m diameter for PVdF/SiO₂ interface fracture property (G_c) measurement.

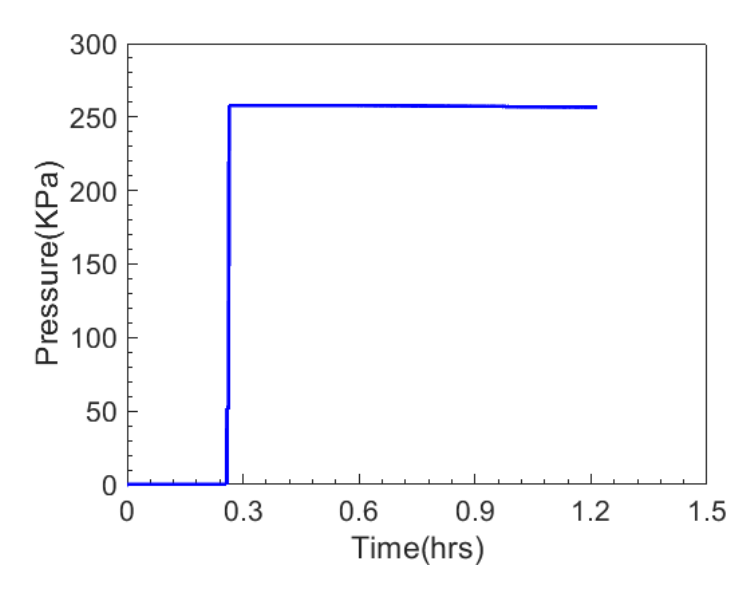


Figure 2.3 Showing the Pressure vs Time when test cell was kept at 250 KPa showing leak free clamping.

axisymmetric sample. For clarity, the boundary between intact region and delaminated region is highlighted with a dotted line.

In addition to pressure, the deflection profile of the PVdF film was measured throughout the test using the interferometer setup that was designed and fabricated in-house. The setup is based on the Michelson interferometry principle and Figure 2.4b shows the details of the interferometer. A green light spectrum with 550 nm ± 10 nm wavelength was employed, and it was obtained by passing white light through a bandpass filter. A combination of collector lens and condenser lens was used to produce a collimated beam of green light (whose light ray remains parallel) and an even illumination of the sample. A beam splitter directs the collimated beam towards a 2x Mitutoyo objective as shown in Fig. 2.4b. The objective was selected to have a field of view big enough to see the full sample and have enough working distance to accommodate optical and sample clamping components. A second beam splitter, located between the objective and the sample, splits the light beam into two and directs one towards a fixed reference mirror and the other towards the sample surface. The reflected beams from the sample and the fixed standard (flat) mirror create an interference pattern due to the slight variations in the optical path lengths travelled by the two beams. Fig. 2.5a shows typical interference patterns formed on an axisymmetric sample. The

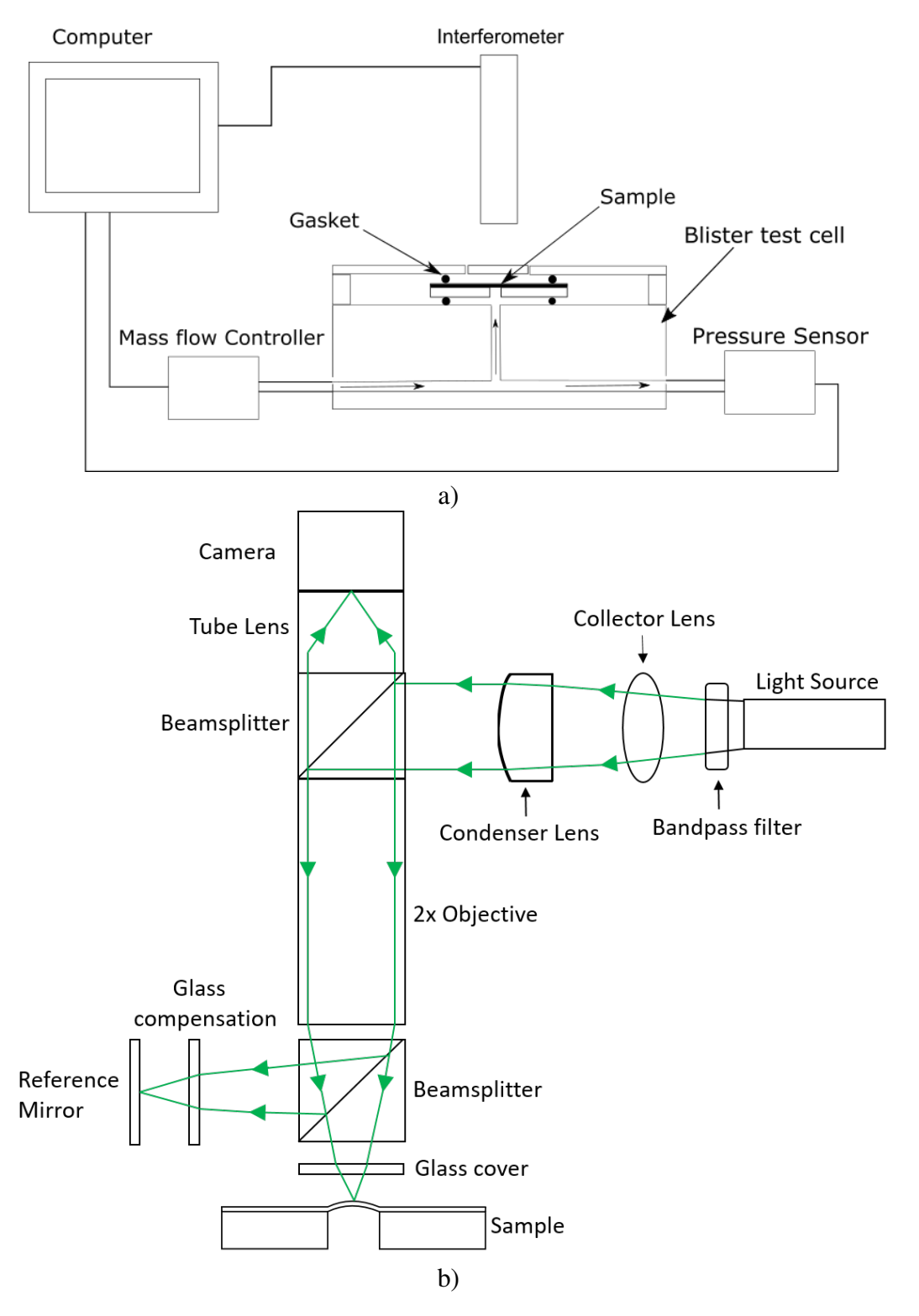


Figure 2.4 a) Schematic of the experimental setup for characterization of binder/active material interface fracture, and b) the details of the interferometer used for the measurement of out-of-plane displacements of pressurized PVdF film. The synchronization of data from the pressure transducer and images obtained from the camera enable identification of the critical pressure at the onset of delamination.

images of the interference pattern are recorded using a CMOS-based monochromatic camera (2MP Basler ace, Edmund Optics Inc.). As the coherency length of the light used is small, it would be difficult to produce interference pattern if the optical path lengths of the beams (travelling from sample surface and the standard mirror) deviate significantly. As a result, a glass window was placed at the reference mirror (see Fig.2.4b) with the same thickness and refractive index as that of the window near the sample surface to balances the optical path lengths.

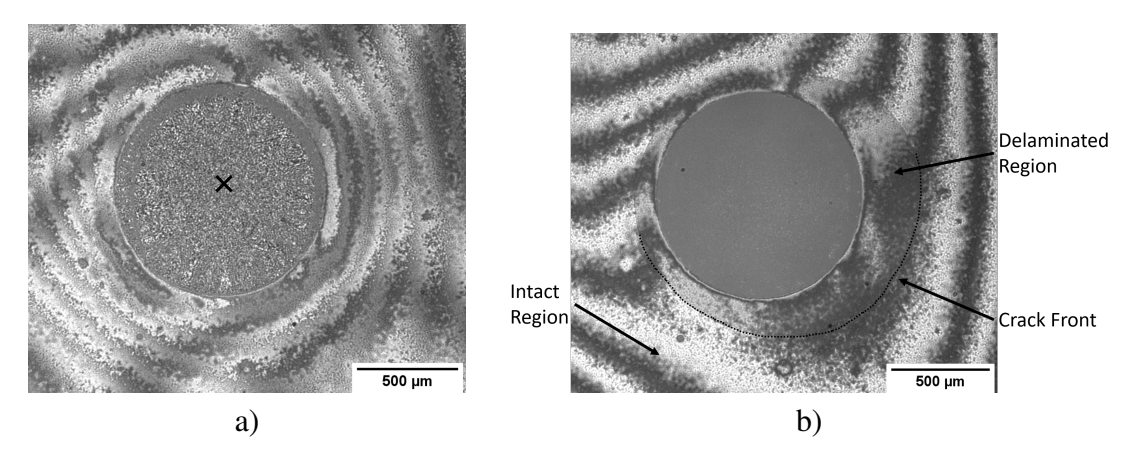


Figure 2.5 a) An axisymmetric sample with typical interference pattern formed on the surface is shown prior to delamination where the symbol 'x' indicates a pixel (at the center of the circular region) chosen for further analysis, and b) shown the sample after some delamination of PVdF from SiO₂ surface, with a portion of delamination or crack front highlighted with a dotted-line for clarity.

The displacement profile of the pressurized PVdF film was obtained by analyzing the interference patterns recorded at a regular interval of 400 ms during a test. A typical interference pattern formed on the samples can be seen in Fig. 2.5a. The passage of each fringe (i.e., the center of one bright (dark) fringe to the next bright (dark) fringe) is equal to 275 nm of an out-of-plane displacement of sample surface, i.e., half of the wavelength of the green light used in the setup (i.e., Fig.2.4b). Hence, in principle, the height profile of the sample surface or pressurized PVdF film at any given time can be obtained by simply counting the number of fringes from the edge of the free-standing area to the center. Such a fringe counting method has been previously used to obtain out-of-plane displacements [67, 68, 69], and it works well for specularly reflective surfaces for which fringe patterns are clear and regular (such as the PVdF/SiO₂ interface in Fig. 2.5a).

However, rough diffuse surfaces might complicate the fringe counting method; for example, the fringe pattern formed on free-standing PVdF area (i.e., the circular region in the middle) is not well defined. Hence, fringe counting method to obtain spatial displacement profile is relatively more challenging.

Due to this challenge, a slightly modified method was implemented to analyze the fringe patterns to obtain the displacement profile of the pressurized PVdF film. Instead of counting number of fringes formed on the entire surface area of the free-standing PVdF film, number of fringes passing a given point on the sample was counted. For example, the intensity of each pixel such as the one indicated with "x" in Fig.2.5a was obtained as a function of time throughout the test by analyzing all the images of a particular test with an image processing code written in Matlab software. Fig. 2.6 shows the normalized intensity as a function of time of the pixel (or the point) indicated as "x" in Fig. 2.5a. The normalized intensity is the ratio of intensity recorded to the maximum intensity (which for a 8 bit image is 256). The intensity reaches a peak every time a fringe passes the point; hence, the number of peaks in Fig 2.6 represent the number of fringes that passed the point 'x' in 200s, which is equal to an out-of-plane displacement of 2.75 µm (i.e., 10 X 275 nm). The filled triangle symbol represents the out-of-plane displacement of the point 'x' as function of time. It should be noted that the resolution of the system shown in Fig. 2.4 is $\lambda/4 = 137.5$ nm, i.e., peak to valley distance. With this procedure, one can obtain out-of-plane displacement of each point on the sample surface during the experiment, even if there are no well-defined and clearly identifiable fringes as seen on the free-standing PVdF surface Fig.2.5a, i.e., on the circular area.

2.4 Theoretical Methods

2.4.1 Finite Element Analysis

Abaqus finite element (FE) software [70] was used to simulate the mechanical behavior of pressurized PVdF film and the PVdF/SiO2 interface fracture. It should be noted that the deformation behavior of pressurized films consists of small strain but large rotations [?]; hence, NLGEOM ON option in Abaqus that simulates the large deformation kinematics was prescribed. Figure 2.8 shows the finite element mesh (of sample in Fig.2.2) along with the boundary conditions of the PVdF

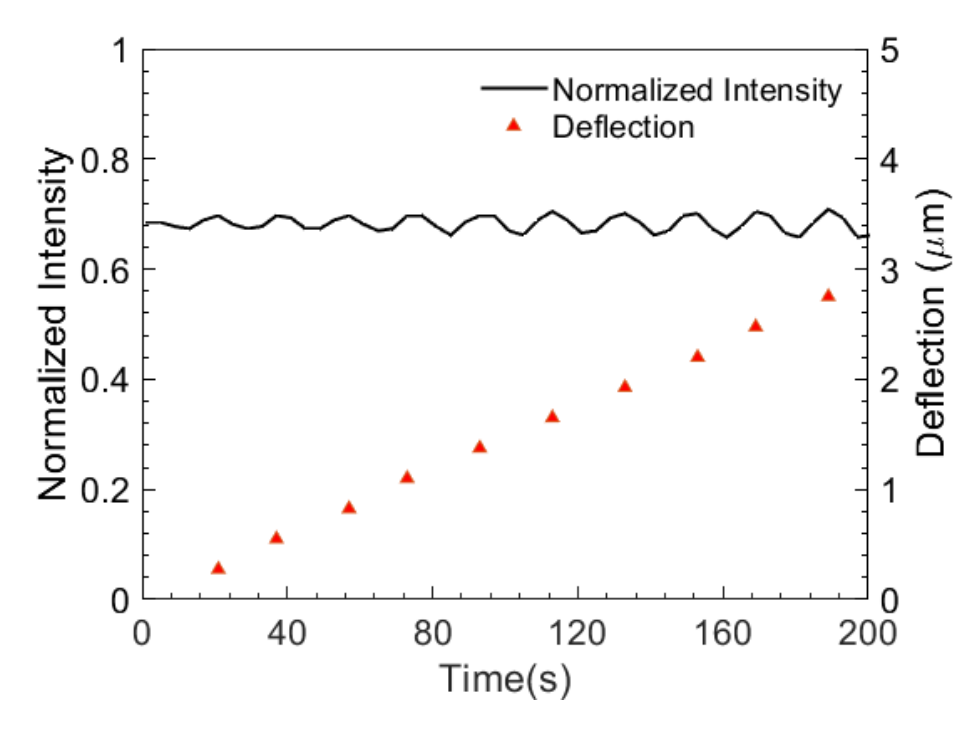


Figure 2.6 Intensity of the pixel (or point) indicated as 'x' in Fig.2.5a is plotted as a function of time during the experiment. The triangle symbol (corresponding to intensity peaks) represent the out-of-plane deflection of the point 'x' as a function of time. In this example, the total out-of-plane displacement is 2.75 µm (as 10 peaks passed the point in 200 s).

film on SiO_2 . The substrate was fixed by constraining nodes at the bottom surface. A symmetric displacement boundary condition was prescribed for the nodes on the left edge of the film at x=0. The thickness of the substrate does not affect the stresses either in the PVdF film or at the PVdF/SiO2 interface, hence, it was adjusted to 500 μ m to optimize computation time. Similarly, the stresses in PVdF film, in SiO_2 , or at the interface far from the crack tip in the radial distance tend to be negligible (see Fig. 2.7); hence, only a portion of the sample dimension was modeled.

The PVdF film was discretized with 8-noded quadrilateral elements CAX8R, and at least ten elements were included across the thickness of the film with the smallest element size being 50 nm. As per the sample, a Cu coating of 130 nm below the free-standing PVdF was included in the model. Similar to PVdF, the SiO2 was discretized with CAX8R elements, with the size of smallest element being 5nm. To capture the stress singularity, the region around the crack tip, i.e., the first ring of elements shown within the circle around crack tip in the inset of Fig.2.8, is modeled

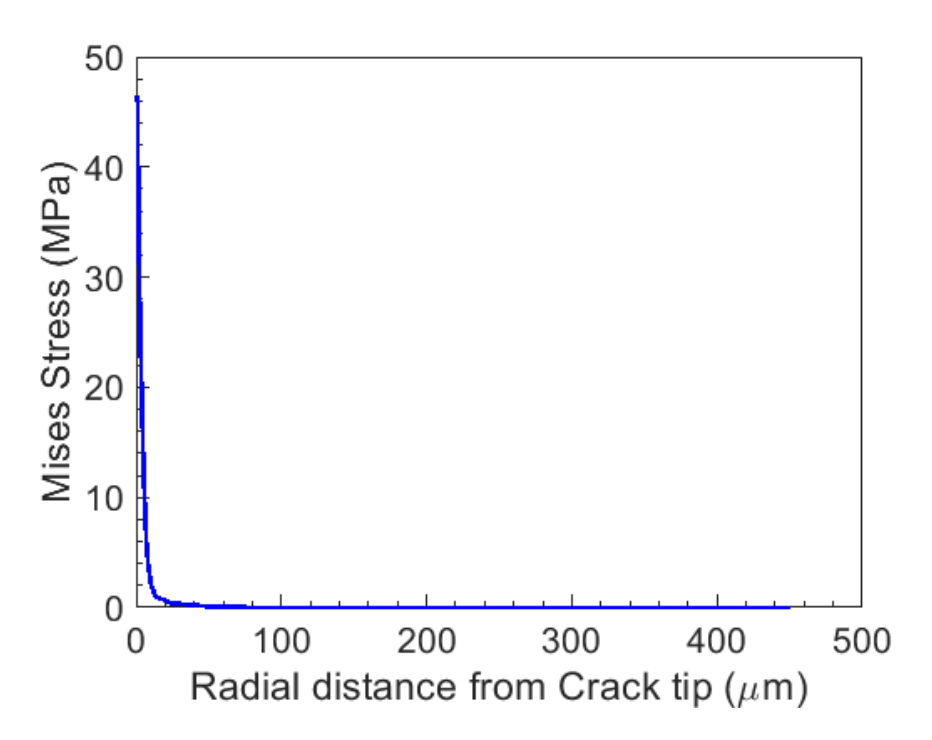


Figure 2.7 The Mises stress magnitude as function of radial distance where the stress goes to zero within $100 \mu m$ of radial distance.

using special 6-noded triangular elements called singularity elements formed by collapsing 2 nodes of 8 node element CAX8R. The mesh grading and the element sizes in Fig.2.8 were optimized through mesh sensitivity study, and further reduction in element size did not produce any significant change in the results. The strain energy release rate was obtained by evaluating contour integral (or J-integral) around the crack tip. The method involves defining the crack tip, crack flanks, and the direction of crack growth as shown in the inset of Fig.2.8. The J-integral [71, 72] was evaluated far away from the crack tip, to ensure the evaluated J-integral values are path independent. Since the crack is at the interface, besides the energy release rate, one has to evaluate the phase angle which provides a measure of shear to opening stresses near the crack tip. The phase angle is given by $\psi = \tan^{-1} \sqrt{\frac{G_{II}}{G_I}}$ where G_I and G_{II} are the energy release rates corresponding to opening and shear mode of fracture, respectively. I. S. Raju [73] proposed a virtual crack closure technique (VCCT) using for 6-noded singularity elements to calculate energy release rate and corresponding phase angle for linear elastic materials. Here, this method was used to determine the phase angle and to

verify if the energy release rate obtained from VCCT matches with that obtained from J-integral.

The PVdF polymer was modeled as a rate dependent isotropic hardening model with the flow rule given as,

$$\dot{\epsilon}^{pl} = D \left(\frac{q}{\sigma^0} - 1 \right)^n \tag{2.1}$$

where $\dot{\epsilon}^{pl}$ is the equivalent plastic strain rate, D and n the temperature dependent material parameters, $\sigma^0(e^{pl})$ the static yield stress, and $q=\sqrt{\frac{3}{2}}\mathbf{S}:\mathbf{S}$ the equivalent stress, where \mathbf{S} is the deviatoric stress. As the experiments were conducted under isothermal conditions, no temperature dependence is considered in the model. The experimental true-stress and true-strain data of PVdF from Santimetaneedol et al. [27] was provided directly as input to the model (as an alternative to prescribing D, q, and n values). The SiO₂, Si, and Cu coating are modeled as linear elastic materials. The properties of these materials are outlined in Table 2.1.

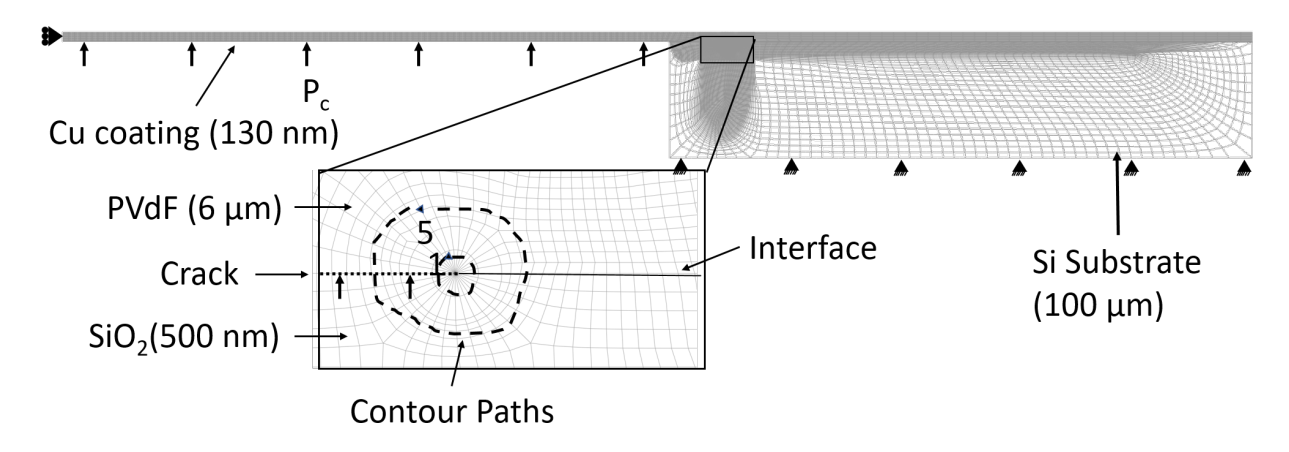


Figure 2.8 Finite element mesh and boundary conditions of the blister test sample. The inset shows the mesh details near the crack tip and a typical contourd used to evaluate J-integral.

2.4.2 Analytical Methods

The deformation response and fracture parameters of the pressurized films were also evaluated using closed form analytical expressions proposed in the literature. Although PVdF exhibits time-dependent material behavior [27], it was assumed as linear elastic material to ascertain if this simple

Table 2.1 Mechanical properties of materials used in finite element simulation.

Materials	Parameters	Values	Remarks
SiO ₂	Youngs Modulus	71 GPa	[72]
	Poisson Ratio	0.16	
Cu	Youngs Modulus	130 GPa	[72]
	Poisson Ratio	0.34	
Si	Youngs Modulus	160 GPa	[74]
	Poisson Ratio	0.28	

model can capture the mechanical behavior of the film prior to the onset of delamination. When the deflections of the film increase to values on the order of film thickness, as in PVdF films here, the films behave more like a membrane [72]. Using the membrane theory assumption, Small et al.[75], derived the pressure - central deflection relation for pressurized circular membranes as,

$$P = C_1 \frac{\sigma_0 t_c}{a^2} w_0 + C_2 \frac{E_c t_c}{(1 - \nu)a^4} w_0^3$$
 (2.2)

where, P is the pressure applied and $w_0 = w_i + w_m$ the central deflection as per Fig. 2.2. Here the central deflection is sum of the initial height (w_i) for non-flat films and measured deflection (w_m) from Fig. 2.6. The geometric parameters of the sample are: the radius of the free-standing film a, the film thickness t_c , and the geometry dependent constants C_1 and C_2 which are 4 and 2.475, respectively, for a circular membrane. Since these equations are for linear elastic membrane, the necessary material properties are E_c which is the Young's modulus of the film and is the Poisson ratio. The σ_0 is the residual stress. The central deflection w_0 for a given pressure P was obtained by solving the Eq. 2.4.2 using the Newton-Rhapson method.

Since a layer of Cu is deposited below PVdF, the elastic modulus of the PVdF/Cu composite film is obtained by following the method proposed by Small et al.[76]. The biaxial modulus of the composite film is obtained as

$$M_c = \frac{t_f}{t_c} M_f + \frac{t_{Cu}}{t_c} M_{Cu} \tag{2.3}$$

where, M is biaxial modulus and the subscripts f, Cu, and c refer to PVdF film, Cu and composite, respectively. The t_f , t_{Cu} , and $t_c = (t_f + t_{Cu})$ are the thickness of PVdF, Cu, and composite, respectively. Since Poisson's ratio of PVdF and Cu are similar referring to Table 2.1 we can get Young's modulus of composite film using Eq. 2.4.2 as 3.6 GPa. The corresponding energy release rate for pressurized circular membrane[67] is given as,

$$G = \frac{5}{8} C_2 \frac{E_c t_c w_0^4}{a^4} \tag{2.4}$$

2.5 Experimental Setup and test procedure for interface failure under electrochemical condition

2.5.1 Electrochemical cycling

Figure 2.9a. show the electrochemical cell assembly to lithiate the Si through PVdF. Here the PVdF/Si sample is mounted on a 2 mm thick stainless steel plate and correspondingly the plate is adhered to the electrochemical cell using a chemical resistant epoxy (Loctite Stycast 2651 Henkel Adhesive). A celgard polymer separator soaked with electrolyte (1:1:1 wt% EC:DC:DMC with LiPF₆ salt) is placed on top of the sample to allow physical separation between sample and Li foil and allow a controlled and uniform absorption/soaking of electrolyte by the PVdF film. In this experiment the PVdF/Si sample acts as a working electrode and Li foil acts as the counter and reference electrode. Here the edges of the sample and the Cu wire connection were covered with Loctite adhesive to prevent lithium flux form any other direction except through PVdF. A galvanostatic current of 7.5 μ A was applied which correspond to 2 μ A cm⁻² current density since the lithium flux area varied from sample to sample. The cycling was carried out in enclosed cell to avoid any reaction with external atmosphere and in addition, the cell was cycled inside a glovebox (MBraun Inc, filled with Argon, <0.1 ppm O2 and <0.1 ppm H2O) for further protection against environment.

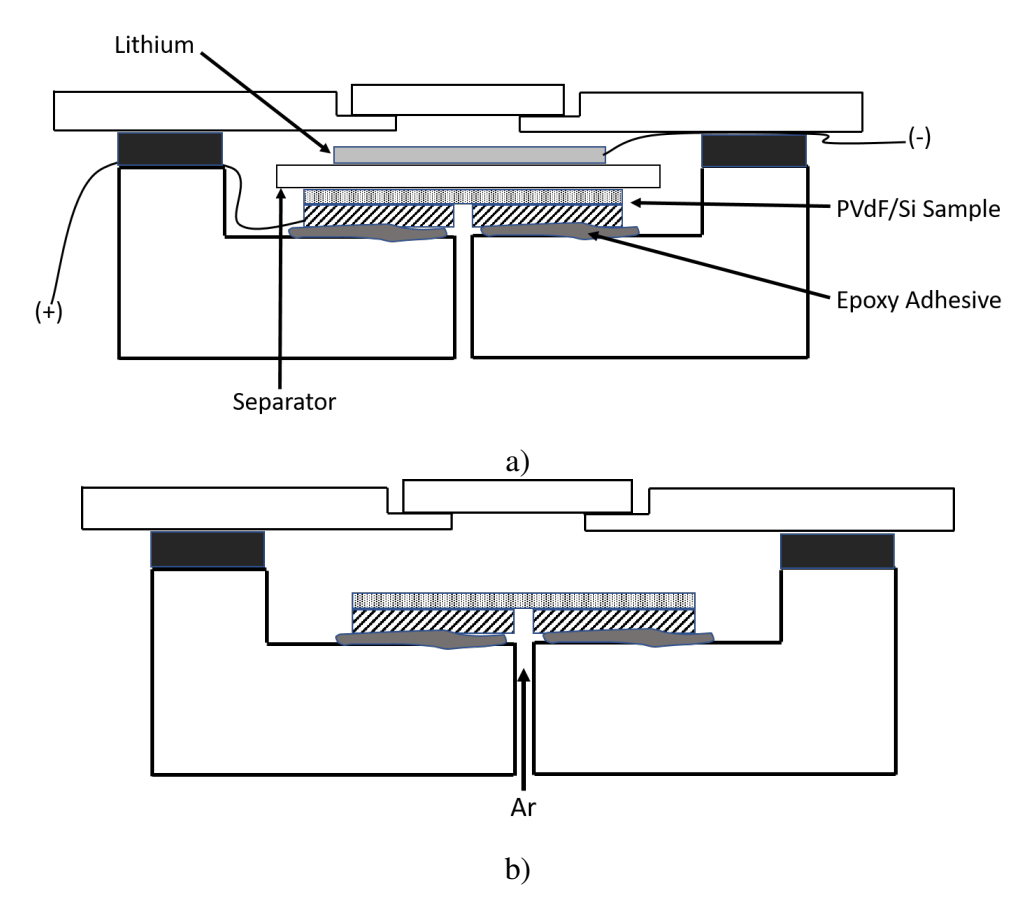


Figure 2.9 a) Shows the setup of electrochemical cell to lithiate the Si and form LixSi at the interface. The sample prepared according to section 2.1 is adhered using epoxy a 2 mm thick stainless steel plate (not shown here) and the plate is adhered to the electrochemical cell. A celgard separators is placed above the sample and lithium counter/reference electrode is placed above to provide the Li+ ion flux. b) The same electrochemical cell is used for interface fracture test where the celgard separator and lithium foil is removed. During interface fracture test Ar is introduced to induce interface fracture.

2.5.2 Interface fracture test under electrochemical conditions

The interface failure tests were performed in the same cell in which electrochemical lithiation was performed as shown in Fig. 2.9b. The testing was done in the same cell in order to avoid any external loading on the sample and at the interface. To perform this test, separator and lithium was removed first, to allow visual observation of the interface and second, to avoid Li flux while PVdF and Si are loaded until failure. The stress concentration generated during interface failure test can act as a driving force for lithium flux when complete electrochemical cell assembly is present [42]. The removal of Li and separator also allows any open circuit potential (OCP) change

and side reactions during the experiment which can affect the concentration in Si and properties at the interface [66, 77].

The PVdF/Lithiated Si sample were loaded until failure by subjecting the sample to ultra-high purity Ar through an orifice below the sample. A constant mass flow rate of 0.2 sccm was applied until 0.5 KPa as a preload and 0.8 sccm mass flow rate was maintained until failure. The two step process allows to capture large displacement changes usually observed for membrane during initial loading [72, 78]. The mass flow rate of 0.8 sccm was used in order to subject the PVdF film and interface to same strain rates. This mass flowrate of 0.8 sccm resulted in a constant 0.5 kPa/min of pressure loading on the PVdF film during the test. The pressure in the cell was measured using a pressure sensor (Omega PX309-050a5v) with a resolution of 0.1 kPa. The deflection of PVdF under the applied pressure was measured using an in house constructed Michelson interferometer setup shown in Fig. 2.4b. For futher information about the experimental setup construction we refer to 2. Images of the interference pattern projected on the sample were captured every 200 ms. The interference pattern moves when PVdF starts to bulge under the applied Ar mass flow. In this experiment light of wavelength of 514 \pm 1 nm was used compared to 550 \pm 10 nm previous experiment on PVdF/SiO2. The wavelength bandwidth of ±1 nm allows to measure higher deflection (100 μm) as compared to ± 10 nm (where deflection measured were 30μm) which improves coherence length of light [79]. This optical system allows for a spatial resolution of 5 μm and out of plane displacement resolution of 128.5 nm. To convert the images to displacement we followed the same procedure as in section 2.3.

2.5.3 Crack initiation pressure identification

Figure 2.10 shows the typical pressure-central deflection of PVdF/lithiated Si sample in blue and the sample compliance i.e. $\frac{dw_0}{dP}$ as black curve. It was observed from a typical pressure-central deflection, the compliance $\frac{dw_0}{dP}$ asymptotes towards a minimum when there is no interface failure (between PVdF/Lithiated Si) or no inelastic effect (plastic deformation of PVdF). However, in the observed samples we see the asymptote however after certain pressure as in Fig. 2.10 after 6 kPa the compliance increases. The observed compliance change also correlated to the typical

membrane behavior. It is known that pressure-central deflection is cubic i.e. $P \propto w_0^3$, which means $\frac{dw_0}{dP} \propto \frac{1}{P^{2/3}}$, any deviation from this behavior show interface failure and can be used to identified crack initiation point (or pressure) as shown by red x mark in Fig. 2.10. Here we choose a 15% increase in sample compliance as a criteria for crack initiation. This method is also verified by the dry PVdF/Si sample where clear crack initiation was observed.

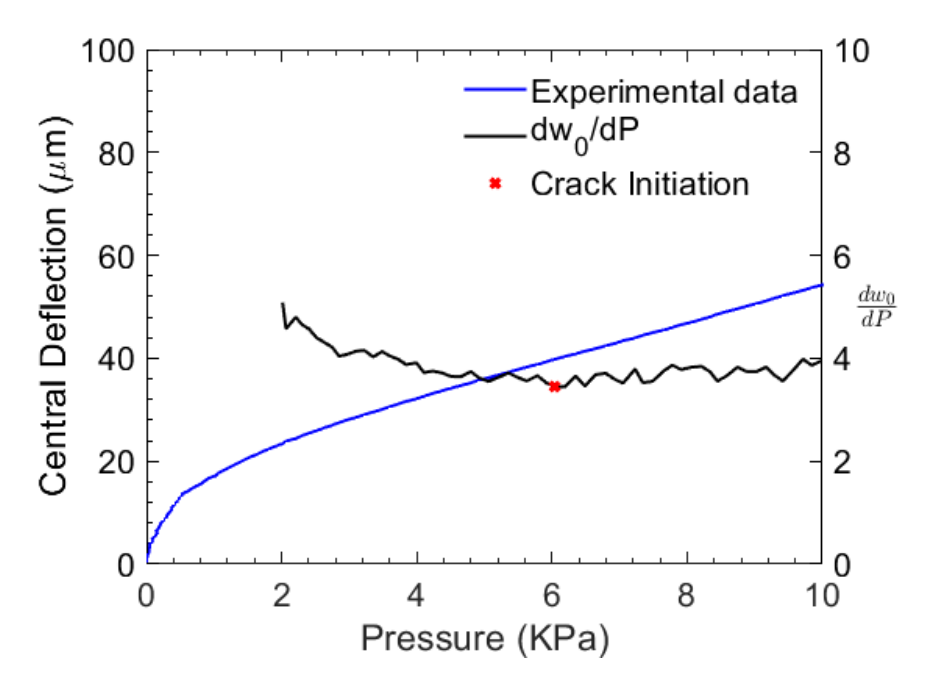


Figure 2.10 Typical pressure-central deflection (in blue) of a sample along with sample stiffness $\frac{dw_0}{dP}$ (in black). The red x marks the crack initiation point which is obtained from the minimum of $\frac{dw_0}{dP}$.

CHAPTER 3

INTERFACE FAILURE RESULTS UNDER DRY CONDITIONS

Iin this chapter we will describe the results obtain from testing the PVdF/Si interface. First we describe the pressure-central deflection response of the film, second, we provide the interface fracture behavior of the PVdF/SiO₂, and lastly we predict the obtain characterized value through experimentation.

3.1 Mechanical response and crack tip condition of PVdF/Si samples

Figure 3.1a shows the applied pressure and the pressure at which the PVdF film delaminates form a Si surface. The x mark indicates the crack initiation point. The complete delamination is shown by the sharp drop in pressure. With the criteria of 50 µm delamination observed (Ref. Fig. 3.1b), the crack initiation point is indicated by a red X in Fig. 3.1a.

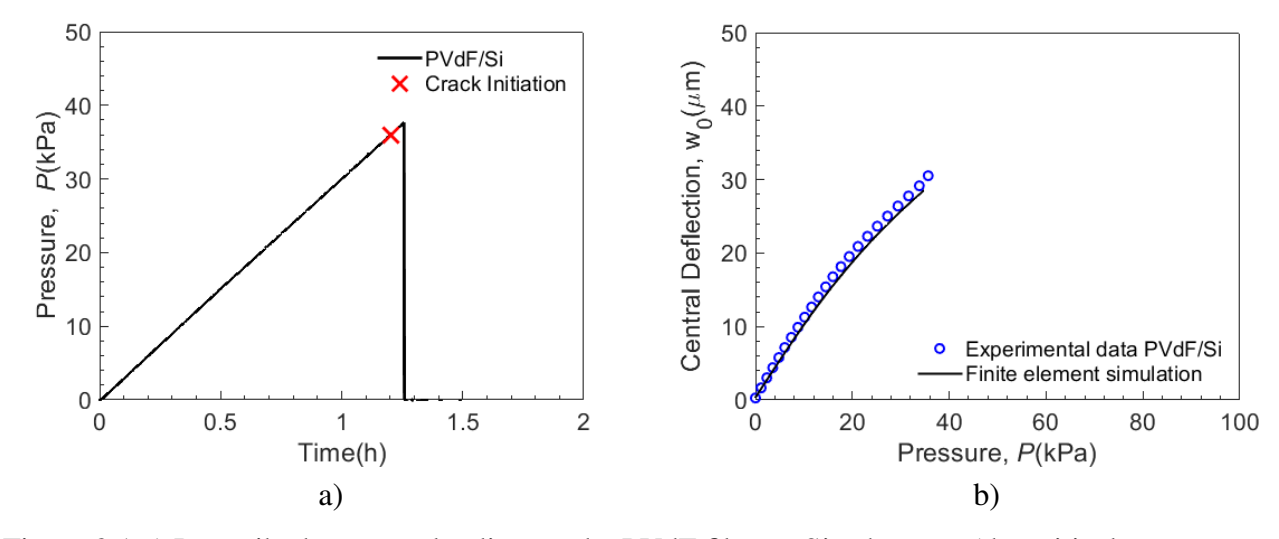


Figure 3.1 a) Prescribed pressure loading on the PVdF film on Si substrate. (the critical pressure associated with onset of delamination is indicated with "x"). b) The Pressure-Central Deflection of the PVdF film from a typical sample of PVdF/Si (blue open circles) along with FE simulation.

Figure 3.1b shows the experimental central deflection of the PVdF under the applied pressure, which was measured using the interference pattern projected on the sample and at the center of the circle. The experimental data for PVdF on Si is shown by the open circles and compared to the solid black line for the FE simulation. The experimental data when compared to the FE simulation

which is performed until peak shows a deviation i.e. from 35 KPa and beyond. This deviation is due to the crack initiation and propagation where the radius of circular sample increases and the corresponding deviation increases whereas in the FE simulation the radius is fixed therefore, this is also an indication that crack has initiation and it corroborates with the visual observation of crack initiation.

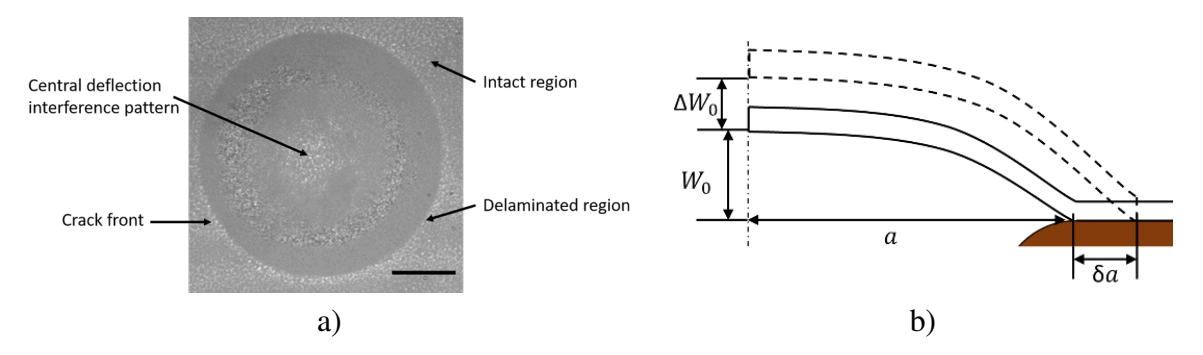


Figure 3.2 a) The crack front propagation identified by contrast difference between PVdF and Si (Note: the scale bar on bottom right is 200 μ m). b) Shows the schematic showing crack extension (δa) and corresponding change in central deflection (ΔW_0) due to crack extension.

The observed central deflection of PVdF is significantly greater than the thickness of film (\approx 6 μ m) which implies the PVdF behaves as a membrane [72]. The observed central deflection also depends on the initial condition of the PVdF film i.e. the initial height and residual stress of film [80, 81, 75]. The initial height i.e. the film is not flat at the beginning of the experiments. It is observed that the PVdF remains flat at the beginning of experiments, this was confirmed using optical profilometry and FIB cut across the sample therefore any effects due to it has been neglected.

The residual stress is another initial condition which affects the deformation of PVdF under the applied pressure. The origin of residual stress lies in the mismatched strain when PVdF is deposited on a substrate [72]. The difference in coefficient of thermal expansion causes this mismatch. Is should also be noted that the PVdF film has undergone various process during sample preparation (Section 2.1) therefore, this process can affect the residual stress. The residual stress is measured using substrate curvature method for PVdF/Si is 10.6 ± 0.8 MPa. To verify the residual stress obtained for PVdF/Si, we plot the experimentally obtain pressure (P) and central deflection (W_0)

as $\frac{P}{W_0}vsW_0^2$ as shown in Fig. 3.3. It should the noted that the residual stress obtained from this fit is only valid if PVdF behaved linear elastically [81]. To ascertain if the behavior is linear elastic, Mieses stress magnitude at central deflection point was obtained, the observed stress is below the yield point of PVdF also, the plastic strain is localized at the crack tip. This indicated that PVdF behaves linear elastically until failure which mean PVdF behaves nominally elastic until failure. Therefore, the σ_R can be obtained from experimental pressure-central deflection data. The obtained residual stress is 10.733 ± 2.141 MPa which is similar to the magnitude obtained for substrate curvature method which verifies the residual stress measurement.

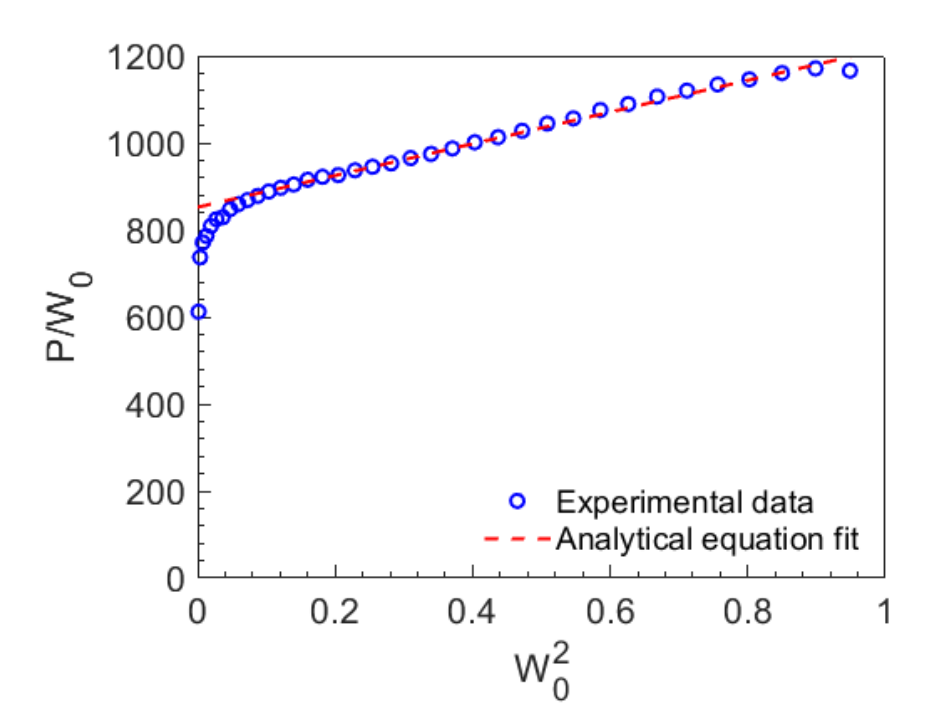


Figure 3.3 The plot of ratio of Pressure-deflection plotted against deflection square show that the y-intercept can be used to obtain the residual stress in the film provided that the film is flat and behaves elastically during the experiment.

The initial conditions i.e. the initial height and residual stress is included in the FE simulations therefore, an excellent match to the pressure-central deflection is obtained and shown in Fig. 3.1b. The FE simulation verify the nominally elastic behavior of PVdF film at the onset of delamination. Also, small scale yield is observed where the plastic strain is localized at the crack tip. Therefore,

the J-integral or the critical strain energy release rata Gc provides the adhesion between PVdF/Si.

3.2 Interface failure behavior of PVdF/Si under dry conditions

The interface failure behavior PVdF/Si is characterized at the crack initiation point. The critical energy release rate (Gc) obtained using FE simulation (J-integral) for axisymmetric PVdF/Si interface is 0.59 ± 0.18 Jm-2 for axisymmetric sample whereas 0.74 ± 0.14 Jm-2 plane strain rectangular samples as shown in Fig.3.3. The variation in G_c for axisymmetric and plane strain geometry is due to phase angle at failure pressure which for axisymmetric sample is 68° compared to 72° for plane strain. The G_c is known to increases with phase angle and has been shown for various other interfaces (e.g. glass/epoxy, silicon/epoxy) [82, 83]. These measurements were obtained from 7 sample for each interface and geometry. As the pressure-central deflection data is influenced mainly by two initial condition i.e. initial height and residual stress it is important to see the sensitivity of G_c to these parameters. FE simulation was performed with and without initial height keeping other initial and boundary conditions constant. It was observed that the difference in J-integral (with and without initial height) is <1%. Therefore, the effect of initial height is negligible on G_c . Similarly, to understand the effect of residual stress FE simulation was performed with and without residual stress keeping other initial and boundary condition constant. It was observed that neglecting residual stress G_c is overestimated by 47%. The significant overestimation for PVdF/Si is because the residual stress in PVdF/Si samples is 10 MPa which is nearly half of the yield stress. This shows that residual stress is an important parameter when obtaining G_c (Allen and Senturia, 1988). Including these initial conditions in FE analysis allows to accurately obtain the G_c for the interface samples. It can be implied from the G_c measurements that it provides the intrinsic adhesion energy between of PVdF/Si as the measure G_c does not contain the plastic dissipation associated with viscoplastic PVdF [84].

To determinate the nature of failure i.e. whether the crack propagates in Si, in PVdF or at the interface, X-ray photoelectron spectroscopy (XPS) analysis was performed on the PVdF, and on the fracture surface. Table 3 shows the chemical composition in at% on the surface of PVdF, bare Si and PVdF/Si fracture surface. Comparing the F concentration, it can be observed that the interface

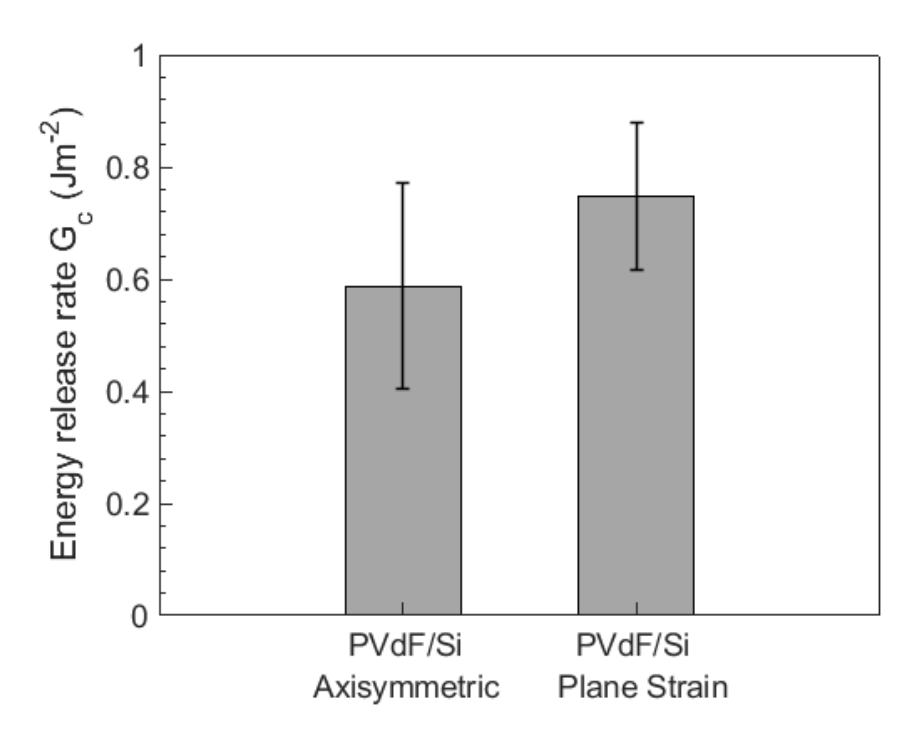


Figure 3.4 The energy release rate (G_c) for axisymmetric and plane strain sample obtain using J-integral in FE simulation at the crack initiation point. The slight difference is due to phase angle which for plane strain is higher compare to axisymmetric.

failure is predominantly adhesive i.e. the crack propagates at the interface neither in PVdF not in the Si substrate. Therefore, the obtained Gc is the interface energy release rate or the adhesion of PVdF to substrate. The Oxygen (O) content is observed on the fractured surface of PVdF/Si in spite cleaning with HF, this is because as soon as the pristine Si surface is exposed to air, native oxide layer starts to form and cannot be avoided. To further limit the growth of this oxide is PVdF is spincoated immediately on Si. It can be implied that native oxide layer thickness on Si surface is 0.2 nm as the PVdF is spincoated with 60 min [85]. Also, when native oxide forms, -OH radical attach to the Si surface which can contribute to the O content [86].

Table 3.1 The chemical composition in at% on the PVdF film, bare Si surface and on the fracture surface of PVdF/Si.

Sample/Composition	С	О	F	Si	N
(at%)					
Bare Si	23.97	17.05	0.58	57.09	0.84
PVdF	59.28	4.56	35.32	0	0.84
Fractured Surface	19.80	35.00	1.05	42.82	1.34

3.3 Characterization of PVdF/SiO₂ Interface Failure

3.3.1 Mechanical response and crack tip conditions

Figure 3.5a shows the typical profile of free-standing circular film measured (using Zygo NewView5000 optical profilometer) before pressurizing the film. Note that the PVdF film is not flat at the start of the experiment, i.e., under zero applied pressure, and this is true in all the samples. This is expected because (during the sample preparation process, Fig.2.2b) the thermally grown SiO₂ film releases its compressive residual stress by buckling out-of-plane when the substrate is etched away [87]; this out-of-plane buckling is inherent to SiO₂ films [88]. The spincoated PVdF film assumes the shape of the relaxed out-of-plane buckled configuration of SiO₂, resulting in the profile shown in Fig. 3.5a.

Note from Eq.2.4.2 that in addition to measuring the initial profile (shown in Fig. 3.5a) and film thickness (Fig.3.5b), it is important to measure the residual stress in the film to characterize/understand the mechanical behavior of the PVdF film [89]. The residual stress in PVdF thin film was measured using Multibeam optical sensor (MOS) setup (see Fig.3.6). In this setup, curvature of SiO_2 substrate is measured before and after PVdF deposition and converted to stress using Stoney equation [72, 90]. The measured value of the residual stress in PVdF film is ≈ 3 MPa, which is not significant enough to influence the pressure-central deflection behavior of the film.

Figures 3.5c and 3.5d show the prescribed pressure loading applied on the circular film and the evolution of the film profile at various levels of pressure, respectively. The critical pressure at the onset of film delamination is indicated with a symbol 'x'. The open circle symbols in Fig. 3.5d represent the experimental data and the solid lines represent FE results. The deflection-pressure data corresponding to x=0 from Fig.3.5d, i.e., at the center of free-standing film, is plotted in Fig.3.5e, which is commonly referred to as pressure-central deflection response of the PVdF film. Although pressure is monitored and recorded continuously throughout the experiment, the displacement data is available only until about 30 μ m, due to the characteristic bandwidth of green light source used here. Note from Figs. 3.5d and 3.5e that there is an excellent agreement between experimentally measured deflections and film profile at various levels of pressure and the corresponding FE data.

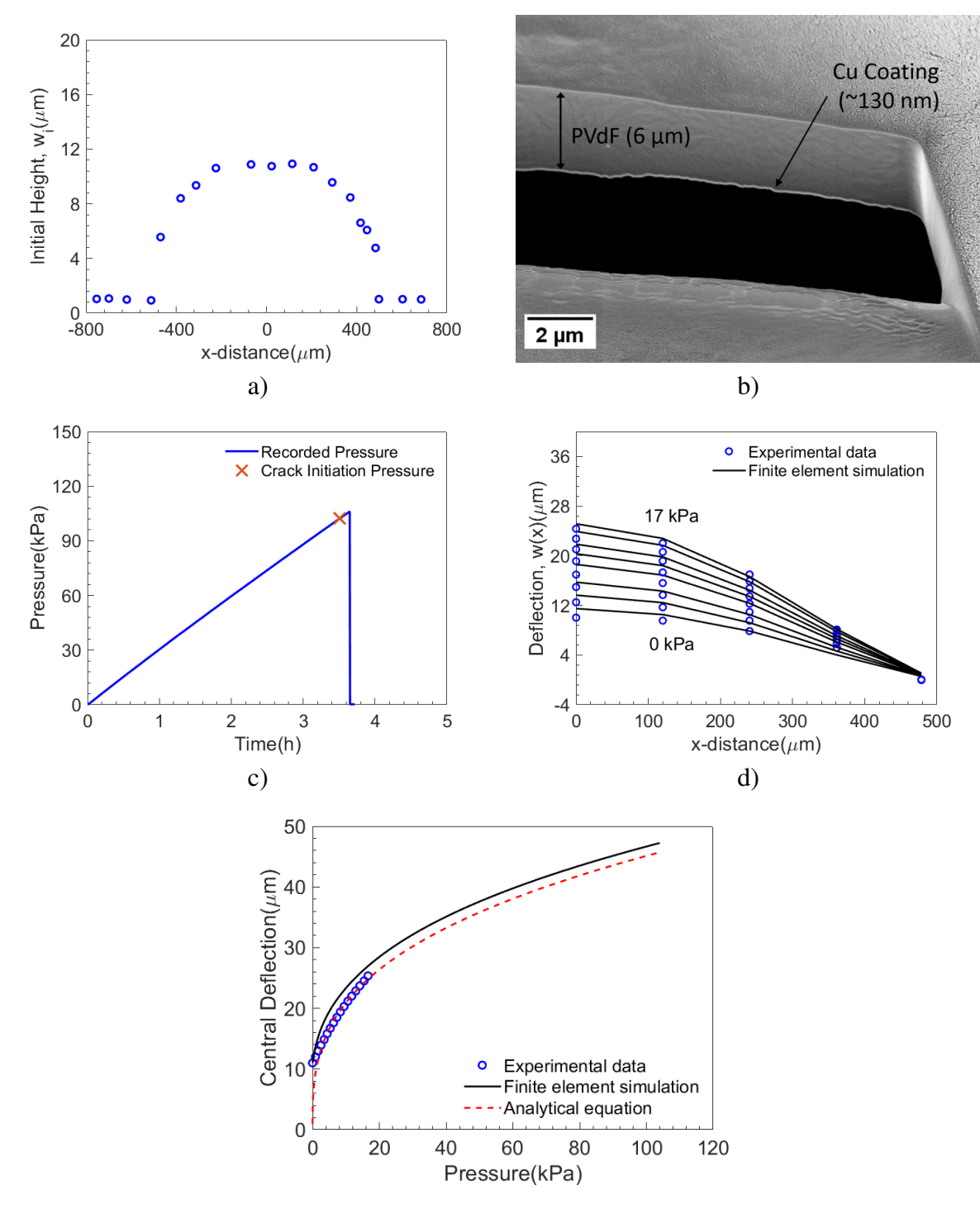


Figure 3.5 (a) The profile of circular PVdF film measured under zero applied pressure, (b) the cross section of free-standing PVdF film obtained by FIB milling, (c) prescribed pressure loading on the film (the critical pressure associated with onset of delamination is indicated with "x"), (d) comparison of experimentally measured film profiles at various levels of pressure with those obtained from finite element analysis, and (e) comparison of pressure-central deflection response (p-wo) of the film measured from experiments and those obtained from analytical and finite element models.

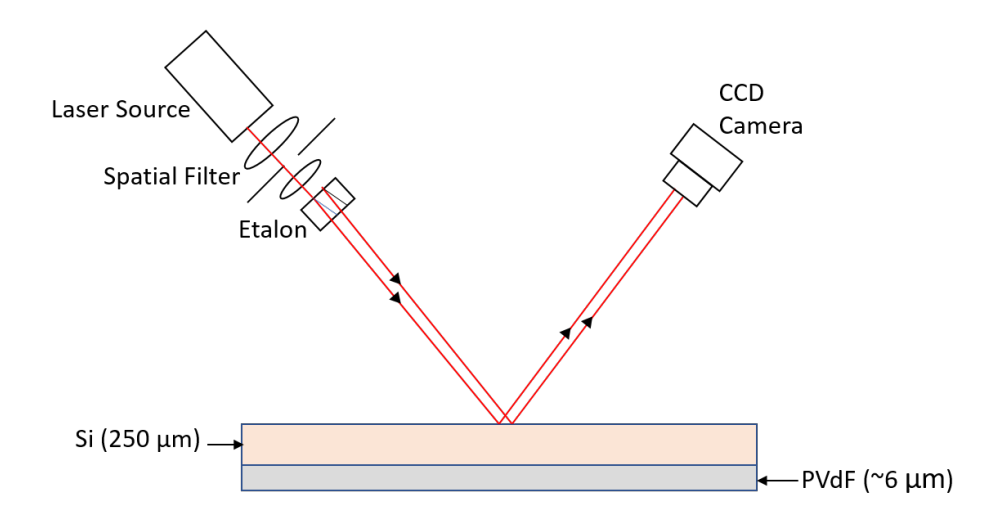


Figure 3.6 Schematic of multibeam optical sensor setup (MOSS) showing the method the to measure residual stress. The residual stress is measured by recording the curvature of the 2-in Si wafer before and after PVdF deposition.

This could be attributed to the fact that in addition to an accurate constitutive model of PVdF, all the critical system parameters discussed above, i.e., thickness, initial profile, and residual stress of the PVdF film have been accounted for in the FE models. For example, the initial (non-flat) profile of the film, i.e., Fig 3.5a, under zero pressure was included in FE analysis by first deforming the mesh until the profile matched experimental values in Fig.3.5a and then importing the deformed mesh as the starting geometry for the subsequent simulation, where pressure-time loading shown in Fig.3.5c was prescribed along with the boundary conditions shown in Fig. 2.8. It should be noted that when matching profile and central deflection, the interface crack between PVdF and SiO₂ was closed and only for calculation after crack initiation, the interface crack was pressurized. The residual stress in the film was also included in the simulation as an initial condition. As a result, the overall mechanical behavior of the PVdF film on SiO₂ was captured well by the finite element model.

It is interesting to note from Fig. 3.5e is that the pressure-central deflection $(p-w_0)$ response predicted by the analytical solution i.e., Eqs. 2.4.2 and 2.4.2, (dashed line) also matches very well with the experimental data. This is interesting because the analytical equation is based on finite deformation linear elastic membrane theory, yet it predicts the mechanical response of the

rate-dependent (or elastic-viscoplastic) PVdF film successfully. This can be explained further by looking at the stress and strain fields in the PVdF film. Fig. 3.7 shows the von Mises equivalent stress and equivalent plastic strain contours of PVdF film at the critical pressure (i.e., at the onset of crack growth). Note that the equivalent stress near the center of the circular membrane (i.e., in the central deflection region, inset on the left side in Fig. 3.7) is between 12 to 24 MPa which is below the yield strength of PVdF reported by Santimetaneedol et al.[27]. The equivalent plastic strain contour (inset on the right side in Fig.3.7) shows that the plastic deformation of PVdF film occurs in a very small region near crack tip. Hence, the deformation of PVdF film is nominally elastic prior to the onset of crack growth. This is analogues to small scale yielding condition in linear elastic fracture mechanics theory which justifies application of linear elastic theory to ductile materials such as steel for example [71, 91]. This explains why the analytical solution (Eqs. 2.4.2 and 2.4.2) based on simple linear elastic membrane theory predicts the behavior of the PVdF film reasonably well. The small discrepancy between the experimental and analytical results can be attributed to the fact that the analytical solution was derived based on the assumption that the film is flat at zero pressure which is clearly not the case in the current film as shown in Fig. 3.5a. Another important observation is that the current experimental setup enables the interface fracture characterization with simple linear elastic properties of PVdF film and corresponding analytical solutions.

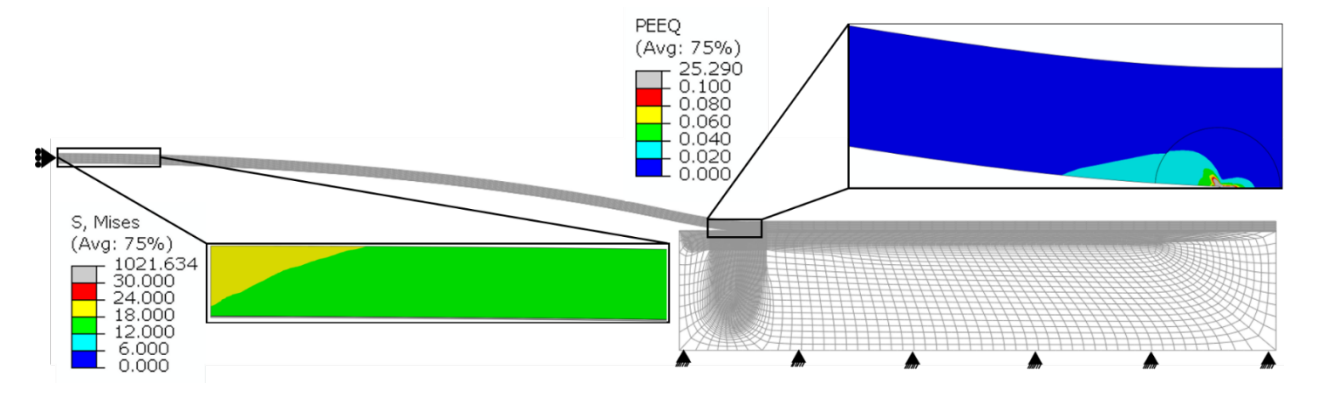


Figure 3.7 Deformed mesh of the circular membrane at the critical pressure is shown along with the equivalent (von Mises) stress contour near the center of the film (inset on the left side) and the equivalent plastic strain near the crack tip (inset on the right side). This confirms that the PVdF film remains nominally elastic prior to onset of delamination, i.e., existence of small scale yielding conditions.

3.4 Interface fracture behavior of PVdF/SiO₂

The critical pressure at the onset of crack propagation measured from circular blister tests is used in FE models to determine the critical energy release rate Gc of PVdF/SiO2 interface and is shown in Table 3.2. It should be noted that, to measure the linear elastic fracture property, i.e., the interface fracture energy Gc, it is extremely important to ensure that the dissipative mechanisms such as plastic deformation are limited to a very small region near the crack-tip in a fracture sample as shown in Fig. 3.6. The maximum, minimum, and the average critical energy release rate Gc values of PVdF/SiO₂ interface are 3.04 J/m², 2.02 J/m², and 2.46 J/m², respectively. As expected, due to the small-scale yielding conditions in the samples, the Gc evaluated from analytical equations matched very well with the FE calculations. Although the analytical equation assumes a flat PVdF film under zero applied pressure, the Gc matched with the comprehensive FE model; hence, the errors associated with an initial non-flat film profile may be negligible for PVdF films.

In order to understand the potential errors in measured Gc due to the uncertainty associated with the PVdF/SiO₂ sample parameters, several finite element simulations were conducted. It was observed that if the initial profile of the film was neglected (i.e., if the free-standing film was assumed to be flat), keeping everything else constant, the error in Gc will be 0.03%, i.e., negligible. This is why the analytical data (with flat film assumption) matched with FE data very well. The reason for this can be evident from Fig. 3.5(e), where the central deflection of the film rises steeply to 12 μ m with negligible pressure; hence, as long as the initial height of the film is less than 12 μ m, error associate with neglecting initial height of the film is minor. However, neglecting the residual stress σ_R , on the other hand, will lead to an overestimation of the Gc by 7%. If both the initial profile and residual stress in the film are neglected, then Gc will be overestimated by 8%. Since the initial height and residual stress, film thickness, radius of the film, and critical pressure were measured experimentally, the variation in the Gc values presented are primarily due to the sample to sample variation.

Figure 3.8 shows the fracture surface of the sample after the PVdF film was completely delaminated from the SiO2 surface. To understand the crack path and fracture mechanism, an X-ray

Table 3.2 The pressure at the onset of delamination and the corresponding critical energy release rate (G_c) values of PVdF/SiO₂ interface measured from seven circular blister tests. As this is a mixed-mode fracture property, the phase angle ψ_G corresponding to these measurements is 43°.

Sample	Crack Initiation	Energy release	Energy release
	Pressure (kPa)	rate G_c (J m ⁻²)	rate G_c (J m ⁻²)
		Finite element	Analytical
		model	
Sample 1	106	3.04	3.18
Sample 2	104	2.92	3.06
Sample 3	81	2.04	2.09
Sample 4	91	2.45	2.55
Sample 5	90	2.47	2.52
Sample 6	80	2.02	2.04
Sample 7	87	2.28	2.36
Mean + stan-	91 ± 10	2.46 ± 0.40	2.54 ± 0.44
dard deviation (7			
samples)			

Table 3.3 Energy release rate (G_c) for all circular samples measured along with crack initation pressure.

Description	Error (%)
Finite Element with accurate	0.00
initiation condition	
No initial profile i.e. flat film	-0.03
assumption	
No Residual stress initial con-	7.30
dition	
Neglecting both initial profile	7.96
and residual stress	

photoelectron spectroscopy (XPS) analysis was performed on the fracture surface (shown in Fig. 3.8), and the results are compared in Table 3.4 with that of bare SiO₂ and pure PVdF film. Note that the elemental composition, except for the fluorine, of the fractured surface resembles that of bare SiO₂ surface quite closely, confirming that the crack propagation occurred between PVdF/SiO2 interface and not in the PVdF film or in the SiO₂ substrate. Hence, the mechanism is predominantly adhesive failure (i.e., delamination of PVdF film from SiO₂) rather than cohesive (i.e., failure of PVdF film). Since the film was nominally elastic until the onset of crack growth, the measured Gc values characterize the resistance of PVdF/SiO₂ interface to delamination, i.e., the energy neces-

sary to break bonds between PVdF and SiO₂. If the crack propagation occurs primarily in PVdF (i.e., the mechanism becomes cohesive), the energy required to propagate the crack will be higher. As the Gc values presented in Table 3.2 are fundamental fracture properties, they can be used in predicting the failure of PVdF/ SiO₂ interface systems, irrespective of the electrode geometry (i.e., thin film, particles, nanotubes etc.). Although our samples showed predominantly interface failure, it should be noted that several possible crack propagation paths exist in a composite electrode. For example, depending on the fracture resistance of the material, crack can propagate in the polymer binder, in the active material, or at the interface. Hence, for a comprehensive understanding of electrode degradation, in addition to fracture properties of the interface, it is also important to understand the fracture properties of the materials adjacent to the interface.

When a crack propagates at an interface between two dissimilar materials (i.e., similar to PVdF and SiO₂ in Fig. 3.8), even a pure tensile remote load leads to a mixed-mode fracture [71, 91, 84]. Depending on the nature of interface and the adjoining solids, the fracture energy Gc of an interface could be a strong or weak function of the mode-mixity [82, 84]. The degree of mode-mixity is generally characterized by the phase angle ψ which provides a relative ratio of shear to tensile load on a crack tip. The phase angle ψ of the PVdF/SiO2 interface in the blister test samples was evaluated using the virtual crack growth technique (VCCT) [92, 73], and it was 41°. Since the crack growth occurred at the PVdF/SiO2 interface in all the samples tested here, the fracture energy presented in the Table 2 should be associated with a phase angle of 41° for PVdF/SiO₂ system.

Table 3.4 Composition at Various interfaces.

Sample/Composition (at%)	С	O	F	Si
Bare SiO2	22.37	44.77	0.0	32.86
PVdF	63.23	0	36.77	0
Fractured Surface	20.17	40.54	7.46	31.83

3.5 Effect of thermal oxide on the adhesion of PVdF to Si

Figure 3.9 clearly shows the addition of thermal oxide SiO₂ coating at the interface between PVdF/Si improved the adhesion of PVdF. It is known that PVdF adheres to Si surface via. van der walls forces [93, 94, 21, 22, 95, 31, 96]. The adhesion is likely to occurs at the acidic functional

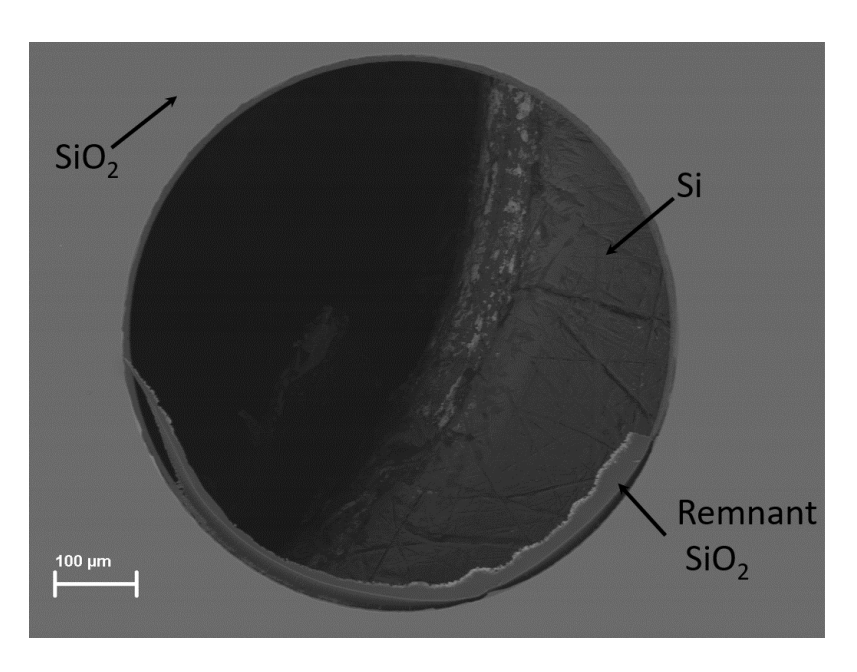


Figure 3.8 Scanning electron microscope backscatter image of the fracture surface (i.e., surface after free standing PVdF delaminated from SiO2). The table shows the atomic weight fractions of elemental C, O, F, and Si obtained from the XPS analysis showing nearly identical stoichiometry of bare SiO2 and delaminated region (with some fluorine on the surface).

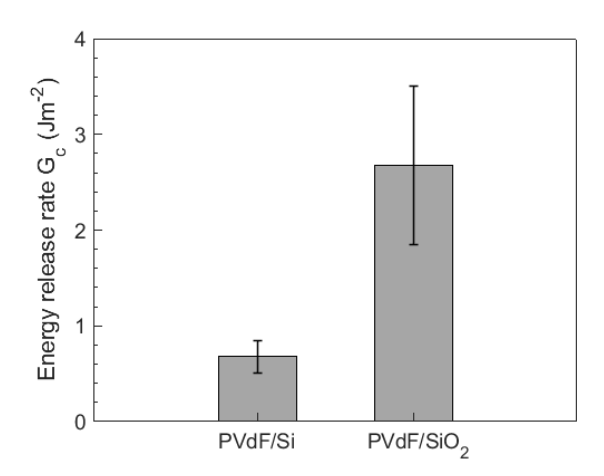


Figure 3.9 Comparison of the energy release rate obtain through finite element by J-integral for PVdF/Si and $PVdF/SiO_2$ interface.

group (-OH) present on the surface of Si [8]. The presence of SiO₂ on Si surface causes the changes in surface concentration of -OH group i.e. more -OH groups per area which mean more site are presented for the PVdF polymer chain to adhere which improves adhesion (Ref. Fig. 3.10d and 3.10e). Studies conducted on increasing silanol (Si-OH) concentration change e.g. (Jiang et al., 2018) increased the concentration by hydrogen peroxide (H2O2) treatment and improved polyacrylic acid (PAA) binder adhesion. Similar observation of SiOx grown on Si nanoparticles were shown by Guo et al. [97]. This can imply that a Si surface when treated with HF the concentration of -OH group reduces as in our case. The thermal oxide surfaces have more -OH group concentration than Si [98, 99] which likely leads to better adhesion. To ascertain this, Raman spectroscopy measurements (Horiba LabRAM ARAMIS) and XPS core scans (Kratos Axis were performed on Si surface treated with HF and SiO2 surface. Fig 3.10a shows the qualitative comparison of Si-OH concentration on Si and SiO2 surface from Raman spectroscopy and Fig. 3.10b and 3.10c shows the deconvoluted spectra at O1s in both Si and SiO2 with emphasis on Si-OH group. This high intensity in Raman can correspond to the higher concentration of Si-OH similarly higher Si-OH concentration on SiO₂ compare to Si can be obtained from XPS since, SiO₂ samples has higher area (nearly twice) under the Si-OH curve. Therefore, it can be clearly implied that the presence of more Si-OH group on surface of SiO₂ as compared to Si is the reason for the higher Gc of PVdF/SiO₂ as compared to PVdF/Si. It can be implied that a composite battery of Si anode with SiO₂ coating will show lower capacity fade as compared to Si.

3.6 G_c as fracture criterion to predict PVdF/SiO₂ Interface failure

To experimentally validate and demonstrate the robust predictive capability of fracture criterion, $G = G_c$, rectangular PVdF films on SiO2 surface (Fig. 3.11) were pressurized until the onset of film delamination, and the critical pressure of failure was predicted. To this end, a finite element mesh of the rectangular (Fig. 3.11) plane strain sample, similar to axisymmetric sample (Fig. 2.8), is constructed in ABAQUS. The continuum plane strain elements (CPE8R) are used to mesh the geometry. The residual stress in the PVdF film and the initial profile of plane strain sample, recorded using Zygo NewView5000 and shown in supplementary data (Fig.3.12), was included

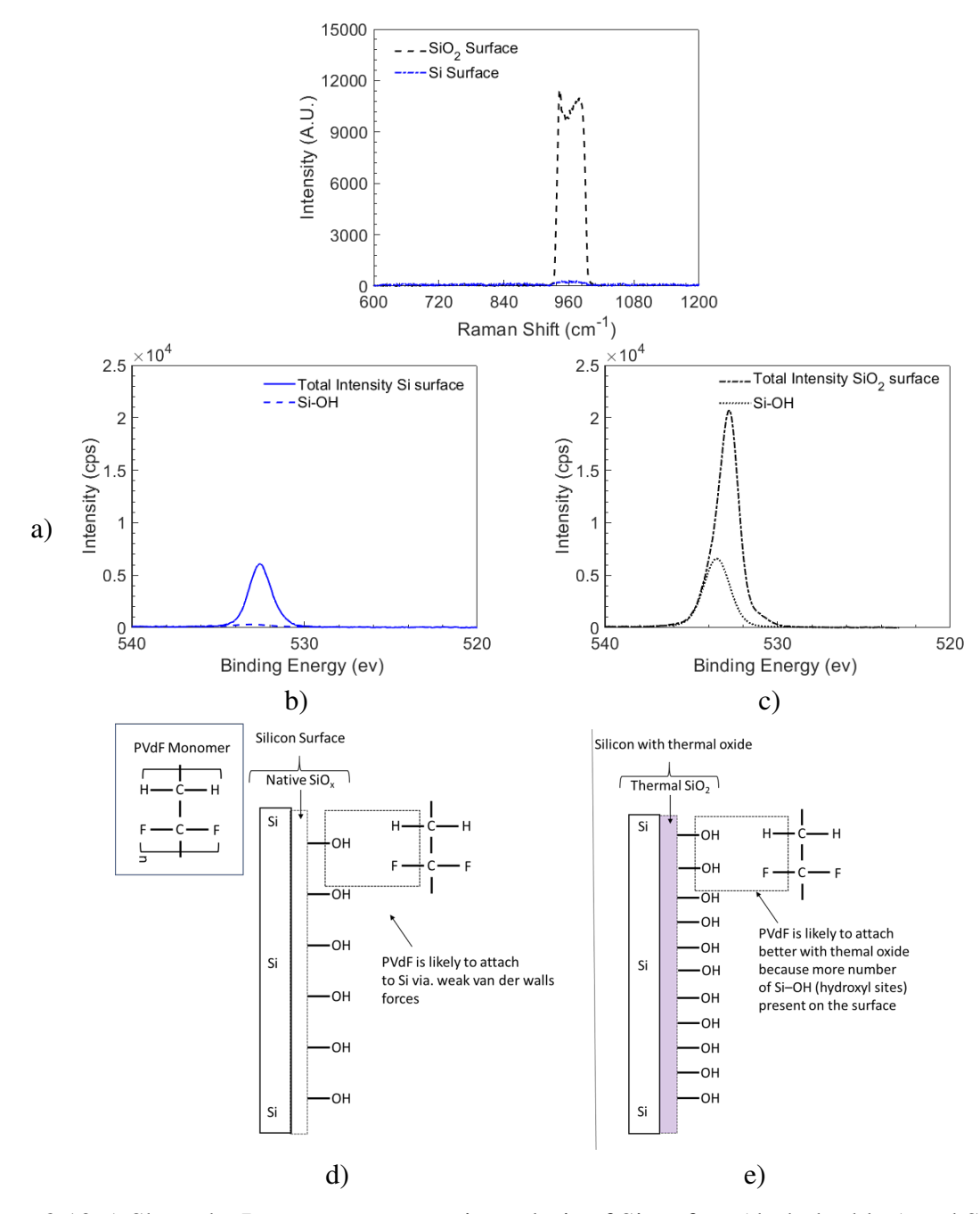


Figure 3.10 a) Show the Raman spectroscopic analysis of Si surface (dash dot blue) and SiO_2 (dashed black line) surface where the peak at 975 cm⁻¹ corresponds to Si-OH group. The relative intensity comparisons show that the concentration Si-OH is higher on SiO_2 compared to Si. The b) and c) are the XPS spectra focusing on O1s peak conducted on bare Si (solid blue) and SiO_2 (dashed black) surface. Here the Si-OH peak (at 533 eV) deconvoluted from the O1s peak of survey scan is and compared for both Si and Si surface. The figs. d) and e) are the schematic showing the likely mechanism of adhesion between PVdF binder to Si surface with native oxide, and thermal oxide SiO_2 on Si surface.

in the FE analysis. The measured pressure corresponding to the onset of delamination in three different rectangular samples is presented in the Table. 5 along with the predicted critical pressure from FE analysis using G_c criterion. It can be noted that the failure pressure was predicted very well in four sample with a maximum error of 12%. This prediction verifies that the obtained energy release rate is independent of geometry and support our argument that G_c as a failure criteria for binder/active material interface delamination.

It should be noted that the phase angle of the plane strain samples at failure is also reported in the table 5 using VCCT. It is important to note that phase angle is critical in failure prediction as G_c is a function of ψ_G and to accurately predicted failure pressure, G_c for all angles of ψ_G should be characterized. It is observed here by changing the geometry, the phase angle increased which can indicated the error obtained in the predicted pressure. Further experimentation is required in which varying the thickness of film can change the phase angle [89]. This analysis is important since the literature investigating the binder/active material interface based on scratch tests and peel test do not report how the critical parameters is influenced. Hence, when considering critical strain energy G_c as criteria for failure prediction, ψ_G should be associated with it.

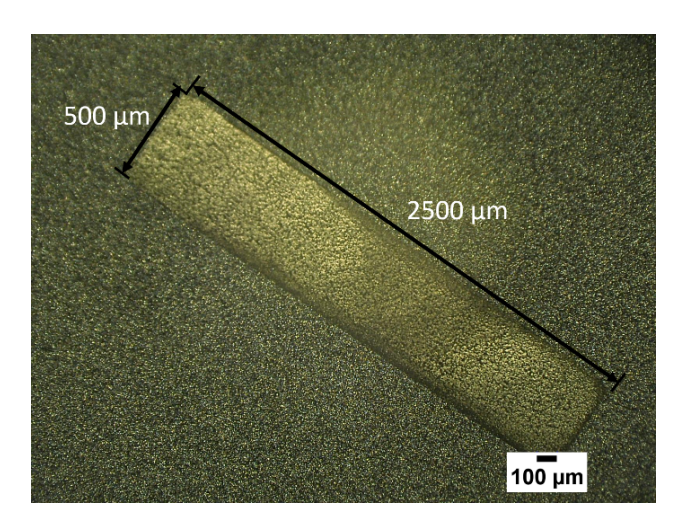


Figure 3.11 Rectangular PVdF film sample prepared following the fabrication process outlined above.

The ability to predict the binder/active material interface failure, as demonstrated above, will enable significant advantages to designing durable battery electrodes. The critical strain energy

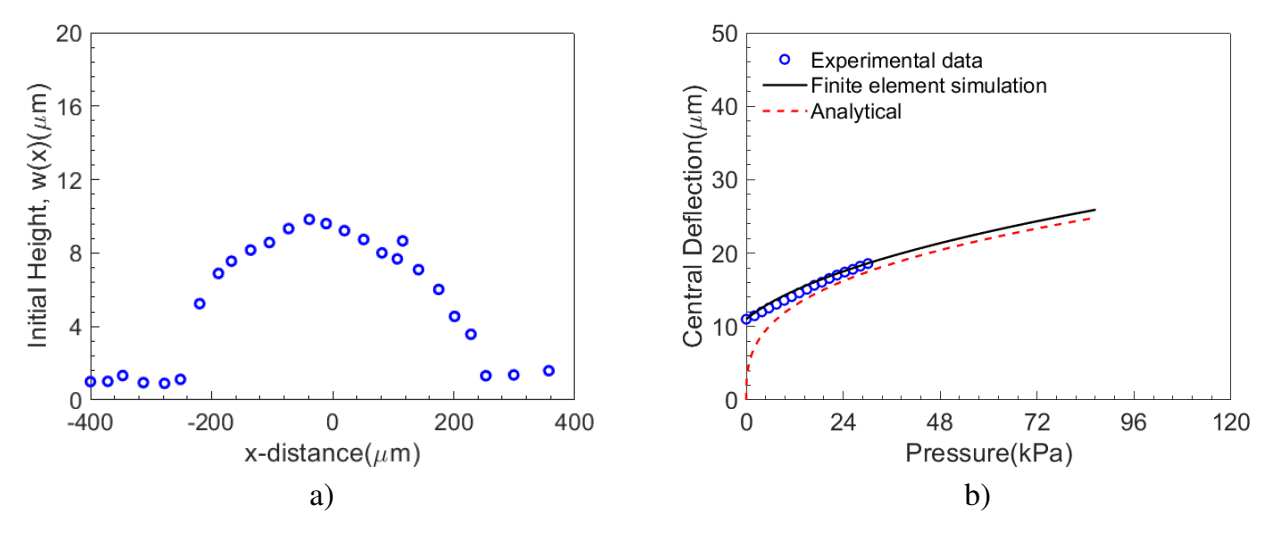


Figure 3.12 (a) The initial profile of rectangular sample (b) Comparing the obtained total deflection to finite element simulation and analytical solution.

release rate Gc is a fundamental property provided by the blister test and this allows to incorporate interface fracture mechanics into multiphysics model developed to understand and mitigate the degradation phenomena in composite lithium-ion battery. This indeed shows that G_c parameter can be used to study (1) The interface failure mechanism in batteries and, (2) can act as a design criteria for battery electrode architecture.

Table 3.5 Comparision of critical pressure value of rectangular PVdF films on SiO₂ substrate measured from experiments and the from the FE predictions using $G = G_c$ failure criterion.

Rectangular	Experimentally	Finite Element	Error (%)	Phase Angle at
Sample	Measured Pres-	Predicted Pres-		experimental fail-
	sure (kPa)	sure (kPa)		ure pressure
Sample 1	67	85.830	-21.94	72.593
Sample 2	76	84.012	-9.54	52.780
Sample 3	66	85.549	-22.85	72.355

3.7 Conclusion

In conclusion, there lacks a systematic method for studying interface failure for binder active material. Literature studies rely on qualitative methods like scratch test and peel test. These qualitative methods are good for comparison however, they lack fundamental understanding and fail to report data which can be used to design better battery interfaces. Here, we address this problem

by first, establishing an experimental methodology which quantifies the binder active material interface. Second, by providing critical energy release rate data using standard interface facture mechanics tests which can be used to study and design battery binder/active material interface. Blister test interface failure method is used to conduct experiments in which critical pressure of delamination is recorded along with blister profile using in-house Michelson interferometric method. The interface energy/critical strain energy release rate is calculated using finite element simulation and closed form analytical solutions. A model PVdF/SiO₂¬ interface which is relevant for current composite battery anodes is used for study.

The pressure-central deflection is the characteristic information obtained from experimental results. It is seen that obtained behavior does not follow the cubic pressure-central deflection relation (P \propto h³) generally followed by membranes. This is due to effect of initial condition i.e. non-flat initial profile and residual stress in film. Accounting for these effects in finite element simulation and analytical solution predicts the obtained behavior. The critical strain energy release rate is obtain using J-integral contours and analytical solution. For an axisymmetric sample the obtain energy is $2.457 \pm 0.398 \text{ Jm}^{-2}$ form finite element. The blister test experiments showed that PVdF behaves nominally elastic therefore simple analytical closed form solution results are quite close to finite element. The discrepancies associated with the mean data in finite element and analytical solution is due to assumptions associated with analytical equation therefore, the finite element mean is an accurate value. To verify this result, a rectangular (plane strain) samples are tested and its critical pressure of delamination is predicted. A good prediction for critical pressure obtained shows the robust nature of G_c in spite of phase angle variation. This shows that critical energy release rate (G_c) is a fundamental parameter. Therefore, the experimental method developed is an effective tool to quantify the interface energy in binder/active material interface in lithium ion batteries.

The obtained PVdF/Si energy release rate is less compared to PVdF/SiO2 (2.4 Jm⁻²) this can be understood by the fact that PVdF bonds to Si via. van der waals forces. The bonding occurs between the F atom in PVdF chain and H atom of the -OH group on Si surface. The number of -OH group

present of SiO₂ is higher than compared to Si surface. Therefore, the higher concentration allows a greater number of sites for the F atom in PVdF chain to bond. This observation corroborates with the literature where PVdF modified with -OH or binders with higher -OH concentration bonds better with Si surface. The measurement of energy release rate via. blister test allows for this comparison and provides insights into bonding mechanism between binder and active material interface

The obtained result shows that quantification of interface energy is critical in understanding and designing better binder/active material interface in lithium ion batteries. This method can be used to understand effect of different electrochemical conditions on interface and can be extended to study and interfaces that exists in battery materials.

CHAPTER 4

INTERFACE FAILURE RESULTS UNDER ELECTROCHEMICAL CONDITIONS

4.1 Electrochemical Cycling of Interface Fracture Sample

Fig. 4.1a show the typical potential-time curve of a PVdF (Soaked)/Si sample (Fig. 4.1b) subjected to electrochemical lithiation i.e. lithium flux entering in Si, in the electrochemical cell shown in Fig. 4.1a. The potential immediately drops form the open circuit potential (OCP) ≈ 2.7 V when electrochemical cell is assembled to 0.6 V when galvanostatic current of 7.5 μ A is applied. This initial drop is due to resistance in the electrical circuit. This gradual decrease in potential after 0.6 V is attributed to SEI formation and diffusion of Li in Si. The inset in Fig. 4.1a shows that an undercooling effect where the potential drops below 0.11 V and increases to 0.115 V where it plateaus. The undercooling effect is observed due to phase transformation of crystalline (100) Si to amorphous Si [12]. The subsequent plateau is the lithiation (100) Si where the phase boundary moves in the crystalline layer [100, 101] as shown in schematic fig. 4.1c . In these experiments, the time of the potential plateau was controlled to 8 h so that enough lithiated Si layer was formed to measure interface failure between PVdF and lithiated Si.

4.2 Mechanical behavior of soaked PVdF film and PVdF/LixSi interface failure

Figure 4.2a shows the pressure-time behavior of soaked PVdF/LixSi sample when subjected to mass flow of Ar. This behavior remains linear for axisymmetric sample until complete failure i.e. soaked PVdF completely delaminated from LixSi surface. Similar behavior is observed for plane strain sample although some deviation from axisymmetric behavior is observed after certain pressure which could be due to crack front moving. Fig. 4.2b and 4.2c shows the central deflection (at x = 0) of soaked PVdF film when subjected to the Ar pressure along with the FE simulations. In both geometries, the deflection is significantly higher than the film thickness indicating a membrane behavior i.e. pure stretching and no bending [72]. The FE simulation was performed for both cases and compared against the measured data. The simulation matches up to a certain pressure after which a clear distinction is seen (around 5 KPa for axisymmetric and 7 KPa for plane strain). This

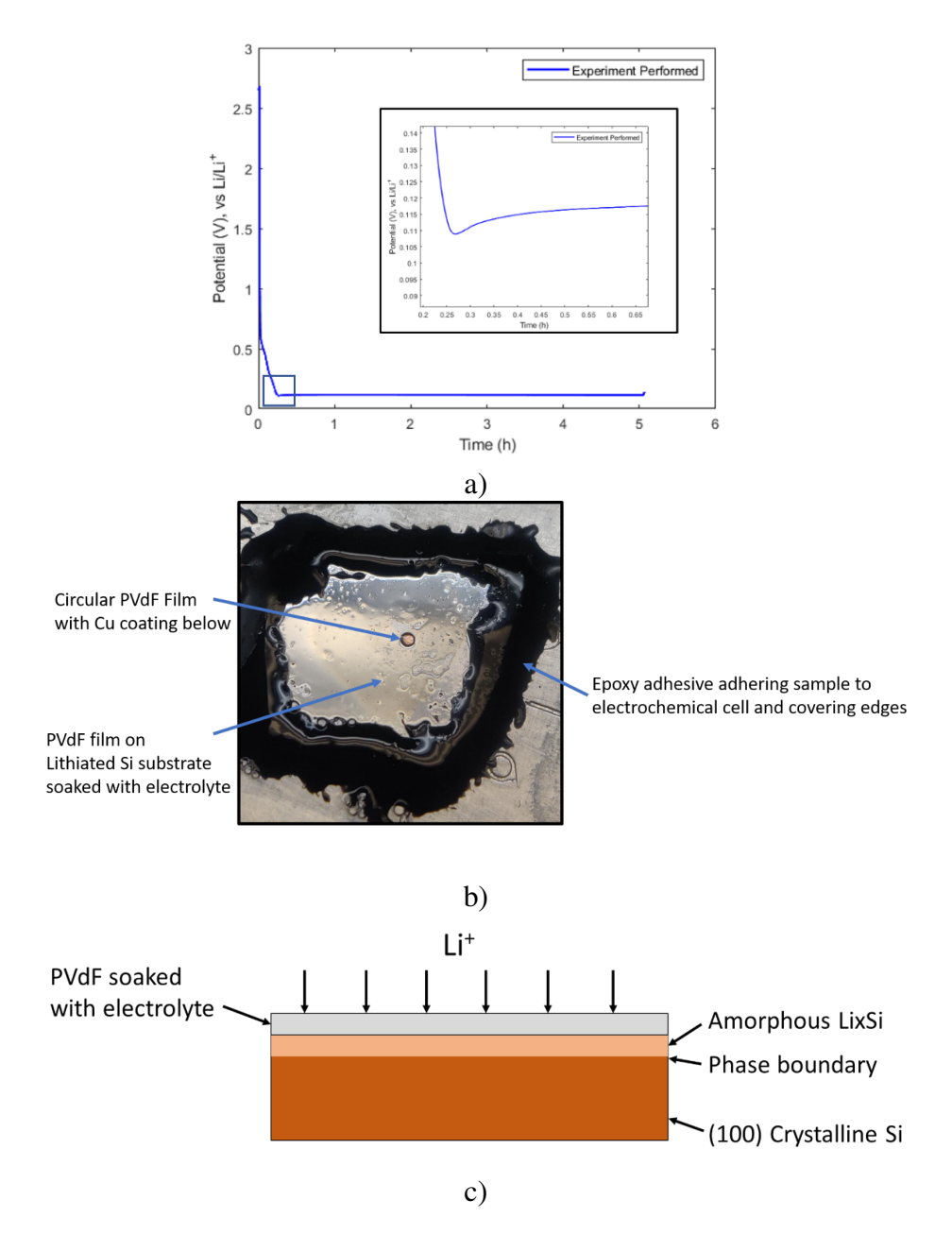


Figure 4.1 a) shows the potential vs time of a typical PVdF/Si sample subjected to electrochemical cycling. The inset shows an enlarged region of Potential-Time curve at 0.25 h showing undercooling effect which indicates phase formation. b) Shows the top view of actual PVdF/Si sample after being subjected to lithiation. c) Schematic showing the lithiaition of (100) Si sample.

deviation can be either due to inelastic response [102] of soaked PVdF membrane or interface failure where either the radius (in case of axisymmetric) or width (in case of plane strain) of sample has increased [89, 68, 103]. A close inspection of the recorded images shows that deviation occurs due to interface failure which is the crack initiation point. Also, plasticity was included in the FE model which shows that PVdF remains nominally elastic (plastic strain only exists near the crack tip) at crack initiation pressure which corroborates our evidence that deviation is due to crack initiation. Fig 4.2d show the schematic of failure and 4.2e shows an actual failed axisymmetric sample. The δa is the increase in radius/width and $\Delta W0$ is the corresponding deviation. This point is considered as the critical crack initiation point which is marked as red X in Fig. 4.2a.

The crack initiation pressure can be decomposed into pressure due to (i) the surface tension of electrolyte at interface and (ii) the adhesion of PVdF to LixSi. The surface tension of the electrolyte used (1:1:1 wt% mixture of EC:DC:DMC) can be assumed similar to EC:DMC which is 40.13 ± 0.20 mN/m[104] and contributes to 1.14 KPa for axisymmetric samples ($P_{st} = \frac{circumference}{area} \frac{x surface}{area} \frac{tension}{area}$) and or ≈ 1.28 KPa for plane strain samples($P_{st} = \frac{perimeter}{area} \frac{x surface}{area} \frac{tension}{area}$). The rest of crack initiation pressure i.e. 3.87 KPa for axisymmetric and 5.72 KPa for plane strain is due to adhesion at interface. To verify this observation samples delaminated films were subjected to applied pressure, here the film is adhering to the substrate due to surface tension[105]. The failure pressure observed in the surface tension is similar to ones calulated by surface tension assumption. For further analysis we will consider crack initiation pressure after immediate testing due to similar condition observed at the interface in composite battery electrodes.

The pressure increases beyond crack initiation (beyond 5 KPa up to peak) is due to resistant to crack propagation. Here the crack propagation was difficult to observe due to electrolyte at the interface. This resistance can be either due to the roughness at the interface created when Li flux intercalates Si substrate or due to presence of electrolyte at interface which adheres the soaked PVdF film to the Si substrate. It was also observed that the amount of electrolyte present in the experiment affect the propagation however, this did not affect the initiation. This propagation

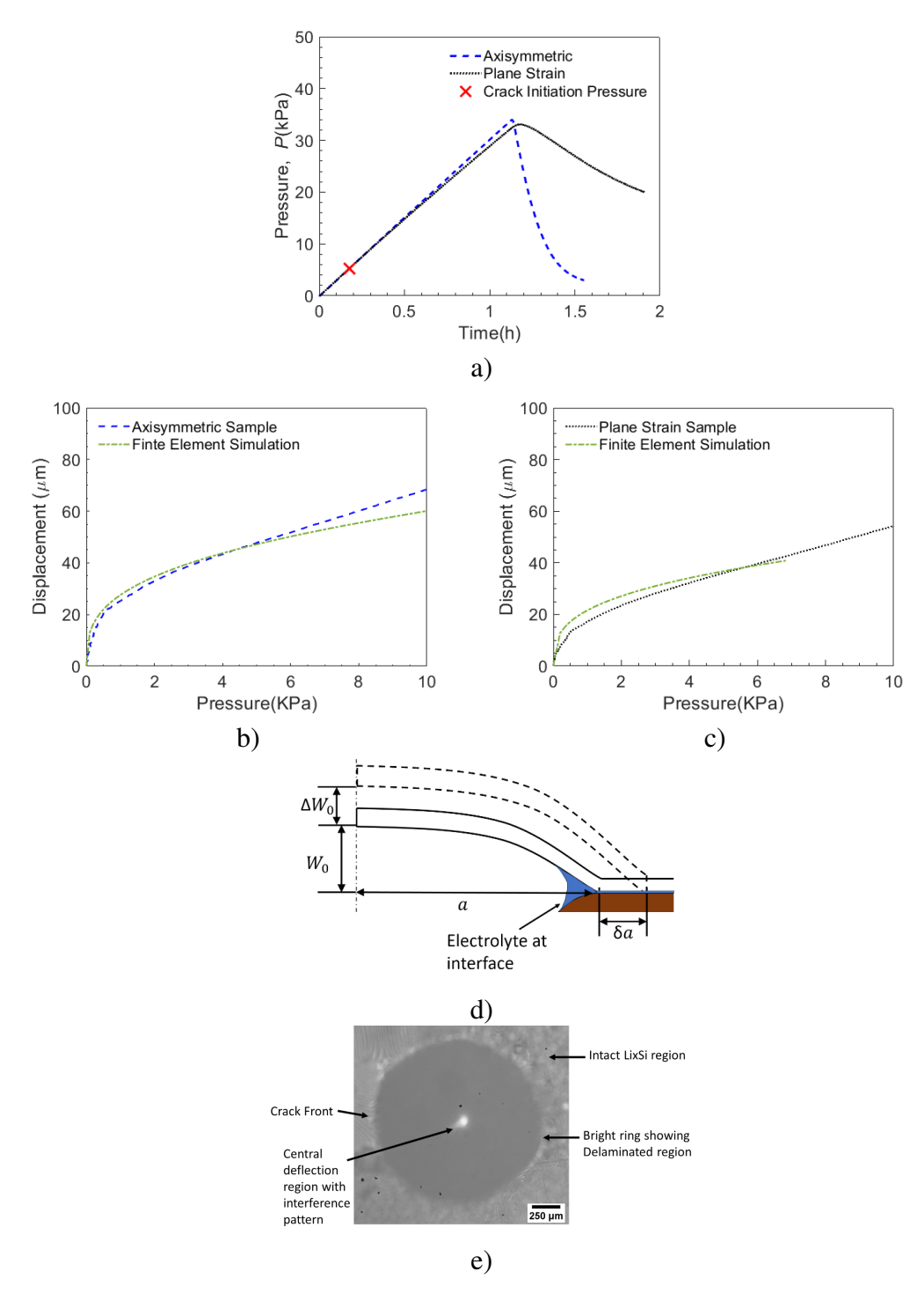


Figure 4.2 a) Shows the pressure-time behavior of a typical axisymmetric (dashed blue) and plane strain (dotted black) sample subjected to pressure due to argon. (b) The pressure-central deflection response of the typical axisymmetric sample (dashed blue) and FE simulation (dashed dot curve). c) The pressure-central deflection response of a typical plane strain same (dotted curve) along with FE simulations.d)Shows the schematic of the sample after failure where the presence of electrolyte at the interface affects propagation. e) An actual axisymmetric sample which shows crack initiation.

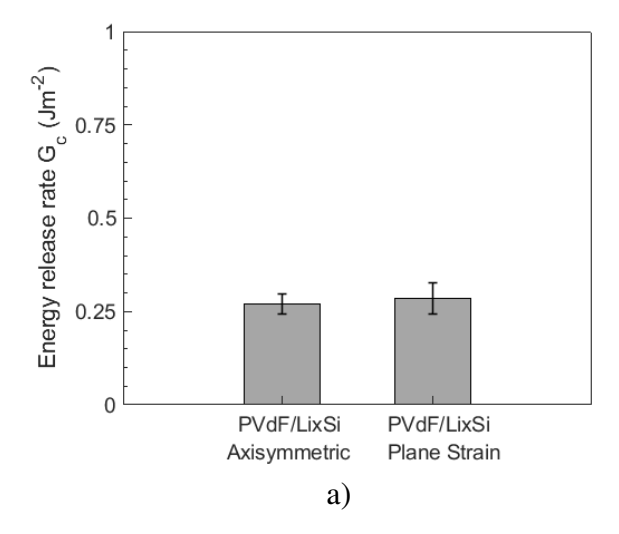
behavior varied from batch to batch in which some batch samples the pressure drop is immediately after initiation and in some cases the pressure drop is significantly after initiation. The observed effect can also be due to the removal of electrolyte from the PVdF soaked film as the electrolyte used in these experiments have low vapor pressure. However, the electrolyte at the interface between PVdF/lithiated Si cannot be removed as visually observed. In case of low electrolyte concentration in PVdF film, the behavior is reflected in the pressure-deflection curve where low electrolyte concentration films have a stiffer response compared to electrolyte saturated film which were complaint. These observed variations have been accounted for in the FE analysis where the Youngs Modulus of PVdF was varied and compared to the experimentally observed pressure-deflection.

It is to be noted that deflection behavior can be affected by two initial condition i.e. initial height and residual stress. The initial height means that the PVdF film is not flat are the beginning of experiments. Here our observation shows no initial height or minimal presence of initial height. Similarly, the residual stress is present in PVdF film when deposited on Si wafer in unsoaked conditions however, it is known the PVdF when it absorbs electrolyte it expands 4% in unconstrained condition which could cause relieving of any tensile residual stress present in the film. Therefore, in the FE analysis no initial height or residual stresses effects are considered.

The energy release rate (Gc) or adhesion of soaked PVdF/lithiated interface is evaluated at the crack initiation point using J-integral in the FE simulation. Figure 4.3a shows the Gc for the axisymmetric and plane strain samples. Since Gc from axisymmetric and plane strain sample are similar we compare the grand average with dry PVdF/Si interface. It can be clearly seen that the electrochemical cycling and electrolyte soaking of PVdF binder degrades the interface i.e. the Gc is lower compared to dry PVdF/Si.

4.3 Effect of electrolyte on the pressure-deflection and interface failure behavior

The electrochemical cycling of PVdF causes the decrease in the critical energy release rate Gc. This degradation arises from (i) introduction of electrolyte in PVdF and at the interface and (ii) electrochemical cycling which affects the interface. In order to determine the effect of introduction electrolyte, PVdF/Si samples were soaked in electrolyte and tested for interface failure without



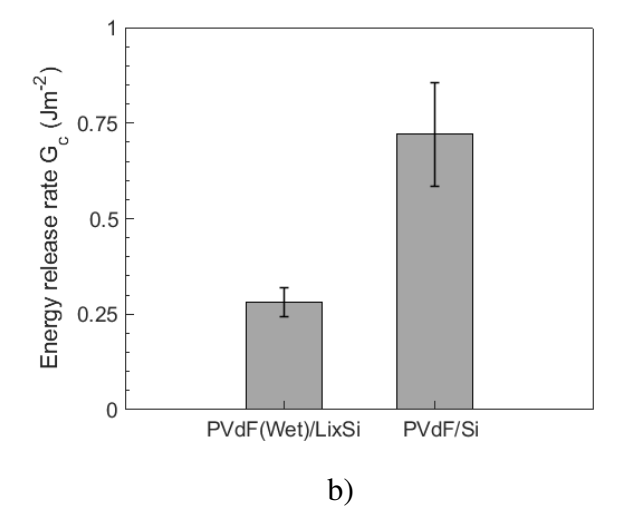
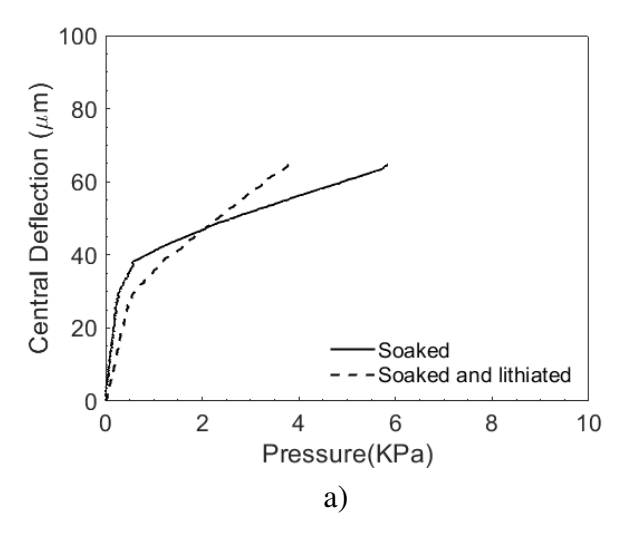


Figure 4.3 a) show the axisymmetric and plane strain energy release rate of electrolyte soaked PVdF/LixSi interface. b) The comparison of energy release rate of soaked PVdF/LixSi interface with dry PVdF/Si showing that soaking of electrolyte and lithiating Si reduces weaken the interface.

electrochemical cycling. Fig. 4.4a show the pressure-central deflection behavior of soaked PVdF compared to electrochemically cycled PVdF the deflection is shown until failure. The deflection of PVdF in both cases is similar, this is expected because sample were subjected to similar electrolyte and were completely soaked. In case of PVdF/lithiated Si samples, it is known that SEI forms as a diffused layer [?] and this could possibily affect the deflection behavior. The modulus of SEI [102] formed is similar to soaked PVdF modulus and therefore its effect can be negligible. In both cases, the modulus is taked as that of soaked PVdF[94] and FE comparision shows a similar behavior until failure leading to conclusion that in cased of soaked and electrochemical PVdF the film behaves similar.

It can be observe from Fig.4.4a that the failure pressure of soaked PVdF is slightly higher compared to lithiated samples. The failure pressure is controlled by the nature of the interface between PVdF and Si samples. In case of soaked PVdF samples, there is presence of electrolyte at the interface however, in lithiated samples, in addition to electrolyte, there is SEI formation. SEI is an irreversible layer formed due to decomposition of electrolyte [3, 10] at inteface and degrades the interface hence as obseved in Fig. 4.4b, the slight decrease in critical energy release rate is due to SEI formation.



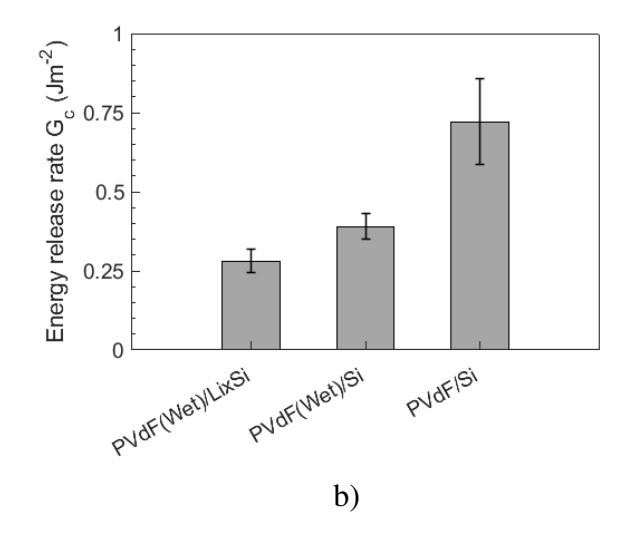


Figure 4.4 a) show the axisymmetric and plane strain energy release rate of electrolyte soaked PVdF/LixSi interface. b) The comparison of energy release rate of soaked PVdF/LixSi interface with dry PVdF/Si showing that soaking of electrolyte and lithiating Si reduces weaken the interface.

4.4 Possible Mechanism of interface Fracture

Fig 4.5a shows the schematic of PVdF adhering to Si via vander wall forces. The PVdF likely attached to Si-OH as was shown when comparing the adhesion of Si and SiO₂. For simplicity, here we are representing the adhesion of PVdF to Si as Fig. 4.5b. The introduction of electrolyte in sample cause PVdF swell [106, 107, 31] and peak strain obtained was 4% with the LP71 electrolyte. The electrolyte causes PVdF crystallinity to reduce i.e. reduce the %crystallinity of PVdF which can reduce the critical loads sustained by the interface(Yoo et al., 2003b). In addition, the stress-strain behavior of PVdF subjected to electrolyte changes i.e. Youngs modulus reduces significantly (e.g. from 1.6 GPa in dry to 0.3 GPa in soaked)(Chen et al., 2003a; Santimetaneedol et al., 2016a) also strain at failure is increase (e.g. 0.1 strain in dry condition to 0.3 strain in soaked condition). This could also be the reason that peak pressure significantly higher compared to crack initiation pressure and possible blunting at the crack tip which is observed in FE simulations. The electrochemical cycling involves lithium and electron transport in addition to the soaking of PVdF. The flux of lithium changes surface morphology of Si from atomically flat surface to porous surface network when lithium enter Si(Nadimpalli et al., 2015, 2013). In addition, the electron transfer and availability of electrolyte cause an irreversible layer called solid electrolyte interface

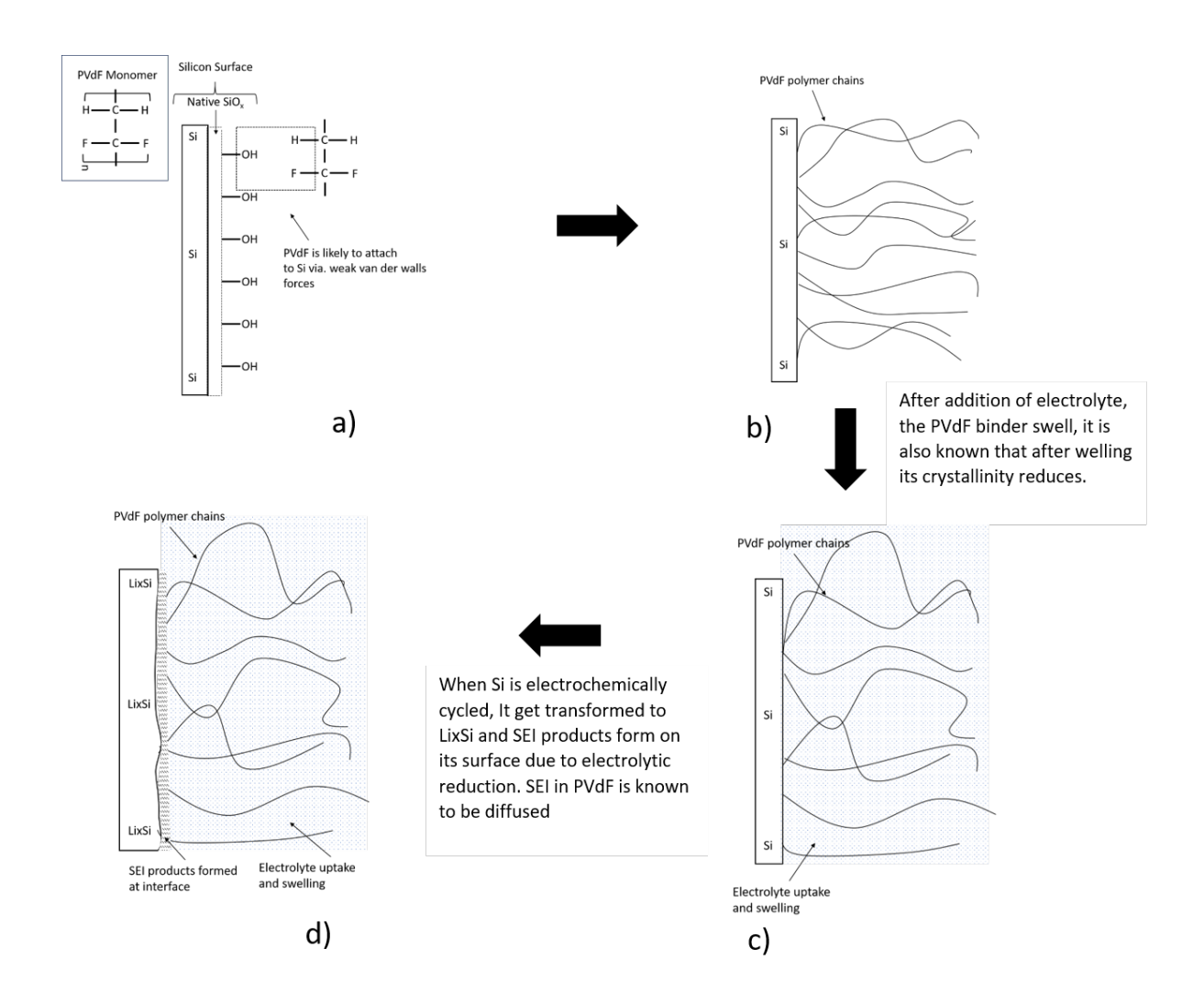


Figure 4.5 a) Shows that PVdF is likely to bond to via. van der walls forces of attraction, the polymer chain bonds to the -OH (hydroxyl) radicals present on Si surface. b) Here we present a simplified macroscopic representation of PVdF polymer chains attached to Si substrate. c) When PVdF absorbs electrolyte, is swells and polymer chains are redistributed. The swelling also causes interfacial stress at the surface which decreases the adhesion strength. The uptake of electrolyte which contains constituent such as EC, DC, and DMC which are polar and non-polar solvent can affect the charge distribution at the interface. d) Due to electrochemical reaction at the interface, the Li ions diffuse into Si and intercalates to form alloy of Si i.e. LixSi complete saturation of Si forms Li3.75Si. The interface can get roughened due to formation of diffusion pathways also at the interface due to decomposition of electrolyte, SEI forms at the interface which degrades the interface between swollen PVdF binder and LixSi interface.

(SEI) to form. XPS analysis conducted by Johnson et al. shows that SEI formation in PVdF/Si samples occurs inside the PVdF binder and at the interface due to electrolyte absorption. This SEI formation is likely to alter the interface fracture properties of PVdF/Si interface. The Youngs modulus associated SEI highly depends on the electrolyte composition used. Youn et al.[102] for LiPF6 in EC and EC+FEC obtained modulus to be 240 MPa and 430 MPa respectively using plane strain bulge test. The obtained modulus is similar to PVdF soaked modulus also the Cu film below PVdF stiffens the PVdF-Cu composite therefore SEI formation has minimum effect on the mechanical behavior of PVdF film hower as we see from 4.5b the SEI formation slightly decreases the energy release rate of the interface.

CHAPTER 5

MODELING THE CONSTITUTIVE BEHAVIOR OF ELECTRODES

5.1 Model formulation

5.1.1 Kinematics

This model is based on multiplicative decomposition of deformation gradient. This decomposition allows various phenomenas associated with solid deformation to be accounted. In case of high performance anodes (e.g. Si) used in state of the art lithium ion batteries, the stress shows a characteristic initial elastic deformation, follow by plastic deformation [13] when ions diffuse inside the anode. This deformation originates due to large volume expansion (e.g. 300% for Si) [[23]] when ions alloy with anodes. The mathematical representation [[108, 109, 110]] which can account for this is,

$$\mathbf{F} = \mathbf{F}^e \mathbf{F}^p \mathbf{F}^s \tag{5.1}$$

where $J = \det \mathbf{F} > 0$, $J^e = \det \mathbf{F}^e > 0$, $J^p = \det \mathbf{F}^p = 1$, and $J^s = \det \mathbf{F}^s > 0$. Here, \mathbf{F}^e is the deformation due to elastic stretching, \mathbf{F}^p is deformation due to plasticity, and $\mathbf{F}^s = (J^s)^{1/3}\mathbf{1}$, is the deformation gradient due to swelling with $J^s = 1 + \Omega(c_R - c_{R0})$. Here c_R is the molar concentration per unit reference volume, c_{R0} its initial concentration of ion in anode, and Ω the molar volume of the ion (Li or Na) which is diffusing in the anode. In case of Li-Ge [[15]] and Na-Ge [[39]] similar stress and volume expansion magnitudes have been observed therfore multiplicate decomposition theory can be futher applied.

5.1.2 Free energy

The contribution in this thermodynamic system incorporates the, energy due to solid solution formation when ion alloys with the host anode, and the corresponding elastic strain energy due to volume expansion. The justification of solid solution formation stems from the observation of Baggetto et al. [111] and Rakshit et al. [39] that no intermation phase formation occurs and the solid solution remains amorphouse during the reaction. A similar basis was used by Bucci et al.[61]

and Di Leo et al. [63] for Li-Si. Following literature, a single phase non ideal mixing solid solution formation energy is given as

$$\psi_{R}^{\text{chem}} = \mu^{0} c_{R} + R \vartheta c_{R,\text{max}} (\bar{c} \ln \bar{c} + (1 - \bar{c} \ln(1 - \bar{c}))) + c_{R,\text{max}} \sum_{n=2}^{7} a_{n} \cdot \bar{c}^{(n)}.$$
 (5.2)

Here μ^0 is the reference chemical potential, R is the gas constant, θ being the absolute temperature,

$$\bar{c} = c_{\rm R}/c_{\rm R,max} \in [0, 1],$$
 (5.3)

is the normalized concentration of Na in Ge with c_R being the molar concentration per unit reference volume and $c_{R,max}$ the maximum molar concentration per unit reference concentration. In (5.2) a_n represents the fitting coefficients which quantifies the non-ideal free energy of mixing and needs to be determined experimentally for individual systems. We have determined this for both Li-Ge and Na-Ge following the procedure similar to [61] et al..

The observation from thin film stress measurement of [39] et al. shows the behavior of Na-Ge is isotropic, therefore following [112], the elastic free energy isotropic material is taken as

$$\psi_{R}^{\text{mech}} = G(\bar{c})|\mathbf{E}_{0}^{e}|^{2} + \frac{1}{2}K(\bar{c})(\text{tr}\mathbf{E}^{e})^{2}$$
(5.4)

Here, \mathbf{E}^{e} is the logarithmic elastic strain tensor given as,

$$\mathbf{E}^{e} = \sum_{i=1}^{3} (\ln \lambda_{i}^{e}) \mathbf{r}_{i}^{e} \otimes \mathbf{r}_{i}^{e}$$
(5.5)

where \mathbf{r}_i^e is the orthonormal eigenvectors of \mathbf{E}^e and λ_i^e are the corresponding eignenvalues. In (5.4) $G(\bar{c})$ and $K(\bar{c})$ represents the concentration dependent shear modulus and bulk modulus for Ge. A similar free energy for was used be DiLeo et al.[63] to model the behavior of Li-Si.

The total free energy of the system which is sum of chemical and mechanical contribution and is written as

$$\psi_{R} = \psi_{R}^{\text{chem}} + \psi_{R}^{\text{mech}} \tag{5.6}$$

5.1.3 Constitutive equation

5.1.3.1 Constitutive equation of Mandel and Cauchy stress

The free energy determines the stress and chemical potential of the system. The stress which satisfies the free energy imbalance is given as

$$\mathbf{T}^{e} = 2 \frac{\partial \psi_{R}(\mathbf{C}^{e}, c_{R})}{\partial (\mathbf{C}^{e})}.$$
 (5.7)

where ψ_R is total free energy from (5.6) and \mathbf{C}^e is the right Cauchy Green tensor which is given as

$$\mathbf{C}^e = \sum_{i=1}^3 \lambda_i^{e^2} \mathbf{r}_i^e \otimes \mathbf{r}_i^e, \tag{5.8}$$

with λ_i^e being the elastic stretch tensor and $(\mathbf{r}_1^e, \mathbf{r}_2^e, \mathbf{r}_3^e)$ the orthonormal eigenvectors of \mathbf{C}^e . The equations 5.7 and 5.8 is obtained from [?] for a viscoplastic material similar to anodes in this paper. The Cauchy stress (\mathbf{T}^e) or true stress tensor quantifies the deformation in the current configuration i.e. considering the current volume expansion whereas the Piola stress

$$\mathbf{S} = J\mathbf{T}\mathbf{F}^{-\mathsf{T}},\tag{5.9}$$

is defined in reference configuration with respect to pristine film dimension.

In formulating the theory, a stress tensor called Mandel stress defined as

$$\mathbf{M}^e \stackrel{\text{def}}{=} \mathbf{C}^e \mathbf{T}^e. \tag{5.10}$$

The Mandel stress can account which is symmetric for isotropic materials can account for the plastic flow in the material. The relation between Mandel and Cauchy stress is

$$\mathbf{M}^{e} = J^{e^{-1}} \mathbf{F}^{e \mathsf{T}} \mathbf{T} \mathbf{F}^{e \mathsf{T}}. \tag{5.11}$$

Following (5.7), (5.8), (5.10), defining logarithmic strain tensor as

$$\mathbf{E}^{\mathbf{e}} \stackrel{\text{def}}{=} \sum_{i=1}^{3} E_{i}^{e} \mathbf{r}_{i}^{e} \otimes \mathbf{r}_{i}^{e}$$
 (5.12)

where $E_i^e \stackrel{\text{def}}{=} \ln \lambda_i^e$, the Mandel stress is written as

$$\mathbf{M}^{\mathbf{e}} = J^{s^{-1}} \frac{\partial \psi_{\mathbf{R}}}{\partial \mathbf{F}^{\mathbf{e}}} = 2G(\bar{c}) \mathbf{E}_{0}^{e} + K(\bar{c}) (\operatorname{tr} \mathbf{E}^{e}) \mathbf{1}$$
 (5.13)

this is obtained from eqn. (5.6).

Similarly, the Cauchy stress can be written as

$$\mathbf{T} = J^{e^{-1}} \mathbf{R}^{\mathbf{e}} \mathbf{M}^{\mathbf{e}} \mathbf{R}^{\mathbf{e} \mathsf{T}} = J^{e^{-1}} \Big(2G(\bar{c}) \mathbf{E}^{e} + K(\bar{c}) (\operatorname{tr} \mathbf{E}^{e}) \mathbf{1} \Big). \tag{5.14}$$

Here the shear modulus(G) and bulk modulus(K) is a function of normalized concentration(\bar{c}). The constant G and K are relates to Young's modulus E as $G = E/(2(1+\nu))$ and $K = E/(3(1-2\nu))$. It is well known that when ions(Li or Na) alloys with solid solution anode the modulus varies with concentration. [113] showed that biaxial modulus variation can be well described using rule of mixture. Here, we follow the modulus and poisson ratio change similar to [61].

$$E(\bar{c}) = E_0 + E_1 \log \left(1 + \frac{\bar{c}}{\bar{c_0}} \right), \quad \text{and} \quad \nu(\bar{c}) = \nu_0 + \nu_1 \log \left(1 + \frac{\bar{c}}{\bar{c_0}} \right),$$
 (5.15)

$$a = \frac{x}{x+1} = \frac{x_{\text{max}}\bar{c}}{x_{\text{max}}\bar{c}+1}$$
 (5.16)

with a being the atomic fraction of ion in Ge.

5.1.3.2 Constitutive equation of chemical potential

The reaction of Li or Na against Ge is primarly to minimize the free energy. The free energy minimization is obtain when chemical potential is zero. Therefore, we define the chemical potential the anode using the relation given by [114]. The relation is given as

$$\mu = \frac{\partial \psi_{\rm R}}{\partial c_{\rm R}} + \bar{p}\Omega \tag{5.17}$$

where

$$\bar{p} = -\frac{1}{3} \text{tr} \mathbf{M}^e, \tag{5.18}$$

which is the mean normal pressure.

Here the terms in eqn.(5.17) includes the contribution due to chemical reaction and stress and futher the chemical potential is constrained by the hydrostatic pressure in the system originating from volume expansion.

The chemical potential now can be written as

$$\mu = \frac{\partial \psi_{R}}{\partial c_{R}} - \Omega \frac{1}{3} \text{tr} \mathbf{M}^{e}$$
 (5.19)

and based on the free energy form (5.6) is given as

$$\mu = \mu_0 + R\vartheta \ln \left(\gamma \frac{\bar{c}}{1 - \bar{c}} \right) - K(\bar{c})\Omega \text{tr} \mathbf{E}^e$$

$$+ K(\bar{c}) \ln(1 + \Omega c_{\text{R,max}}(\bar{c} - \bar{c}_0))$$
(5.20)

The chemical contribution for eqn. (5.20) is similar to the form used by [58], [61] and [63], however, the mechanical contribution is derived from (5.13).

Here γ is the activity coefficient given by [61] as

$$R\theta \ln \gamma = \sum_{n=2}^{7} a_n \cdot n \cdot \bar{c}^{(n-1)}. \tag{5.21}$$

5.1.3.3 Evolution equation for \mathbf{F}^p

The free energy or the chemical potential defined accounts for energy stored in the system and retained during cycling. Additional contribution comes through the plastic deformation which

dissapates energy during cycling. This dissapation needs to be accounted as shown by [13] for Li-Si that it account for nearly half of the total losses. Similar observation have been shown by [39] for Li-Ge and Na-Ge system. The constitutive relations here defines how mechanical dissapation is accounted. With the assumption that plastic flow is incompressible $J^p = 1$, and knowing that the material is isotropic, this futher gives us that the plastic flow is irrotational $\mathbf{W}^p = 0$ (spin tensor). Therefore, the equation for plastic distortion \mathbf{F}^p is given as

$$\dot{\mathbf{F}}^p = \mathbf{D}^p \mathbf{F}^p \tag{5.22}$$

$$\mathbf{D}^p = \sqrt{\frac{3}{2}} \dot{\epsilon}^p \mathbf{N}^p, \tag{5.23}$$

which is the plastic stretching tensor and $\mathbf{N}^p = \sqrt{\frac{3\,\mathbf{M}_0^e}{2\,\bar{\sigma}}}$ defines the direction of plastic flow. Here the $\dot{\epsilon}^p$ gives the equivalent tensile plastic strain rate and $\bar{\sigma}$ gives the equivalent stress. The change in flow strength following [63] is

$$\bar{\sigma} = Y(\bar{c}) + Y_{\star} \left(\frac{\dot{\epsilon}^p}{\dot{\epsilon}_0}\right)^{1/m}.$$
 (5.24)

Here, Y_{\star} is a positive-valued stress dimensioned constant with $Y(\bar{c})$ being the concentration dependent yield strength. The $\dot{\epsilon}_0$ is the reference tensile plastic strain rate, and m is the strain rate sensitivity of the material. The equation now for the plastic strain rate can be written as

$$\dot{\epsilon}^{p} = \begin{cases} 0 & \text{if } \bar{\sigma} \leq Y(\bar{c}) \\ \dot{\epsilon}_{0} \left(\frac{\bar{\sigma} - Y(\bar{c})}{Y_{\star}} \right)^{m} & \text{if } \bar{\sigma} > Y(\bar{c}). \end{cases}$$
 (5.25)

The concentration dependent yield strength changes is taken as

$$Y(\bar{c}) = Y_{\text{sat}} + (Y_0 - Y_{\text{sat}}) \exp\left(-\frac{\bar{c}}{\bar{c}_{\star}}\right), \tag{5.26}$$

In this case the three independent parameter $\{Y_0, Y_{\text{sat}}, \bar{c}_{\star}\}$ which needs to be obtained by fitting the experimental data.

5.1.3.4 Constitutive equation for mass flux

To define the boundary conditions on the system, we follow the procedures used by [115] and [63]. External boundary conditions applied in case of battery experiments is current or potential, which relates to boundary flux applied to the system. We neglect the effect of electric field which was considered by [58] and assume that the current or potential directly influences the species flux. In regards, the spatial flux \mathbf{j} of the diffusing species (Li or Na) is defined as

$$\mathbf{j} = -m \operatorname{grad} \mu. \tag{5.27}$$

A galvanostatic experiment is generally conducted to study the electrodes electrochemical and stress behavior. In that case, the current i.e. the flux remains constant which through eqn. (5.27) directly influences the chemical potential (refer eqn. (5.20)). Considering the material to be isotropic therefore, the mobility tensor(m) reduces to a scalar. The influence of external flux boundary condtion to the internal diffusion is related by

$$m = \frac{D_0}{R\vartheta}c(1-\bar{c}). {(5.28)}$$

Here, D_0 is the diffusion coefficient and $c = J^{-1}c_R$. It is straightforward that the concentration of diffusing atoms in the anode influences the diffusion response i.e. the mobility is higher in pristine sample compared to near saturation.

5.1.4 Electrochemical Kinetics

The prescribed flux on the surface is governed by the interfacial electrochemical kinetics (Fig. 1.4). A general relation between flux and current density is given as

$$I = -F\check{j} \tag{5.29}$$

where I is the applied current per unit area and is constant in case of galvanostatic experiments, F is the Faraday constant which is charge carried by a mole of electrons, and \check{j} is surface flux. In a galvanostatic experiment, the applied current or flux of active species can be distributed to two types of reaction, (i) the main reaction which governs the intercalation/alloying, (ii) the side reaction which contributed to the irreversible loss of ions e.g. the SEI formation, and (iii) flux attributed to double layer capacitance which acts as a buffer. The applied current in terms of main, side, and double layer can be written as [66, 61]

$$I_{\rm app} = I_{\rm main} + I_{\rm side} + I_{\rm DL}. \tag{5.30}$$

The relation of main current (I_{main}) to the overpotential(η) is governed by Butler-Volmer kinetics which is defined as

$$I_{\text{main}} = I_{0,\text{main}} \left(\exp\left(-\alpha \frac{F\eta}{R\theta}\right) - \exp\left(1 - \alpha \frac{F\eta}{R\theta}\right) \right). \tag{5.31}$$

Here, α is the symmetry factor($0 < \alpha < 1$) and considering the redox reaction to be symmetric, we consider $\alpha = 0.5$. The overpotential($\eta = V - U$) is potential change required to drive an electrochemical reaction i.e. $U(\bar{c})$ is equilibrium potential and V is the external measured potential (in case of galvanostatic experiment). The coefficient $I_{0,\text{main}}$ is the concentration dependent exchange current density which relates to the redox reaction at the interface. Based on direction of externally applied current (positive or negative), either an oxidation or a reduction reaction dominates. The $I_{0,\text{main}}$ is givens as

$$I_{0,\text{main}} = F k_{0,\text{main}} (1 - \bar{c})^{\alpha} \bar{c}^{1-\alpha}$$
(5.32)

with the parameter k_0 defining the reaction rate constant which is determined through experiments. In addition to main reaction, the side reactions occurs at the interface and reduces the concentration of active ions participating in the main reaction. This reaction can be modeled using tafel kinetics as

$$I_{\text{side}} = I_{0,\text{side}} \exp\left(-\alpha_{\text{side}} \frac{F\eta_{\text{side}}}{R\theta}\right).$$
 (5.33)

Here $I_{\rm side}$ is the exchange current density for side reaction, and $\eta_{\rm side}$ is given as $\eta_{\rm side} = V - U_{\rm side}$ is the overpotential to drive the side reaction. The $I_{\rm side}$ similar to eq. 5.32 is also defined as $I_{0,\rm side} = Fk_{0,\rm side}(1-\bar c)^\alpha \bar c^{1-\alpha}$. It is to be noted that the side reactions always reduces the applied current density irrespective of main reaction direction. To obtain $I_{0,\rm side}$, procedure given by Sethuraman et al. [66] can be used. The side reaction kinetics is high in magnitude during formation cycles i.e. cycle ran after assembly of battery. A cyclic voltametry (CV) experiment during the first cycle provides the potential $U_{\rm side}$ where the side reaction effects originates and its magnitude increases as the surface potential (V) deviates from $U_{\rm side}$. In eqn. (5.33) $\alpha_{\rm side}$ can be assume to be 0.5.

In eqn. (5.31) and (5.33), it is critical to define equilibrium potential(U) and to obtain that we follow the relation,

$$U = V_0 - \frac{\mu}{F}. ag{5.34}$$

where V_0 is the stress free rest potential of the electrode, and chemical potential(μ) is obtain through the equation (5.20).

The transient nature to the electrochemical kinetics is provided by a double layer capacitance and the current assocated with double layer is defined as

$$I_{\rm DL} = C_{\rm DL} \frac{dV}{dt},\tag{5.35}$$

where $C_{\rm DL}$ is the capacitance associated with double layer. The simplified capacitance definition was obtained from [65, 66, 116].

5.1.5 Balance laws

To solve a multiphysics problem it is necessary to maintain equilibrium with each individual coupled physical phenomena. In this case, the coupling of stress and electrochemistry, a local

balance of stress and concentration needs to be maintained. The governing partial differential equation defining equilibrium are

1. The local balance of force for the macroscopic Cauchy stress

$$div\mathbf{T} + \mathbf{b} = \mathbf{0} \tag{5.36}$$

where \mathbf{b} is the non-inertial body force, and \mathbf{T} is the Cauchy stress given by 5.14. This follows the continuum mechanics basis where the Cauchy stress and body force needs to be maintained at each material point. In case of statics problem, there exist no intertia therefore $\mathbf{b} = 0$ which means that the Cauchy stress needs to be balanced at a material point.

2. The local balance of the species concentration is given as

$$\dot{c}_R = -J \text{div} \mathbf{j} \tag{5.37}$$

Here, the concentration of ions needs to balanced at the interface where the externally applied flux (\mathbf{j}) balances the diffusing ions in the body.

The equation outlined follows the multiphysics problem defined by [[114, 117]]. This problem is numerically implemented following the approach on [[115]].

The governing equation are numerically implemented using the following strong forms

1. The balance of momentum is described as

$$\operatorname{div}\mathbf{T} = 0 \quad \text{in} \quad B_t \times [0, T], \tag{5.38}$$

$$\mathbf{u} = \mathbf{\check{u}} \quad \text{on} \quad S_{\mathbf{u}} \times [0, T], \tag{5.39}$$

$$\mathbf{Tn} = \check{\mathbf{t}} \quad \text{on} \quad S_{\mathbf{t}} \times [0, T] \tag{5.40}$$

Here $S_{\mathbf{u}}$, and $S_{\mathbf{t}}$ denotes the complimentary subsurface on the boundary ∂B_t on the deformed body B_t .

2. The balance of ion concentration is described as

A pair of boundary condition in which the chemical potential is defined on S_{μ} and fluid flux on $S_{\mathbf{i}}$.

$$\dot{c}_R = -J \text{div} \mathbf{j} \quad \text{in} \quad B_t \times [0, T], \tag{5.41}$$

$$\mu = \breve{\mu} \quad \text{on} \quad S_{\mu} \times [0, T], \tag{5.42}$$

$$-\mathbf{j} \cdot \mathbf{n} = \dot{j} \quad \text{on} \quad S_{\mathbf{j}} \times [0, T]$$
 (5.43)

with $\mathbf{\check{u}}$, $\mathbf{\check{t}}$, μ , and \dot{j} prescribed function on \mathbf{x} and t. The initial data is taken as

$$\mathbf{u}(\mathbf{X}, 0) = \mathbf{u}_0(\mathbf{X}), \text{ and } \mu(\mathbf{X}, 0) = \mu_0(\mathbf{X}) \text{ in B}$$
 (5.44)

The equation 5.36 and 5.37 with 5.41 and 5.44 yield the initial and boundary value problem for displacement and chemical potential.

The numerical implementation was carried out using ABAQUS user element subroutine (UEL) for a linear isoparametric 4 node 2D axisymmetric element (UAX4), 2D plane strain element (UPE4), and 8 node 3D element (U3D8). The numerical implementation follows the description given be [115].

Additionally, the electrochemical kinetics is numerically implemented by solving eqn. (5.30).

5.2 Verification of Model

The coupled multiphysics problem of diffusion-deformation is complex in implementation and needs to be verified againt standard analytical solutions or a simplified numerical implementation of the problem. In this case, the verification was done against 1-D forms of the equation which were implemented in MATLAB. To verify this problem, individual components i.e. diffusion without deformation and vice versa needs to be compared.

5.2.1 Mechanical constitutive

Figure 5.1 and Fig. 5.2 compares the true stress - strain curves from a 1-D MATLAB implementation to a single element finite element implementation in ABAQUS. Here, deformation was applied at different strain rates with constant concentration (Fig. 5.1), and deformation at different concentration under same strain rate (Fig. 5.2).

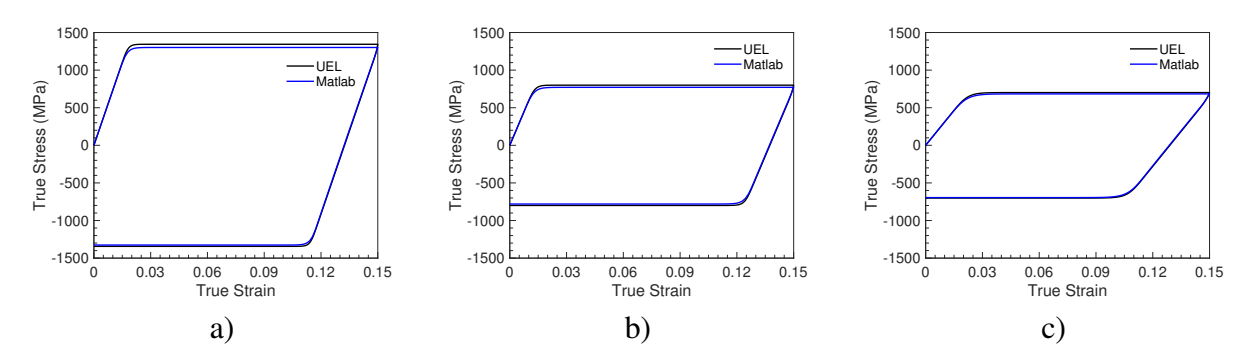


Figure 5.1 Comparing True Stress vs True Strain at 3 different normalized concentration(\bar{c}) a) 0.025 b) 0.1 c) 0.5 with data from 1-D Matlab and single element U3D8 at $\dot{\epsilon} = 0.001$.

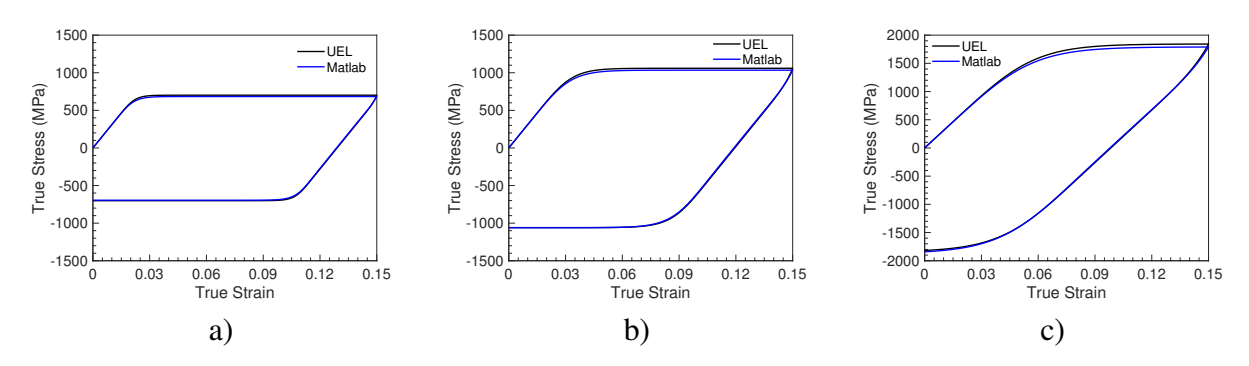


Figure 5.2 Comparing True Stress vs True Strain at 3 different strain rate($\dot{\epsilon}$) a) 0.001 b) 0.01 c) 0.1 with data from 1-D Matlab and single element U3D8 at $\bar{c} = 0.5$.

In absence of diffusion, the deformation problem is simplified to solve a viscoplastic problem. Here the plastic strain is considered as described in (5.25) with the yield strength given in (5.24). Using the material parameters given by [63] et al., Fig. 5.1 at constant $\dot{\epsilon}$ of 0.001 was obtained. We see a good agreement between the simulations performed by ABAQUS UEL and MATLAB. In addition, we can also see the characteristic of concentration dependence(Fig. 5.1) which is, as we

increase the normalized concentration(\bar{c}), the young's modulus decreases, also accompanied with a decrease in Yield strength and a delayed yielding at corresponding strain.

Figure 5.2 which is a comparison of True Stress vs True Strain behavior at different strain rate keeping the concentration(\bar{c}) constant at 0.5. Here, we see a good agreement between UEL and MATLAB with the classical strain rate dependence shown. Also, when strain rate is increased by a magnitude, the corresponding yield point and saturation strength increases with a delayed onset of plasticity. Figure 5.1 and Fig. 5.2 therefore verifies the deformation problem in absence of diffusion.

5.2.2 Diffusion constitutive

We verify the diffusion characteristics by suppressing the deformation. Here we compare the 1-D the diffusion equation (Fick's law) given as,

$$\frac{\partial \bar{c}}{\partial t} = \frac{\partial}{\partial x} \left(m \frac{\partial \bar{c}}{\partial x} \right),\tag{5.45}$$

where m being the mobility defined in 5.28 to solution obtained form ABAQUS finite element. The eqn 5.45 was implemented using finite difference method in MATLAB. Now a 1-D geometry simulated by a row a plane strain elements (UPE4) was solved using UEL subroutine in ABAQUS. The comparison of the obtained solutions is shown in Fig. 5.3. In both cases a concentration boundary condition applied was linearly ramped to a \bar{c} of 0.5. A good agreement if seen between the ABAQUS UEL and 1-D diffusion equation verifying the numerical implementation of the constitute flux equations.

5.3 Model Calibration

We now proceed to calibrate the model to the experimental data provided by [39] for Na-Ge system. Fig. 5.5 shows the experimental data required for calibrating the model. The data for stress change due to sodiation/desodiation in Ge was obtained following the substrate curvature method [[13]]. In this experiment, a galvanostatic current density (i.e. constant flux boundary condition) of 1 μ A cm⁻² was applied and potential was varied between 2.0 V and 0.001 V vs Na/Na⁺. During the galvanostatic cycling, the Ge thin film undergoes volumetric expansion due to diffusion of Na,

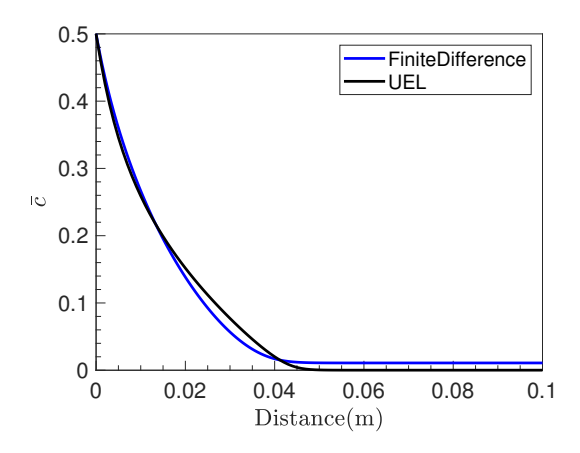


Figure 5.3 Comparing normalized concentration (\bar{c}) vs distance/length between ABAQUS UEL and 1D diffusion equation.

and its experimental data is provided by [39]. As a 100 nm Ge film is deposited on a 250μ m fused silica substrate (Fig. 5.4), the in plane expansion is constrained causing ths substrate to curve. The curvature is recorded using multi-beam optical sensing(MOS) method and the relation between curvature(κ) and stress is given by Stoney equation [[90]]

$$\sigma = \frac{1}{6} \frac{E_s}{(1 - \nu_s)} \frac{h_s^2}{h_f} \kappa. \tag{5.46}$$

Here E_s and v_s is Young's Modulus and Poisson ratio of fused silica substrate, with h_s and h_f begin the substrate and film thickness respectively. Note, to record the true stress we need to incorporate thickness change as area remain constant. The thickness change is accounted by linearly interpolating it with state of charge(SOC, $z \subset [0,1]$) where pristine Ge is 0 and Na saturated in Ge is 1. The equation for thickness change is

$$h_f = h_f^0 (1 + 2.6z), (5.47)$$

where h_f^0 is the film thickness (100 nm) at the start of the experiment and z is obtained as

$$z = \frac{\text{Capacity}}{\text{Maximum Capacity}}.$$
 (5.48)

To obtain capacity we calculate the charge accumulated (Q) due to electron flow

$$Q = \int I_{app} d\tau \tag{5.49}$$

where I_{app} begin the applied current. The charge can be converted to specific capacity using

Capacity =
$$\frac{Q}{V \times \rho}$$
 (5.50)

Here V is the initial volume of the thin film anode and ρ the density of Ge thin film.

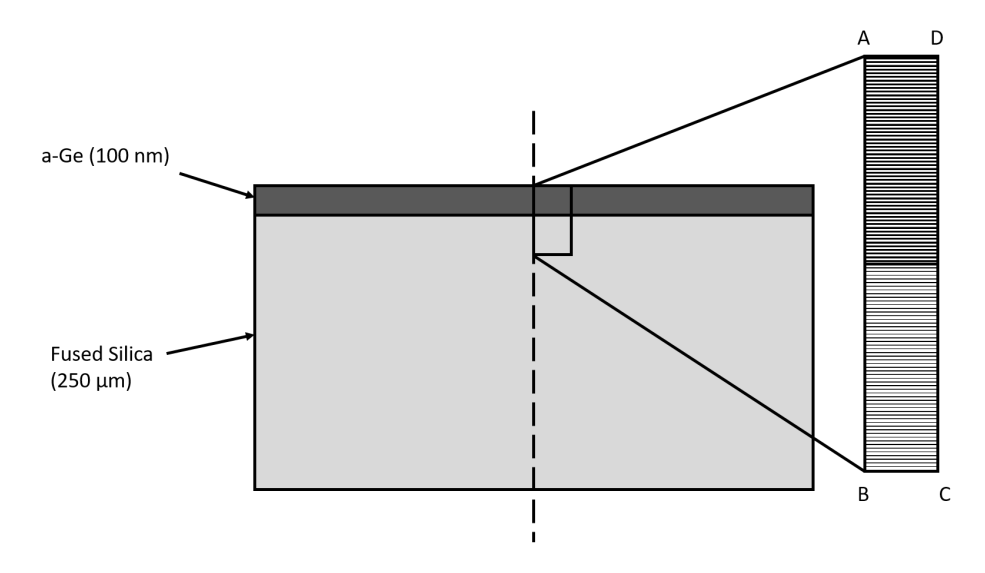


Figure 5.4 hows the mesh to simulate the thin film in-situ stress experiment.

To simulate the experiment we implement the finite element mesh as shown in Fig. 5.4. Here a single column of elements near the axis of symmetry was considered. The 100 nm Ge film was simulated using ABAQUS user element (UAX4) and the fused silica substrate was meshed using ABAQUS standard continuum elements (CAX4). The element size for Ge film was chosed to obey the diffusion lengths scales follwing $L = \sqrt{D_0 t}$ where L is element length, D_0 is diffusion coeffcient of Na in Ge, and t is the time scale. 100 element each of 1 nm was chosen to discretize the film. Similarly, the substrate was discretized with 20 elements each of 5 nm in size. The thickness of the substrate was reduced to minimize computation time, and this was done by adjusting the Young's modulus of the substrate to maintain stiffness. Mesh size refinement did not yield any significant change in result. The boundary condition applied to solve this problem are

- **Mechanical boundary condition:** In Fig. 5.4 on the left edge AB symmetric boundary condition is applied having fixed radial displacement. The right edge CD is applied with slider boundary condition keeping that edge parallel to AB. The bottom left node B is kept fixed in order to avoid the substrate moving in vertical direction.
- Flux boundary condition: A constant flux boundary condition applied to surface AD. The magnitude of flux applied was calculated based experimental current density and this takes into consideration the c-rate. In this case, the current density of 1 μ A cm⁻² is prescribed which is equivalent to c-rate of C/20.

Figure 5.5 and Fig. 5.6 shows the result obtained from the simulation and it comparison with experimental data. Fig.5.5a show the stress vs time comparision whereas 5.5b shows the stress vs capacity comparision. The parameters which gave the best fit are outlined in table 5.1

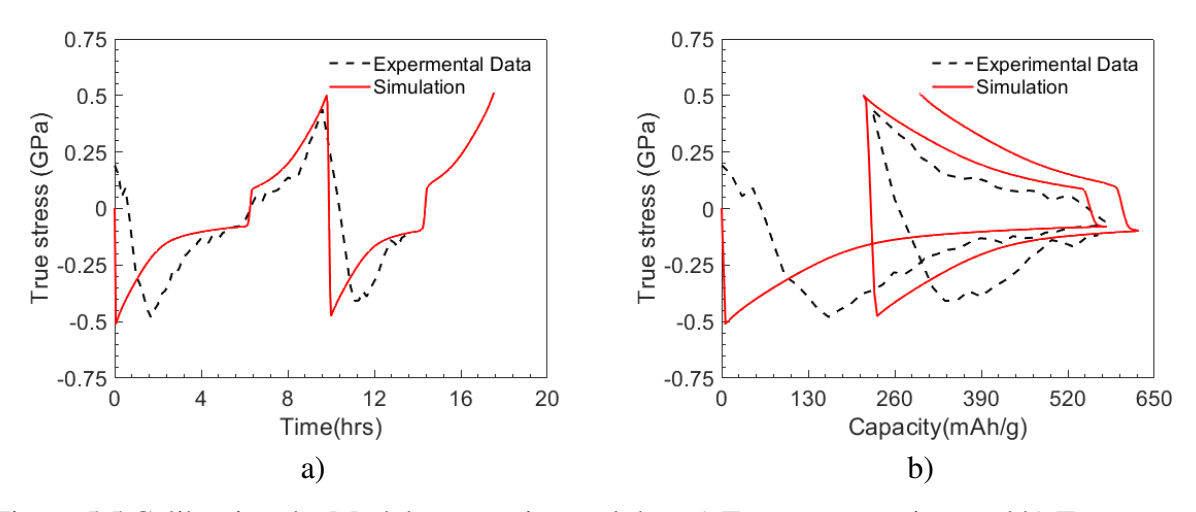


Figure 5.5 Calibrating the Model to experimental data a) True stress vs time and b) True stress vs Capacity for Na-Ge.

The model is robust to capture the stress changes in Li-Ge system. As seen the lithiation of pristine a-Ge produces a compressive stress unlike sodiation of a-Ge therfore the curve fit captured the first cycle stress change. The elastic loading/unloding shows a good match following the modulus change from eqn.5.15 and calibrating to the observations of [120]. A similar energy lost due to plastic deformation is seem from the experimental data and simulation, similarly, the losses

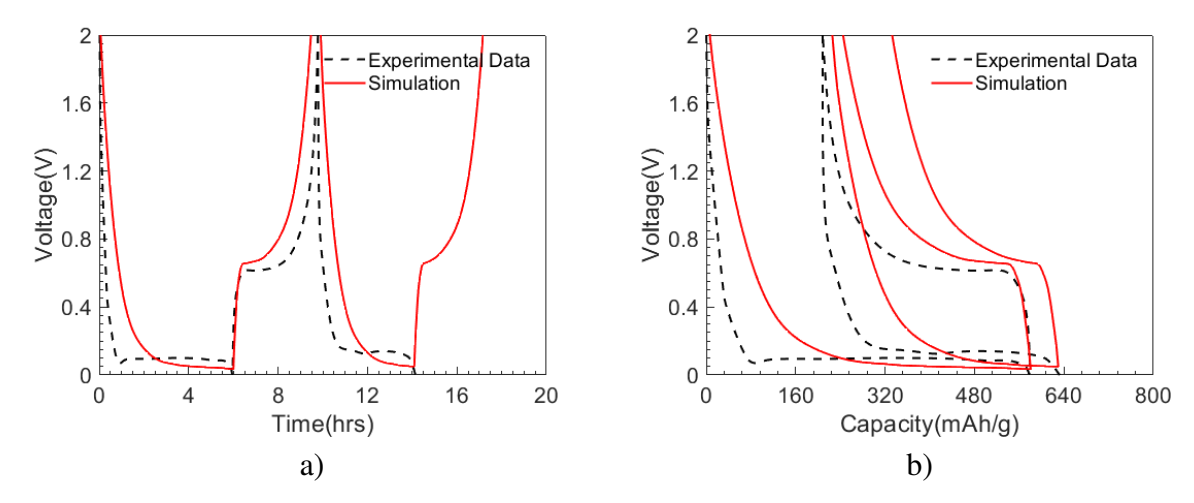


Figure 5.6 Calibrating the Model to experimental data a) Voltage vs time and b) Voltage vs Capacity for Na-Ge.

Table 5.1 Material parameters for Na-Ge calibration.

	Parameters	Values	Source
Chemical	$ ho_{\mathrm{Ge}}$	$7.337 \times 10^4 \text{ mol m}^{-3}$	Singman et al. (1984)
	$\Omega c_{ ext{Max}}$	2.39	[39]
	$c_{R,max}$	$27.5 \times 10^4 \text{ mol m}^{-3}$	[111]
	D_0	$1.6 \times 10^{-17} \text{ m}^2 \text{ s}^{-1}$	[118]
	[a ₂ ,a ₃ ,a ₄ , ₅ , ₆ , ₇]/F	[0.0109,1.8869,-4.4848,6.2981,-5.2075,1.8296] V	Fit Obtained
Elastic Parameters	E_{Ge}	80 GPa	
	$ u_{\mathrm{Ge}}$	0.214	
	$E_{ m Li}$	3.9 GPa	[119]
	$ u_{ m Li}$	0.3	
Plastic Parameters	Y_0	0.5 GPa	Calibration Fit
	$Y_{\rm sat}$	0.1 GPa	
	$\dot{\epsilon_0}$	2.3e-3	
	m	2.94	
	$ar{c_{\star}}$	0.70	
Electrochemical Parameter	k_0	$1.625 \times 10^{-8} \text{ mol s}^{-1}$	
	U_{side}	0.8 V	[39]
	$k_{0,side}$	$4 \times 10^{-13} \text{ mol s}^{-1}$	
	I_0/C_{dl}	$8 \times 10^{-6} \text{ V s}^{-1}$	

due electrochemical hysteresis is captured in the potential change due to lithiation/delithiation by adjusting the reaction kinetics parameter (k_0) .

From the obtained calibration, we can make the following observations as

- The obtained stress evolution (Fig. 5.5) during sodiation and desodiation of a-Ge predicted well with the assumptions of diffusion-deformation coupled with electrochemical theory.
- The compressive stress during sodation and tensile stress generated during desodiation was well captured during by our model and is repeatable for atleast 2 cycles.

- Although there is no published data of Youngs modulus and poisson ratio for change during sodiation/desodiation, with the assumption of modulus variation in eqn. (5.15), good elastic response during loading and unloading.
- The theoritical capacity of NaGe is 369 mAh g⁻¹ however, the capacity obtained in first cycle is well beyond the theoritical limit, which is contrary to the observation of Li-ion based anodes where the first cycle capacity obtained below theoritical limit. This high capacity obtained is due to irreversible reaction contributing significantly than Li-ion system. By adjusting the I_{0,side} the model is able to capture the losses in first cycle and decrease in magnitude of loss during subsequent cycle.
- The marching behavior i.e. the shift in capacity with each cycle as observerd in the experiments is captured due to implementation of Tafel side reaction kinetics which contributes to the capacity loss in each cycle.
- The potential variation is captured first by obtaining the activity coefficient from the equilibrium potential fit and secondly by adjusting the reaction rate kinetic parameter (k_0) which contributed to the area under the potential hyeteresis loop.

The focus currently on modeling the anodes for LIBs [[61, 63]] however with the emergence and demand of NIBs [[121]], there is a need to extend these models and incorporate different chemistries. The results in Fig. 5.5 and Fig. 5.6 shows the diffusion-deformation theory models can incorporate the electrochemical kinetics which helps in extendind these models to NIBs.

One of the characteristics of upcoming electrochemical system viz. NIB, Aluminum ion battery [[122]] is that they are not optimized for cyclibility, and large contribution comes from irreversible losses. These losses is measured by columbic efficiency where for Na-Ge is about 63% compared to 90% observed for Li system for first cycle, and they are attributed to the side reaction due to SEI formation. NIBs have large contribution due to side reaction, as shown in Fig. 5.6 the hysteresis losses in first cycle is significantly higher that subsequent cycle, this has been accounted by adjusting the $I_{0,side}$ which for sodiation of pristine a-Ge is higher than the steady state cycling. This compared

to LIB where $I_{0,side}$ can be same for first cycle and steady state cycling. The electrochemical kintics implementation helps in accounting this observation.

The characteristic effect of side reaction is shown by the marching behavior i.e. increase in capacity at end on sodiation or desodiation for each cycle or the moving of each cycle towards high capacity. This phenomenon originates due to side reaction [[123, 124, 125]] consuming active ion and since an infinte source of Na (counter electrode) exists the overall marching is towards higher capacity. Adjusting this $I_{0,side}$ also accounts for the marching behavior obseved during cycling [[66, 77]]. The implication is that fracture of electrodes can be investigated which provides addition area for side reaction and further contribute towards marching behavior [126].

We follow a similar calibration procedure to fit the experimental data of stress evolution during lithiation/delithiation of amorphous germanium [[15]]. Figure 5.7 and 5.8 shows the curve fit both the stress and potential change.

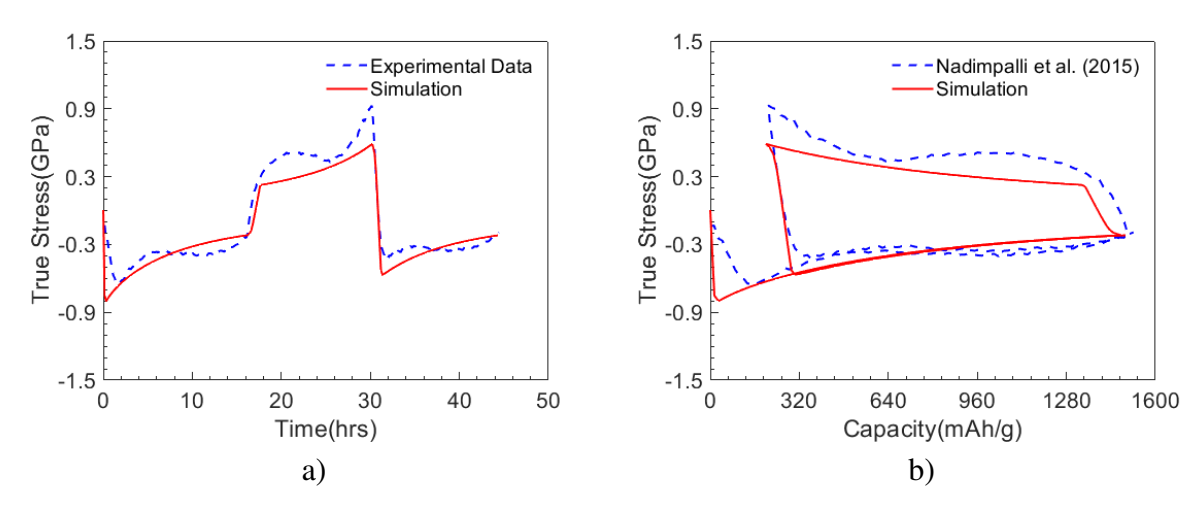


Figure 5.7 Calibrating the Model to experimental data a) True stress vs time and b) True stress vs Capacity for Li-Ge.

5.3.1 Side Reaction kinetics for marching behavior

Figure 5.9 shows the comparision of Na-Ge with and without the side reaction kinetics. The cycle 1 to 4 in all plots show that without including $I_{0,\text{side}}$ the marching behavior i.e. the shift in capacity with cycles cannot be captured. The characteristic effect of side reaction is shown by the marching behavior which increase the capacity at end potentials of sodiation or desodiation for each

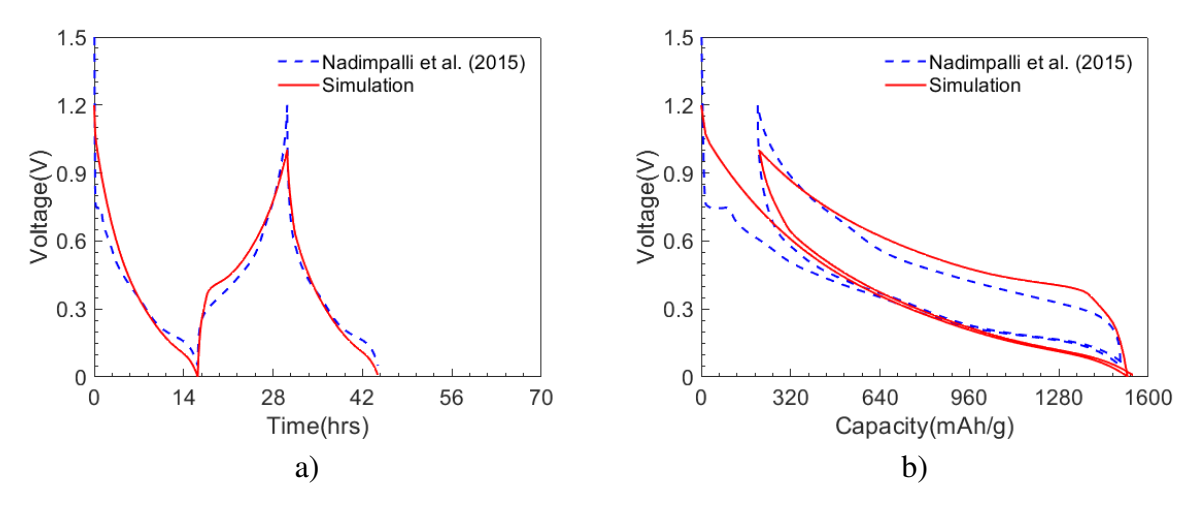


Figure 5.8 Calibrating the Model to experimental data a) Voltage vs Time and b) Voltage vs Capacity for Li-Ge

Table 5.2 Material parameters for Li-Ge calibration.

	Parameters	Values	
Chemical	$ ho_{\mathrm{Ge}}$	$7.337 \times 10^4 \text{ mol m}^{-3}$	
	$\Omega c_{ m RMax}$	2.625	
	c _{R,max}	$2.75 \times 10^5 \text{ mol m}^{-3}$	
	D_0	$1.5 \times 10^{-14} \text{ m}^2 \text{ s}^{-1}$	
	[a ₂ ,a ₃ ,a ₄ , ₅ , ₆ , ₇]/F	[1.9291,-2.1062,-0.4111,4.8441,-5.7364,2.2233] V	
Elastic Parameters	E_{Ge}	80 GPa	
	$ u_{ m Ge}$	0.214	
	$E_{ m Li}$	4.91 GPa	
	$ u_{ m Li}$	0.36	
Plastic Parameters	Y_0	0.7 GPa	
	Y_{sat}	0.6 GPa	
	$\dot{\epsilon}_0$	2.3e-3	
	m	2.94	
	$ar{c_{\star}}$	0.9	
Reaction Kinetics	$k_{0,main}$	$1.625 \times 10^{-7} \text{ mol s}^{-1}$	
	k _{0,side}	$5 \times 10^{-14} \text{ mol s}^{-1}$	
	I_0/C_{dl}	$1.3437 \times 10^{-5} \text{ V s}^{-1}$	

cycle or the moving of each cycle towards high capacity. This phenomenon originates due to side reaction [[123, 124, 125]] consuming active ion and since an infinte source of Na (counter electrode) exists, the overall marching is towards higher capacity. Adjusting this $I_{0,side}$ also accounts for the marching behavior observed during cycling [[66, 77]] which can be seen for the case of cycle 1 compared to subsequent cycles. The marching behavior shown by Na-ion battery system can be due to SEI solubility [[127]]. Relatively, the Li-ion batteries, shows minimal marching due to stable SEI formation after first cycle and follows cycling behavior shown similar to without side reaction in Fig.5.9. The $I_{0,side}$ acts as indicator of the side reaction contribution and with respect to main

reaction the $I_{0,\text{side}}$ of Na-Ge with respect to k_0 is 0.07 whereas for Li-Ge is 0.01. This mean the side reaction nealy 7% of the applied current for Na-Ge whereas incase Li-Ge is 1%.

The potential also changes when there is no flux applied i.e. during OCP condition. In OCP conditions, the ions is assumed to not diffuse in and out of Ge therfore the potential change occurs only through side reactions. Fig. 5.9a illustrates the potential vs time for Na-Ge with and without including side reaction and after 32 hrs, a OCP boundary condition is applied. We can see that when no side reaction is inluded, the potential reamins constant over however, when side reaction is included the potential increases, this is closer to experimental observation in literature. Although the change observed here is small, more experiments are needed in case Na-Ge system to verify the observation. Similarly the stress change can be accurately obtained when side reaction is included although more experiments on stress during OCP is needed to convey this point.

Here we can see the impact of including tafel side reaction kinetics in the marching behavior and during OCP condtion can be accurately obtained. Although inclusion of side reaction kinetics is still steady state in nature. We next explore how the transient kinetics impacts the stress and potential behavior of Na-Ge and Li-Ge systems.

5.4 Steady state vs Transient electrochemical kinetics

Figure 5.10 show the potential vs capacity and stress vs capacity for a Li-Ge system with and without the double layer capacitance. In Fig. 5.10a and 5.10c we see the including the double layer capacitance the potential response at the end potentials i.e. near 0.05 V or 1.2 V is closer to the experimental data as compared to without double layer. This clearly shows that when sudden changes occur at the end potential double layer involves and acts as a buffer which provides smoother transition. When a simulation is performed without the double layer, the end potential i.e. 0.05 V reaches earlier due to the absence of current associated with double layer. The true stress follows the similar path as the potential as seen in Fig.5.10b,5.10d, this is due to the stress-potential coupling[42].

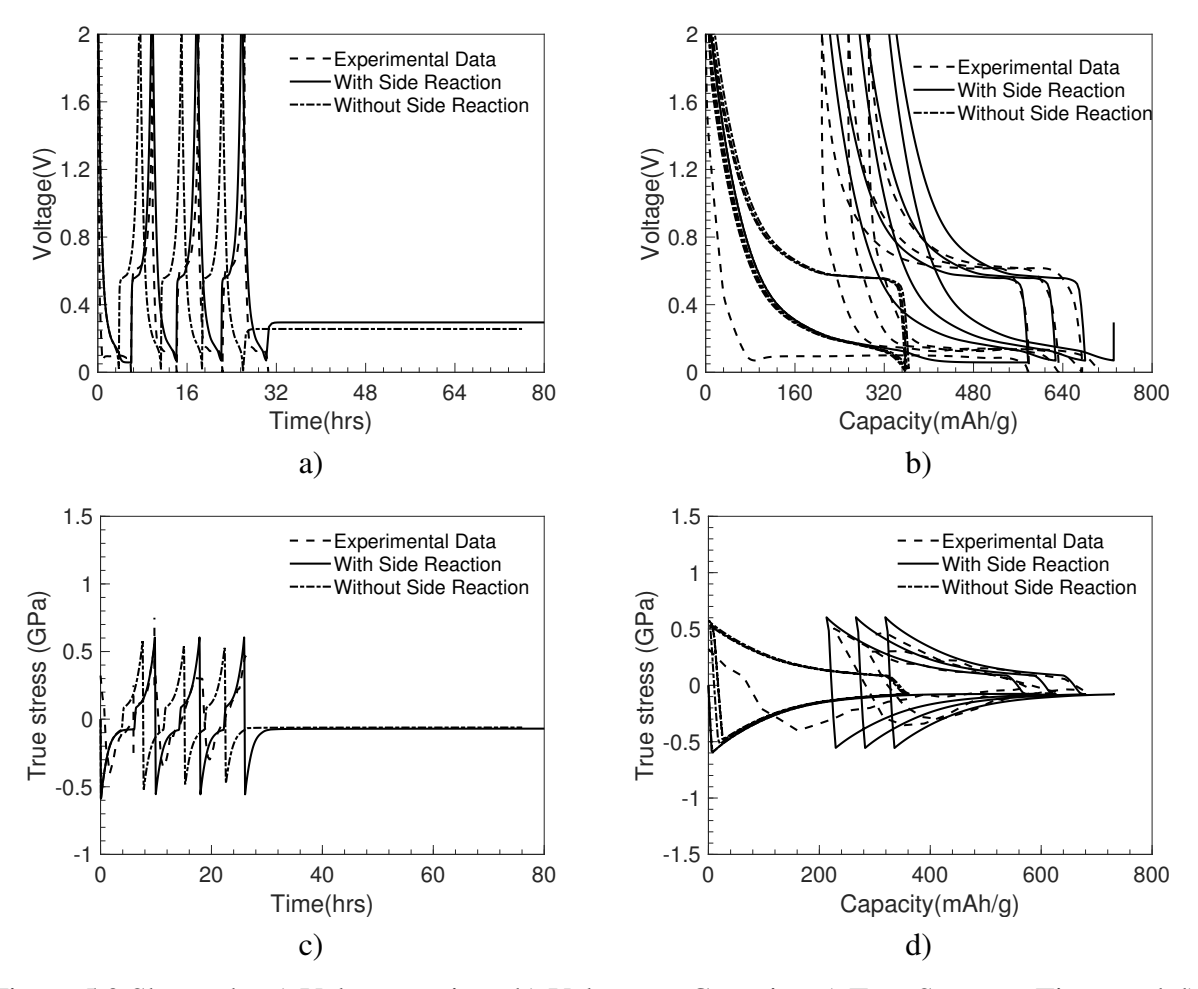


Figure 5.9 Shows the a) Voltage vs time, b) Voltage vs Capacity, c) True Stress vs Time, and d) True stess vs capacity for Li-Ge. Here the dotted black curve is the experimental data, solid black is the simulation with the side reaction and dash dotted curve shows the simulation without side reaction. The inclusion of side reaction allow to match the capacity, account for charge lost, and capture potential change during OCP.

5.5 Conclusion

High performance anodes are been considered for for batteries such lithium ion and sodium ion. These high performance anodes undergo large volume expansion i.e 300% which when constrained produces stress in the order of 1 GPa. These stress can also fracture the electrode and cause variour other associated effects. Therfore a mathematics model is needed in order to study the electrode behavior and design electrode gemometries.

Models that have been develoed in literature are all based on lithium ion batteries. The lithium ion batteries are effecient as compared to other batteries viz. sodium ion therfore, simple

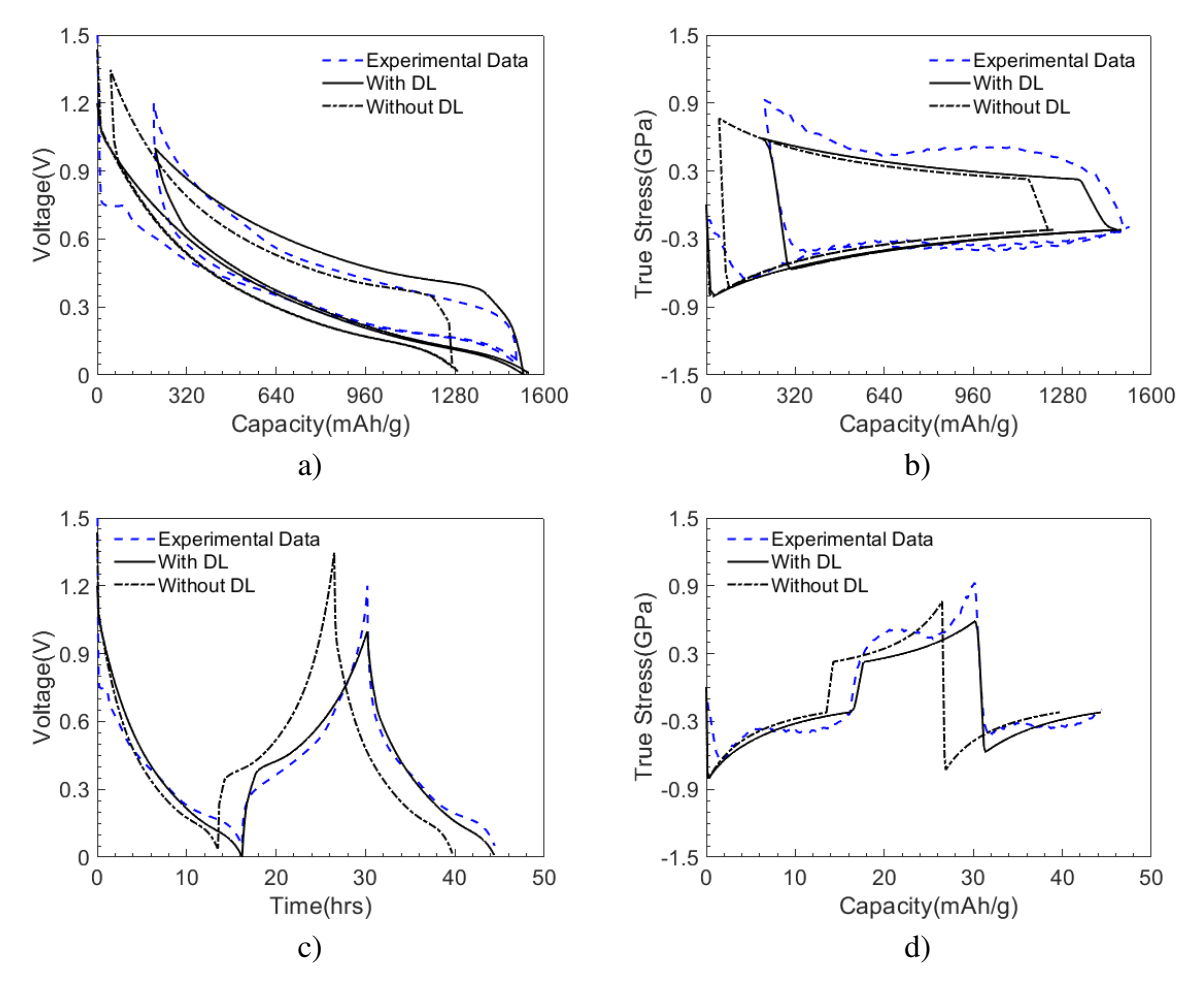


Figure 5.10 Shows the a) Voltage vs Capacity, b) Stess vs Capacity, c) Voltage vs Time, and d) stress vs time during OCP for Li-Ge. Here we compare the effect of double layer capacitance on potential and stress. The double layer capacitance allows to capture accurately the shape of potential and stress during galvanostatic flux change.

approximation of electrochemical effects can be used however, in order to apply these models for upcoming battery chemistries a model which include a generalized description is need. The models are also based on steady state electrochemical kinetics however a transient model is needed to include rate dependency.

Here a simplified transient electrochemical model is formulated coupled with a diffusion deformation model with include viscoplastic constitutive behavior. The model is numerically implemented in a ABAQUS UEL subroutine for three different element i.e. axisymmetric, plane strain and 3D. The model is verified for the viscoplastic finite element implementation and diffusion. There verification shows the formulated model is consistent with standard analytical equations.

The model is calibrated against experiments performed on two different system i.e. Li-Ge and Na-Ge. The calbration shows the robust nature of the model which can be used not only for existing lithium ion batteries but also for sodium ion batteries. The NIB shows a sinificant marching behavior as compared to LIB. In this case, the tafel kinetics side reaction implementation allow to capture the marching behavior. Also, the taflel kinetics allows to capture the potential change during no flux boundary condition i.e. Open Circut Potential (OCP) which is experimentally observed. The side reaction also allow to accurately relate the stress-potential during galvanostatic cycle.

The main and side reaction are the steady state kinetic however, to implement trainsient kinetics, a capacitance is included in the model. The capacitace acts as a buffer for the flux flow controlling rate for ion flux. The effect can be clearly seen in the potential and stress data where an accurate prediction of experimental data is observed compared to steady state condition especially when there is a change in flux direction or applied current. In addition during OCP condition the stress and potential is accuratly known. The difference is highly noticable when high current is applied. Therfore in order to predict stress and potential for higher performance anoded for various chemistries a coupled transient electrochemical model along with large deformation kinetmatics is necessary.

CHAPTER 6

CONCLUSION AND FUTURE PLAN

6.1 Conclusion

6.1.1 Interface fracture under dry conditions

An experimental methodology to characterize the failure behavior of binder/active material interfaces in battery electrodes is established using PVdF/Si as a model interface. A blister test sample that mimics the PVdF/Si interfaces in commercial batteries was fabricated using a series of nanofabrication processes. The samples were then assembled in a cell to pressurize the PVdF film until it delaminates from the Si surface. The pressure and deflection behavior of the film was measured during the experiment with an in-house optical setup based on Michelson interferometry principle.

The critical pressure measured at the onset of crack propagation was then used in a finite element model to evaluate the critical strain energy release rate G_c of the PVdF/Si interface. The FE model accurately accounted for all the experimental conditions including the initial profile of the PVdF film (which was not flat under zero applied pressure for PVdF/SiO₂ samples) and the residual stress in the film which was measured using a well-known substrate curvature measurement technique. The sample design and current testing method ensured small-scale yielding conditions in the samples, i.e., the sample was nominally elastic throughout the test, and the plastic deformation of the PVdF was confined to a very small region near the crack tip. As a result, the critical energy release rate values and the overall mechanical behavior evaluated from a simple analytical solution, based on the theory of linear elasticity, matched very well with those determined from the FE model, which accounted for large deformation and non-linear material behavior.

The average and standard deviation of the critical strain energy release rate Gc of PVdF/Si interface, measured from seven circular blister samples, is $0.59 \pm 0.16 \text{ J/m}^2$. The XPS and SEM analysis of the fracture surfaces showed that the crack path was predominantly at the PVdF/Si interface, i.e., pure delamination, and the mechanism of failure was adhesive. Hence, the measured

Gc can be considered as the energy required to break the bonds to separate PVdF from Sisurfaces. Since the crack propagation occurred at the interface, fracture is mixed-mode and the measured Gc, in general, is a function of the phase angle ψ . The phase angle in the axisymmetric (circular) samples used here is 68°, hence, the Gc = 0.59 ± 0.16 J/m² should be associated with this phase angle. It should be noted that the Gc values reported here were measured by accounting for the residual stress in the film, but if the residual stress in the film was not measured and ignored, the error in the Gc measurement will be 47%.

It is observed that PVdF adhere strongly to SiO_2 compared to Si with native oxide which was determined by the fact that Gc of SiO_2 samples is 2.46 ± 0.40 J/m² compared to Si with native oxide. The likely mechanism that contributes to the higher adhesion is high concentration of Silanol (Si-OH) group present on the substrate surface of SiO_2 compare to native oxide Si. The PVdF adheres to these Si-OH group via the van der waals forces. The higher concentration of Si-OH was verified using XPS and Raman characterization of both surfaces. This observation corroborates with the literature where PVdF modified with -OH or binders with higher -OH concentration bonds better with Si surface. The novel systematic method developed not only allow to quantify the measured of energy release rate i.e. intrinsic adhesion between polymer binder and active material but can also provide insight into the bonding mechanism.

Since the measured Gc is a fundamental fracture parameter that characterizes PVdF/Si and PVdF/SiO₂ interface failure, one can use $G = G_c$ as a failure criterion to predict interface failure irrespective of sample geometry, including the interfaces in a composite battery electrode. To validate and demonstrate the predictive capability of the fracture criterion $G = G_c$, rectangular (plane strain) samples with PVdF films on SiO₂ surface were tested and failure pressure was recorded. Using the measured G_c in a finite element analysis, the failure pressure of the rectangular samples was predicted successfully. The predictions agreed remarkably well, demonstrating that the critical energy release rate G_c measured is a fundamental fracture property that characterizes the PVdF/SiO₂ interface failure. This study paves the way for the implementation of fracture mechanics ideas in multiphysics battery models to simulate and predict the degradation behavior

of batteries

6.1.2 Interface fracture under electrochemical conditions

The PVdF/Si and PVdF/SiO₂ interface shows 0.59 ± 0.16 J/m² and 2.46 ± 0.40 J/m² energy release rate under atmospheric condition. However, in batteries various mechanism occur at the interface due to electrochemical cycling i.e. lithium transport in Si to form lithiated Si, SEI formation, and swelling of PVdF binder due to electrolyte. Therefore, it is important to understand the effect of electrochemical cycling on the interface adhesion i.e. energy release rate of PVdF/Si. Here we subject the PVdF/Si sample to electrochemical cycling by soaking the sample in electrolyte, adding a polymer separator and lithium metal foil over the sample. The samples and lithium foil was connected to an external potentiostat to supply current. Here PVdF/Si sample is the working electrode and lithium foil is the reference/counter electrode. The sample was subjected to a galvanostatic current of 7.5 μ A for 8 h and then tested for interface failure similar to the dry PVdF/Si and PVdF/SiO₂ samples.

The PVdF in the PVdF/Lithiated Si sample showed significant deflection compared to dry PvdF/Si sample. This was due to lower thickness of PVdF i.e. 1.2 μm compared to 6 μm. Also due to electrolyte swelling, the Youngs Modulus of PVdF reduced from 1.6 GPa to 0.3 GPa. FE analysis was performed and compared to the experimental data. It was observed that after certain pressure the experimental deflection was significantly higher that FE simulation. This was due to the crack initiation and propagation as the diameter of intact PVdF increased. Visual observation confirmed the crack initiation. The energy release rate at crack initiation was obtained to be 0.28 ± 0.04 J/m² which is nearly third of the dry condition PVdF/Si i.e. 0.5 9± 0.16 J/m². Therefore, due to electrochemical cycling the interface between PVdF/Si degrades.

This degradation of interface is likely to happen due to the swelling of PVdF binder which disrupts the van der waals interaction between PVdF and Si substrate. Also, the due to degradation of electrolyte, there is formation of SEI at the interface. To verify the interface failure between PVdF/Lithiated Si, formation of SEI and lithiation of Si, XPS analysis was performed on the failed sample. The XPS analysis shows minimal presence of PVdF related peak (686.6 eV) in Si

compound indicating the interface failure. LiPF6 salt derivatives compounds on Si surface indicated the formation of SEI and Li metal peak were observed in Si proving the lithiated Si formation. Therefore, the obtained Gc for PVdF/lithiated Si is the interface adhesion energy required to remove the PVdF binder from Si surface. The obtained energy can be implemented in a Multiphysics model to predict the failure of the composite electrode.

6.1.3 Multiphyiscs model for active material

A multiphysics model that can account for large deformation behavior of active material and strong coupling between mechanics and electrochemistry was developed. The existing models in literature capture the large deformation behavior of battery materials but assume steady state electrochemical kinetics. Here we implement the transient electrochemical kinetic which considers the effect of double layer that exists at the active material particle/electrolyte interface. This implementation allows the time dependent electrochemical behavior.

Here we implement a simple double layer capacitance model relating the current associated with double layer charging to the rate of change of potential; the proportionality constant will be the double layer capacitance. The electrochemical reaction associated with solid solution formation i.e. lithiation/deliathiation or sodiation/desodiation were implemented using Butler/Volmer kinetic and reaction associated with loss of active ions e.g. SEI formation were implemented using Taflel kinetics. The deformation behavior of active material particle was implemented using multiplicative decomposition of diffusion gradient in which the elastic deformation, plasticity and swelling due to volume expansion. The active material particle constitutive behavior was implemented as elastic deformation followed by rate dependent plasticity based on the experimental observation of Li-Ge and Na-Ge. The model is numerically implemented in ABAQUS user element subroutine (UEL).

The model is calibrated with the experiments performed on two deferent systems, i.e., Li-Ge and Na-Ge systems. The calibration shows the robust nature of the model which can be used not only for existing lithium ion batteries but also for sodium ion batteries. The effect of ignoring transient electrochemical kinetics was shown by performing simulations with and without the double layer capacitance. It was observed that the transient kinetics allows for smoother transition in potential

and stress which is what observed in experiments. Also, it enables accurate prediction of the stress and potential behavior of electrodes. Therefore, implementation of transient kinetics is important to accurately predict the behavior of active material particle. The theory will also allow us to predict the interface failure behavior at the binder/ active material interface by applying a cohesive behavior at the interface.

6.2 Future Work

The interface fracture experiments were preformed under dry condition and electrochemical condition for PVdF/Si and PVdF/SiO₂ interface. These characterization method can be extended to study

- 1. Effect of cabon black additive in PVdF on the interface fracture
- 2. Investigating Na-carboxylmethyl cellulose (CMC)/Si interface in dry and electrochemical conditions
- 3. Repeating this study for Na-ion battery composite electrodes
- 4. The current experimental setup uses noncoherent source of green light, but a whitelight with scanning capability can eliminate the limitation of the existing setup
- 5. The current setup can be extended to investigate the stress-strain behavior of electrodes

The model can be extended to

- 1. This model can be extended to include thermal behavior compsite electrode i.e. binder and active material
- 2. Extending the theory to include interface damage
- 3. Extending the theory to develop model for a composite electrode
- 4. Studying the fracture behavior of active material particle

In next two section we will explain with preliminary reults the experiments and model

6.2.1 Characterizing the Stress-Strain behavior of thin films

The experimental method to characterize the interface failure also provided the stress-strain behavior of the thin films. Here we demonstrate the capability by subjecting a PVdF thin film to a loading-unloading pressure-time relation. Fig. 6.1a show the rectangular plane strain sample subjected to an Ar pressure of 4.5 KPa and then unloaded to 1 KPa of pressure at a mass flow rate of 0.8 sccm. The obtained pressure-time curve is shown in Fig. 6.1b. The plateaus obtained in Fig. 6.1a after 4 KPa is due to leakage. Fig. 6.1b shows the corresponding pressure-central deflection obtained from the interference pattern using the procedure described in chapter 2.

The experimentally obtained pressure-central deflection can be converted to stress and strain be implementing the equations Xiang et al. [69]

$$\sigma = \frac{p(a^2 + w_0^2)}{2w_0 t_f} \tag{6.1}$$

and

$$\epsilon = \epsilon_o + \frac{a^2 + w_0^2}{2aw_0} \arcsin\left(\frac{2aw_0}{a^2 + w_0^2}\right) - 1. \tag{6.2}$$

Here σ is the stress and ϵ is the strain in the film. This is obtained for the PVdF film and is shown in Fig. 6.1d. Here the a linear fit is performed on the unloading section of stress-strain curve, and the slope of the linear fit can provide the Youngs modulus of the PVdF film. The elastic modulus was obtained to be 2.95 GPa which is similar to the modulus repoted in literature [27].

A similar analysis can be performed on Si thin film and which can be subjected to lithiation/delithiation and and obtain the stress-strain curve of lithiated films at various concentrations.

6.2.2 Finite Element Simulation of interface failure in composite electrode

Figure 6.2 show the schematic of the rechargeable battery electrode with a zoomed in view at an active material particle and binder interface. The inset is the FE mesh where the 100 nm Si active material particle is discretized with ABAQUS UEL element and PVdF binder is discretized with CAX4 element. The objective of the simulation is to understand the behavior of Si active material particle in the presence of PVdF binder and predict the interface failure behavior.

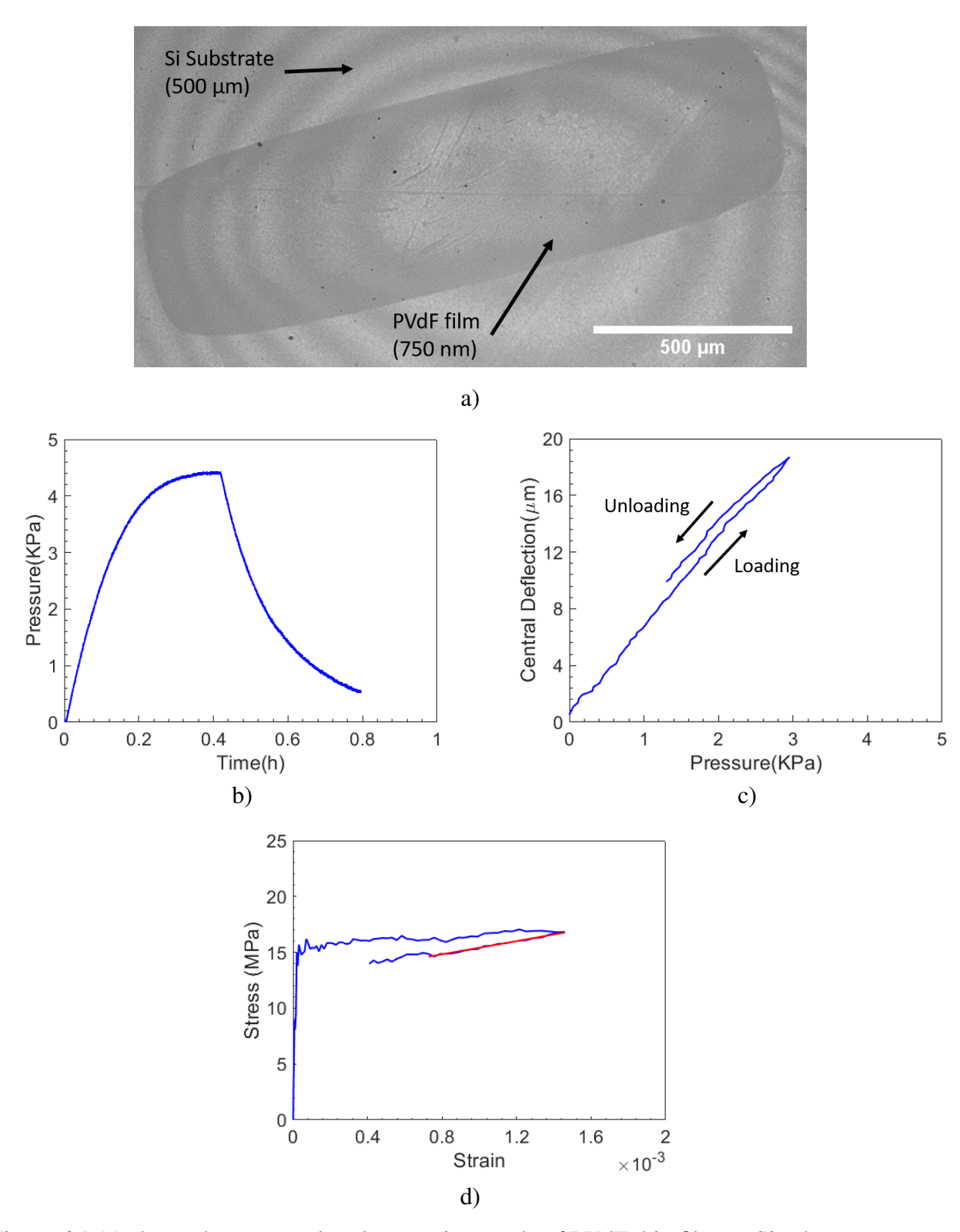


Figure 6.1 (a) shows the rectangular plane strain sample of PVdF thin film on Si substrate (b)Shows the Pressure-time curve of a rectangular PVdF thin film (750 nm) (c) show the corresponding pressure-central deflection during the loading and unloading (d) show the stress and plane strain in the central deflection region where the red line is a linear fit to the stress-strain during unloading.

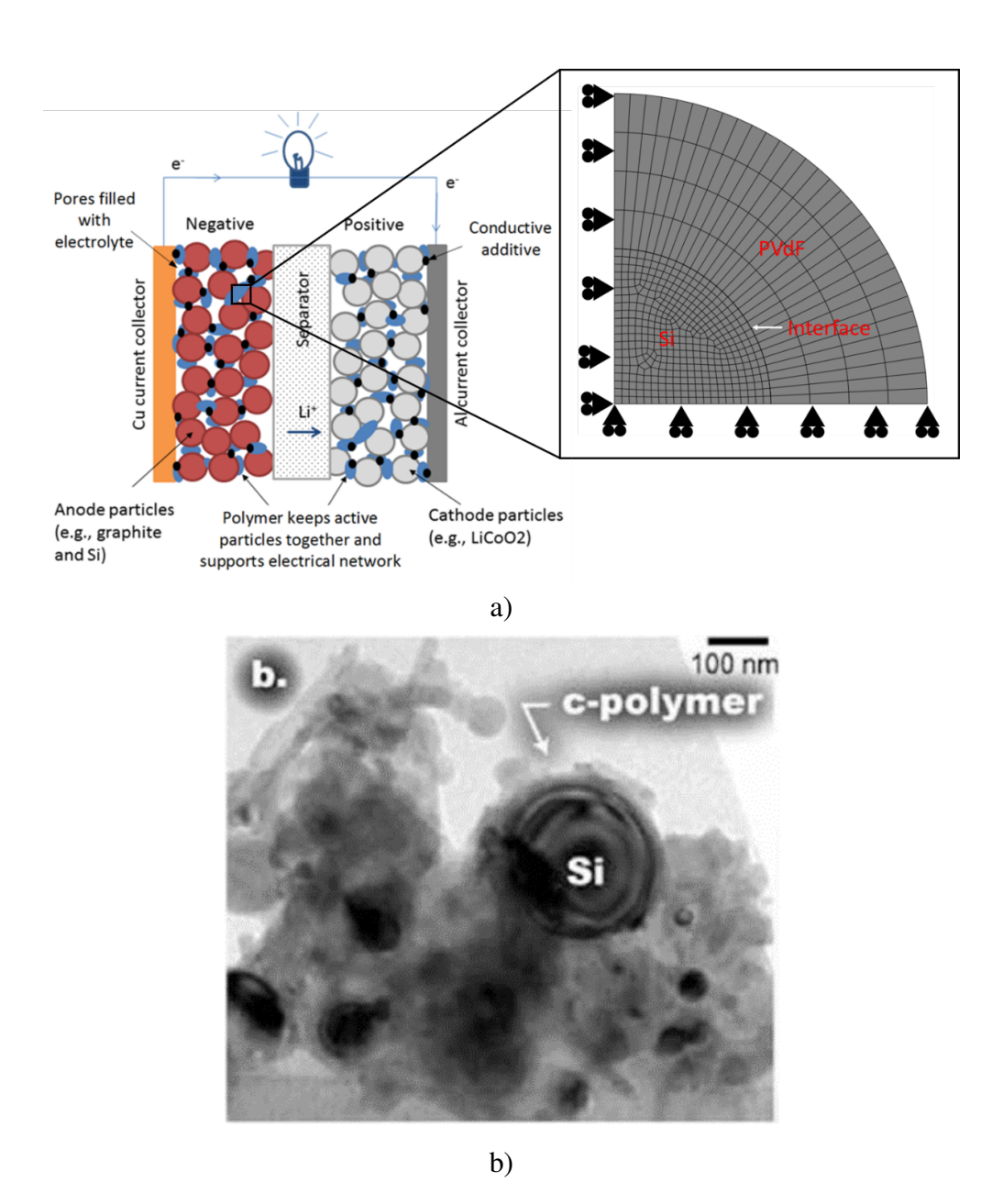


Figure 6.2 (a)Shows the schematic of rechargeable battery with composite electrode. The inset shows the zoomed in view of a binder attached to Si particle. The inset is a FE mesh representing the quarter of the particle with symmetry boundary conditions.(b)Actual active material particle with binder[5].

In this simulation the constitutive behavior of Si particle is defined by the diffusion-deformation theory as defined in Chapter 5. Similarly, the PVdF is defined by elastic-visoplastic constitutive behavior as given by Santimetaneedol et al. [27] and is implemented as an ABAQUS user defined material (UMAT). Here the interface is defined by cohesive surface behavior defined by the quadratic maximum traction-separation relation as

$$\frac{\langle t_n \rangle}{t_n^0} + \frac{t_s}{t_s^0} + \frac{t_f}{t_t^0} = 1 \tag{6.3}$$

Here t_n^0 , t_s^0 , and t_t^0 is peak contact stress at the interface. Here the subscript represent n is normal direction, s and t are the first shear and second shear directions. In a 2-D simplification we can assume the first and second shear direction to be similar as shown in Fig ??. The area under the traction-separation curve is the Gc obtained experimentally from the interface fracture tests.

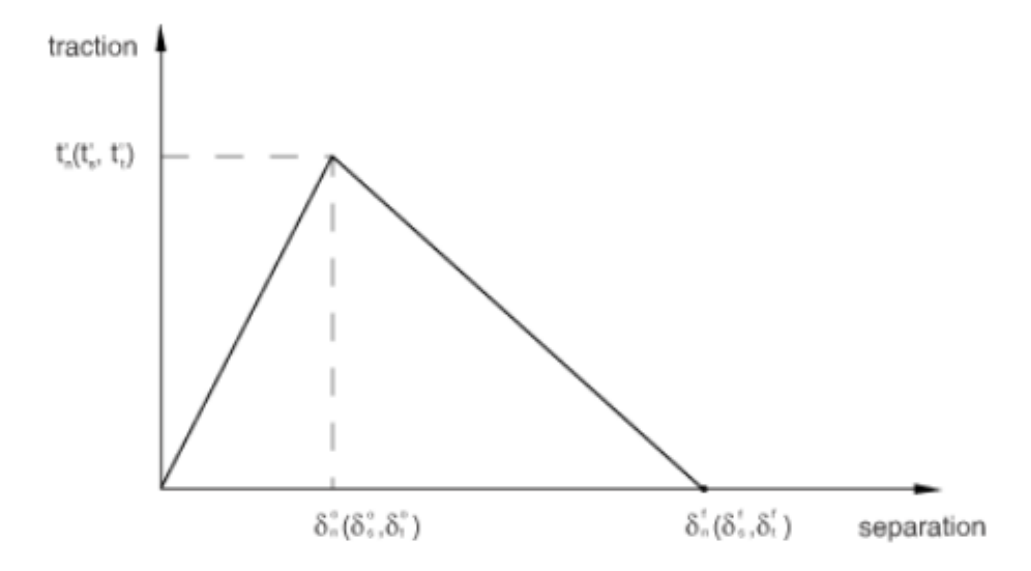


Figure 6.3 Typical traction separation relation with linear softening.

The lithiation/delithiation flux is applied at the interface between the PVdF binder and Si surface because PVdF binder absorbs the electrolyte and provide ions for diffusion. Fig. ??a shows the Potential-time curve obtained for the single particle due to galvanostatic current applied. Here the Si active material particle expands however, it is constrained by the PVdF binder on the surface. Therefore, the expansion causes large traction at the interface between binder and active material

particle. It was observed here due to expansion the interface starts to damage. Fig ??b shows the damage initiated quite quickly (at (i)) however, there is no detachment seen at the interface due to volume expansion generating compressive stress at the interface. The damage progresses until the complete lithiation. Here the particle behaves similar to a perfectly bonded particle until end of lithiation i.e. pt (ii).

When delithiation progresses, the particle interacts with binder on the edges where the contact remains and imparts tensile hoop stress on binder. At pt. (iii) we can see the complete damage progression and detachment of active material particle from the polymer binder indicating failure.

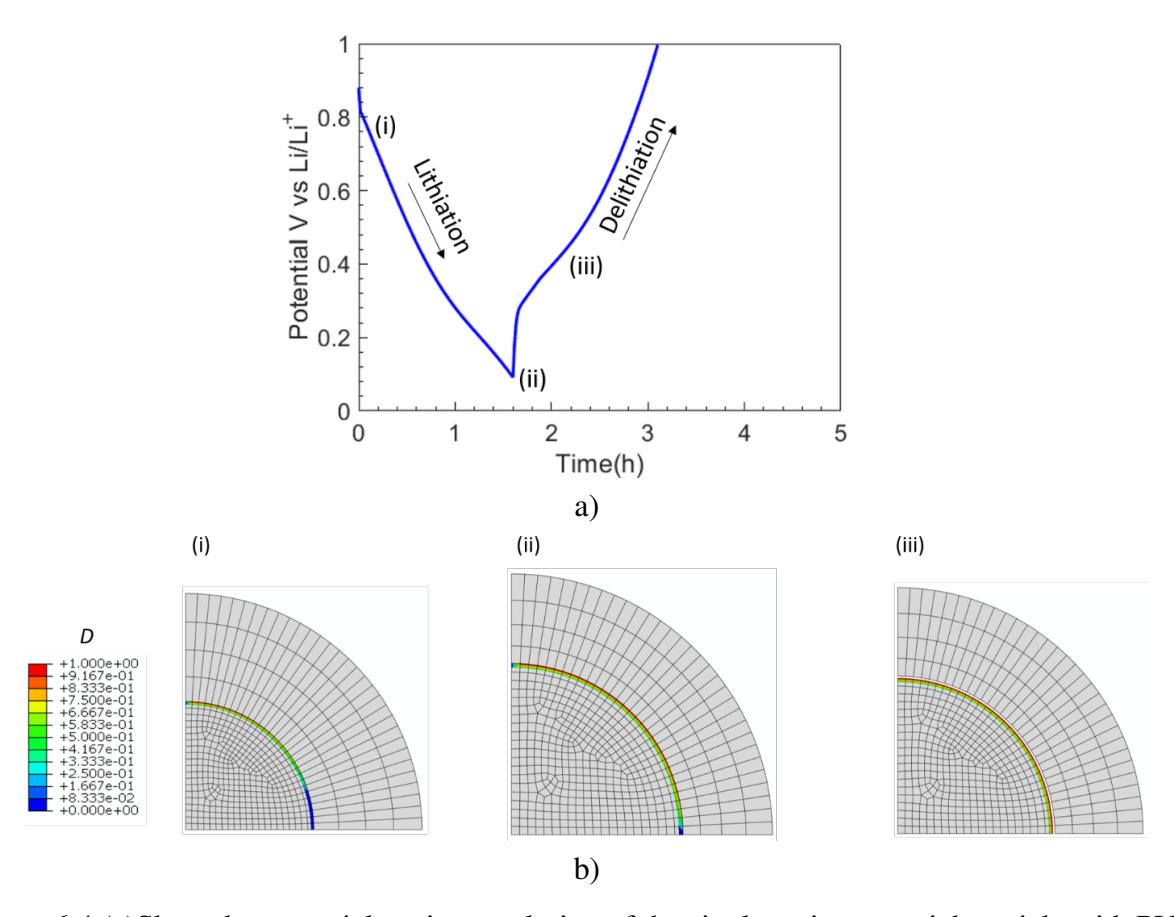


Figure 6.4 (a)Show the potential vs time evolution of the single active material particle with PVdF binder Fig.7.1 subjected to galvanostatic lithiation and delithiation (b) Show the corresponding damage evolution (D) at three different points on the potential-time curve.

BIBLIOGRAPHY

- [1] B. D. McCloskey, "Expanding the Ragone Plot: Pushing the Limits of Energy Storage," Sept. 2015.
- [2] T. Yoon, C. C. Nguyen, D. M. Seo, and B. L. Lucht, "Capacity Fading Mechanisms of Silicon Nanoparticle Negative Electrodes for Lithium Ion Batteries," *Journal of The Electrochemical Society*, vol. 162, no. 12, pp. A2325–A2330, 2015.
- [3] M. B. Pinson and M. Z. Bazant, "Theory of SEI Formation in Rechargeable Batteries: Capacity Fade, Accelerated Aging and Lifetime Prediction," *Journal of The Electrochemical Society*, vol. 160, no. 2, pp. A243–A250, 2013.
- [4] S. P. V. Nadimpalli, V. A. Sethuraman, G. Bucci, V. Srinivasan, A. F. Bower, and P. R. Guduru, "On Plastic Deformation and Fracture in Si Films during Electrochemical Lithiation/Delithiation Cycling," *Journal of The Electrochemical Society*, vol. 160, no. 10, pp. A1885–A1893, 2013.
- [5] H. Wang, S. P. Nadimpalli, and V. B. Shenoy, "Inelastic shape changes of silicon particles and stress evolution at binder/particle interface in a composite electrode during lithiation/delithiation cycling," *Extreme Mechanics Letters*, vol. 9, pp. 430–438, Dec. 2016.
- [6] M. M. Thackeray, C. Wolverton, and E. D. Isaacs, "Electrical energy storage for transportation Approaching the limits of, and going beyond, lithium-ion batteries," June 2012.
- [7] U. Kasavajjula, C. Wang, and A. J. Appleby, "Nano- and bulk-silicon-based insertion anodes for lithium-ion secondary cells," *Journal of Power Sources*, vol. 163, pp. 1003–1039, Jan. 2007.
- [8] Z. Chen, L. Christensen, and J. R. Dahn, "Comparison of PVDF and PVDF-TFE-P as Binders for Electrode Materials Showing Large Volume Changes in Lithium-Ion Batteries," *Journal of The Electrochemical Society*, vol. 150, no. 8, p. A1073, 2003.
- [9] J. H. Ryu, J. W. Kim, Y.-E. Sung, and S. M. Oh, "Failure Modes of Silicon Powder Negative Electrode in Lithium Secondary Batteries," *Electrochemical and Solid-State Letters*, vol. 7, no. 10, p. A306, 2004.
- [10] E. Peled, "The Electrochemical Behavior of Alkali and Alkaline Earth Metals in Nonaqueous Battery Systems—The Solid Electrolyte Interphase Model," *Journal of The Electrochemical Society*, vol. 126, no. 12, pp. 2047–2051, 1979.
- [11] C. Hendricks, N. Williard, S. Mathew, and M. Pecht, "A failure modes, mechanisms, and effects analysis (FMMEA) of lithium-ion batteries," *Journal of Power Sources*, vol. 297, pp. 113–120, Nov. 2015.
- [12] M. N. Obrovac and L. Christensen, "Structural changes in silicon anodes during lithium insertion/extraction," *Electrochemical and Solid-State Letters*, vol. 7, no. 5, pp. 93–96, 2004.

- [13] V. A. Sethuraman, M. J. Chon, M. Shimshak, V. Srinivasan, and P. R. Guduru, "In situ measurements of stress evolution in silicon thin films during electrochemical lithiation and delithiation," *Journal of Power Sources*, vol. 195, pp. 5062–5066, Aug. 2010.
- [14] A. Mukhopadhyay, R. Kali, S. Badjate, A. Tokranov, and B. W. Sheldon, "Plastic deformation associated with phase transformations during lithiation/delithiation of Sn," *Scripta Materialia*, vol. 92, pp. 47–50, 2014.
- [15] S. P. V. Nadimpalli, R. Tripuraneni, and V. A. Sethuraman, "Real-Time Stress Measurements in Germanium Thin Film Electrodes during Electrochemical Lithiation/Delithiation Cycling," *Journal of The Electrochemical Society*, vol. 162, no. 14, pp. A2840–A2846, 2015.
- [16] M. Pharr, Y. S. Choi, D. Lee, K. H. Oh, and J. J. Vlassak, "Measurements of stress and fracture in germanium electrodes of lithium-ion batteries during electrochemical lithiation and delithiation," *Journal of Power Sources*, vol. 304, pp. 164–169, 2016.
- [17] M. Pharr, Z. Suo, and J. J. Vlassak, "Measurements of the fracture energy of lithiated silicon electrodes of Li-Ion batteries," *Nano Letters*, vol. 13, no. 11, pp. 5570–5577, 2013.
- [18] L. Chen, X. Xie, J. Xie, K. Wang, and J. Yang, "Binder effect on cycling performance of silicon/carbon composite anodes for lithium ion batteries," *Journal of Applied Electrochemistry*, vol. 36, pp. 1099–1104, Oct. 2006.
- [19] L. Fransson, T. Eriksson, K. Edström, T. Gustafsson, and J. O. Thomas, "Influence of carbon black and binder on Li-ion batteries," *Journal of Power Sources*, vol. 101, pp. 1–9, Oct. 2001.
- [20] C. Li, H. Zhang, L. Fu, H. Liu, Y. Wu, E. Rahm, R. Holze, and H. Wu, "Cathode materials modified by surface coating for lithium ion batteries," *Electrochimica Acta*, vol. 51, pp. 3872–3883, May 2006.
- [21] D. Mazouzi, B. Lestriez, L. Roué, and D. Guyomard, "Silicon composite electrode with high capacity and long cycle life," *Electrochemical and Solid-State Letters*, vol. 12, p. A215, Aug. 2009.
- [22] D. Mazouzi, Z. Karkar, C. R. Hernandez, P. J. Manero, D. Guyomard, L. Roué, B. Lestriez, C. Reale Hernandez, P. Jimenez Manero, D. Guyomard, L. Roué, and B. Lestriez, "Critical roles of binders and formulation at multiscales of silicon-based composite electrodes," *Journal of Power Sources*, vol. 280, pp. 533–549, Apr. 2015.
- [23] M. N. Obrovac and L. J. Krause, "Reversible Cycling of Crystalline Silicon Powder," *Journal of The Electrochemical Society*, vol. 154, p. A103, Dec. 2007.
- [24] J. Chen, J. Liu, X. Li, Y. Qi, and T. Sun, "Unveiling the Roles of Binder in the Mechanical Integrity of Electrodes for Lithium-Ion Batteries," *Journal of The Electrochemical Society*, vol. 160, no. 9, pp. A1502–A1509, 2013.

- [25] S. P. Nadimpalli, V. A. Sethuraman, D. P. Abraham, A. F. Bower, and P. R. Guduru, "Stress Evolution in Lithium-Ion Composite Electrodes during Electrochemical Cycling and Resulting Internal Pressures on the Cell Casing," *Journal of The Electrochemical Society*, vol. 162, pp. A2656–A2663, Oct. 2015.
- [26] E. K. Rahani and V. B. Shenoy, "Role of Plastic Deformation of Binder on Stress Evolution during Charging and Discharging in Lithium-Ion Battery Negative Electrodes," *Journal of The Electrochemical Society*, vol. 160, pp. A1153–A1162, May 2013.
- [27] A. Santimetaneedol, R. Tripuraneni, S. A. Chester, and S. P. Nadimpalli, "Time-dependent deformation behavior of polyvinylidene fluoride binder: Implications on the mechanics of composite electrodes," *Journal of Power Sources*, vol. 332, pp. 118–128, Nov. 2016.
- [28] V. A. Sethuraman, A. Nguyen, M. J. Chon, S. P. V. Nadimpalli, H. Wang, D. P. Abraham, A. F. Bower, V. B. Shenoy, and P. R. Guduru, "Stress Evolution in Composite Silicon Electrodes during Lithiation/Delithiation," *Journal of The Electrochemical Society*, vol. 160, pp. A739–A746, Mar. 2013.
- [29] K. Kierzek, "Influence of Binder Adhesion Ability on the Performance of Silicon/Carbon Composite as Li-Ion Battery Anode," *Journal of Materials Engineering and Performance*, vol. 25, pp. 2326–2330, June 2016.
- [30] M. Wu, X. Xiao, N. Vukmirovic, S. Xun, P. K. Das, X. Song, P. Olalde-Velasco, D. Wang, A. Z. Weber, L. W. Wang, V. S. Battaglia, W. Yang, and G. Liu, "Toward an ideal polymer binder design for high-capacity battery anodes," *Journal of the American Chemical Society*, vol. 135, pp. 12048–12056, Aug. 2013.
- [31] M. Yoo, C. W. Frank, and S. Mori, "Interaction of poly(vinylidene fluoride) with graphite particles. 1. Surface morphology of a composite film and its relation to processing parameters," *Chemistry of Materials*, vol. 15, pp. 850–861, Feb. 2003.
- [32] Y.-S. Hu, R. Demir-Cakan, M.-M. Titirici, J.-O. Müller, R. Schlögl, M. Antonietti, and J. Maier, "Superior Storage Performance of a Si@SiOx/C Nanocomposite as Anode Material for Lithium-Ion Batteries," *Angewandte Chemie International Edition*, vol. 47, no. 9, pp. 1645–1649, 2008.
- [33] S. Komaba, K. Shimomura, N. Yabuuchi, T. Ozeki, H. Yui, and K. Konno, "Study on polymer binders for high-capacity SiO negative electrode of Li-Ion batteries," *Journal of Physical Chemistry C*, vol. 115, pp. 13487–13495, July 2011.
- [34] J. H. Lee, U. Paik, V. A. Hackley, and Y. M. Choi, "Effect of poly(acrylic acid) on adhesion strength and electrochemical performance of natural graphite negative electrode for lithium-ion batteries," *Journal of Power Sources*, vol. 161, pp. 612–616, Oct. 2006.
- [35] S. Sun, D. He, P. Li, Y. Liu, Q. Wan, Q. Tan, Z. Liu, F. An, G. Gong, and X. Qu, "Improved adhesion of cross-linked binder and SiO2-coating enhances structural and cyclic stability of silicon electrodes for lithium-ion batteries," *Journal of Power Sources*, vol. 454, p. 227907, Apr. 2020.

- [36] S. Müller, V. Wood, P. Baade, B.-E. Brandt, F. De Carlo, P. Pietsch, V. De Andrade, B.-E. Brandt, P. Baade, V. De Andrade, F. De Carlo, and V. Wood, "Quantification and modeling of mechanical degradation in lithium-ion batteries based on nanoscale imaging," *Nature Communications*, vol. 9, p. 2340, Dec. 2018.
- [37] A. Al-Obeidi, D. Kramer, C. V. Thompson, and R. Mönig, "Mechanical stresses and morphology evolution in germanium thin film electrodes during lithiation and delithiation," *Journal of Power Sources*, vol. 297, pp. 472–480, 2015.
- [38] M. Pharr, Z. Suo, and J. J. Vlassak, "Variation of stress with charging rate due to strain-rate sensitivity of silicon electrodes of Li-ion batteries," *Journal of Power Sources*, vol. 270, pp. 569–575, Dec. 2014.
- [39] S. Rakshit, A. S. Pakhare, O. Ruiz, M. R. Khoshi, E. Detsi, H. He, V. A. Sethuraman, and S. P. V. Nadimpalli, "Measurement of Volume Changes and Associated Stresses in Ge Electrodes Due to Na/Na+ Redox Reactions," *Journal of The Electrochemical Society*, vol. 168, p. 010504, Jan. 2021.
- [40] Z. Chen, L. Christensen, and J. Dahn, "Large-volume-change electrodes for Li-ion batteries of amorphous alloy particles held by elastomeric tethers," *Electrochemistry Communications*, vol. 5, pp. 919–923, Nov. 2003.
- [41] G. Singh and T. K. Bhandakkar, "Analytical Investigation of Binder's Role on the Diffusion Induced Stresses in Lithium Ion Battery through a Representative System of Spherical Isolated Electrode Particle Enclosed by Binder," *Journal of The Electrochemical Society*, vol. 164, pp. A608–A621, Jan. 2017.
- [42] V. A. Sethuraman, V. Srinivasan, A. F. Bower, and P. R. Guduru, "In Situ Measurements of Stress-Potential Coupling in Lithiated Silicon," *Journal of The Electrochemical Society*, vol. 157, no. 11, p. A1253, 2010.
- [43] R. Tripuraneni, S. Rakshit, and S. P. V. Nadimpalli, "In Situ Measurement of the Effect of Stress on the Chemical Diffusion Coefficient of Li in High-Energy-Density Electrodes," *Journal of The Electrochemical Society*, vol. 165, pp. A2194–A2202, July 2018.
- [44] J. Christensen and J. Newman, "A Mathematical Model of Stress Generation and Fracture in Lithium Manganese Oxide," *Journal of The Electrochemical Society*, vol. 153, no. 6, p. A1019, 2006.
- [45] J. Christensen and J. Newman, "Stress generation and fracture in lithium insertion materials," *Journal of Solid State Electrochemistry*, vol. 10, pp. 293–319, Mar. 2006.
- [46] R. E. García, Y.-M. Chiang, W. Craig Carter, P. Limthongkul, and C. M. Bishop, "Microstructural Modeling and Design of Rechargeable Lithium-Ion Batteries," *Journal of The Electrochemical Society*, vol. 152, no. 1, p. A255, 2005.
- [47] Y. T. Cheng and M. W. Verbrugge, "Evolution of stress within a spherical insertion electrode particle under potentiostatic and galvanostatic operation," *Journal of Power Sources*, vol. 190, pp. 453–460, May 2009.

- [48] Y.-T. Cheng and M. W. Verbrugge, "Diffusion-Induced Stress, Interfacial Charge Transfer, and Criteria for Avoiding Crack Initiation of Electrode Particles," *Journal of The Electrochemical Society*, vol. 157, no. 4, p. A508, 2010.
- [49] R. Deshpande, Y. T. Cheng, and M. W. Verbrugge, "Modeling diffusion-induced stress in nanowire electrode structures," *Journal of Power Sources*, vol. 195, pp. 5081–5088, Aug. 2010.
- [50] T. K. Bhandakkar and H. Gao, "Cohesive modeling of crack nucleation under diffusion induced stresses in a thin strip: Implications on the critical size for flaw tolerant battery electrodes," *International Journal of Solids and Structures*, vol. 47, pp. 1424–1434, May 2010.
- [51] S. Golmon, K. Maute, and M. L. Dunn, "Numerical modeling of electrochemical-mechanical interactions in lithium polymer batteries," *Computers and Structures*, vol. 87, pp. 1567–1579, Dec. 2009.
- [52] S. Golmon, K. Maute, and M. L. Dunn, "Multiscale design optimization of lithium ion batteries using adjoint sensitivity analysis," *International Journal for Numerical Methods in Engineering*, vol. 92, no. 5, pp. 475–494, 2012.
- [53] S. Lee, A. M. Sastry, and J. Park, "Study on microstructures of electrodes in lithium-ion batteries using variational multi-scale enrichment," *Journal of Power Sources*, vol. 315, pp. 96–110, May 2016.
- [54] Y. Qi and S. J. Harris, "In Situ Observation of Strains during Lithiation of a Graphite Electrode," *Journal of The Electrochemical Society*, vol. 157, p. A741, May 2010.
- [55] Y. Qi, H. Guo, L. G. Hector, and A. Timmons, "Threefold Increase in the Young's Modulus of Graphite Negative Electrode during Lithium Intercalation," *Journal of The Electrochemical Society*, vol. 157, p. A558, Mar. 2010.
- [56] K. Zhao, M. Pharr, J. J. Vlassak, and Z. Suo, "Inelastic hosts as electrodes for high-capacity lithium-ion batteries," *Journal of Applied Physics*, vol. 109, p. 016110, Jan. 2011.
- [57] K. Zhao, M. Pharr, S. Cai, J. J. Vlassak, and Z. Suo, "Large plastic deformation in high-capacity lithium-ion batteries caused by charge and discharge," *Journal of the American Ceramic Society*, vol. 94, no. SUPPL. 1, pp. s226–s235, 2011.
- [58] A. Bower, P. Guduru, and V. Sethuraman, "A finite strain model of stress, diffusion, plastic flow, and electrochemical reactions in a lithium-ion half-cell," *Journal of the Mechanics and Physics of Solids*, vol. 59, pp. 804–828, Apr. 2011.
- [59] A. F. Bower and P. R. Guduru, "A simple finite element model of diffusion, finite deformation, plasticity and fracture in lithium ion insertion electrode materials," *Modelling and Simulation in Materials Science and Engineering*, vol. 20, no. 4, 2012.
- [60] A. F. Bower, E. Chason, P. R. Guduru, and B. W. Sheldon, "A continuum model of deformation, transport and irreversible changes in atomic structure in amorphous lithium-silicon electrodes," *Acta Materialia*, vol. 98, pp. 229–241, Oct. 2015.

- [61] G. Bucci, S. P. Nadimpalli, V. A. Sethuraman, A. F. Bower, and P. R. Guduru, "Measurement and modeling of the mechanical and electrochemical response of amorphous Si thin film electrodes during cyclic lithiation," *Journal of the Mechanics and Physics of Solids*, vol. 62, pp. 276–294, Jan. 2014.
- [62] L. Anand, N. M. Ames, V. Srivastava, and S. A. Chester, "A thermo-mechanically coupled theory for large deformations of amorphous polymers. Part I: Formulation," *International Journal of Plasticity*, vol. 25, pp. 1474–1494, Aug. 2009.
- [63] C. V. Di Leo, E. Rejovitzky, and L. Anand, "Diffusion–deformation theory for amorphous silicon anodes: The role of plastic deformation on electrochemical performance," *International Journal of Solids and Structures*, vol. 67–68, pp. 283–296, Aug. 2015.
- [64] A. J. Bard and L. R. Faulkner, *Electrochemical Methods: Fundamentals and Applications*. New York: Wiley, 2nd ed ed., 2001.
- [65] I. J. Ong and J. Newman, "Double-Layer Capacitance in a Dual Lithium Ion Insertion Cell," *Journal of The Electrochemical Society*, vol. 146, pp. 4360–4365, Dec. 1999.
- [66] V. A. Sethuraman, V. Srinivasan, and J. Newman, "Analysis of Electrochemical Lithiation and Delithiation Kinetics in Silicon," *Journal of The Electrochemical Society*, vol. 160, no. 2, pp. A394–A403, 2013.
- [67] Z. Cao, P. Wang, W. Gao, L. Tao, J. Suk, R. Ruoff, D. Akinwande, R. Huang, and K. Liechti, "A blister test for interfacial adhesion of large-scale transferred graphene," *Carbon*, vol. 69, pp. 390–400, Apr. 2014.
- [68] R. J. Hohlfelder, H. Luo, J. J. Vlassak, C. E. D. Chidsey, and W. D. Nix, "Measuring Interfacial Fracture Toughness With The Blister Test," *MRS Proceedings*, vol. 436, p. 115, Feb. 1996.
- [69] Y. Xiang, X. Chen, and J. Vlassak, "Plane-strain Bulge Test for Thin Films," *Journal of Materials Research*, vol. 20, pp. 2360–2370, Sept. 2005.
- [70] Simulia, "Abaqus / CAE 6.14 User's Manual," 2020.
- [71] T. Anderson, *Fracture Mechanics: Fundamentals and Applications*. CRC Press, 3 ed., Mar. 2017.
- [72] L. B. Freund and S. Suresh, *Thin Film Materials*. Cambridge University Press, Jan. 2004.
- [73] I. S. Raju, "Simple Formulas for Strain Energy Release Rates with Higher Order and Singular Finite Elements CALCULATION OF STRAIN-ENERGY RELEASE RATES WITH HIGHER ORDER AND SINGULAR FINITE ELEMENTS," *Engineering Fracture Mechanics*, vol. 28, pp. 251–274, 1987.
- [74] W. D. Nix and W. D. Nix, "Mechanical Properties of Thin Films," tech. rep., 2005.

- [75] M. K. Small and W. D. Nix, "Analysis of the accuracy of the bulge test in determining the mechanical properties of thin films," *Journal of Materials Research*, vol. 7, no. 6, pp. 1553–1563, 1992.
- [76] M. K. Small, B. J. Daniels, B. M. Clemens, and W. D. Nix, "The elastic biaxial modulus of Ag-Pd multilayered thin films measured using the bulge test," *Journal of Materials Research*, vol. 9, no. 1, pp. 25–30, 1994.
- [77] V. A. Sethuraman, "Capacity Fade due to Side-reactions in Silicon Anodes in Lithium-ion Batteries," *Portugaliae Electrochimica Acta*, pp. 1–14, Jan. 2012.
- [78] S. Guo, K. T. Wan, and D. A. Dillard, "A bending-to-stretching analysis of the blister test in the presence of tensile residual stress," *International Journal of Solids and Structures*, vol. 42, pp. 2771–2784, May 2005.
- [79] R. Leach, ed., *Optical Measurement of Surface Topography*. Berlin, Heidelberg: Springer, 2011.
- [80] H. M. Jensen and M. D. Thouless, "Effects of residual stresses in the blister test," *International Journal of Solids and Structures*, vol. 30, no. 6, pp. 779–795, 1993.
- [81] M. K. Small, J. J. Vlassak, and W. D. Nix, "Re-Examining the Bulge Test: Methods for Improving Accuracy and Reliability," *MRS Proceedings*, vol. 239, 1991.
- [82] K. M. Liechti and Y. S. Chai, "Asymmetric shielding in interfacial fracture under in-plane shear," *Journal of Applied Mechanics, Transactions ASME*, vol. 59, no. 2, pp. 295–304, 1992.
- [83] C. Wu, S. Gowrishankar, R. Huang, K. M. Liechti, C. Wu, R. Huang, K. M. Liechti, and S. Gowrishankar, "On determining mixed-mode traction-separation relations for interfaces A damage-based cohe," vol. 202, pp. 1–19, 2016.
- [84] J. G. Swadener, K. M. Liechti, and A. L. Lozanne, "The intrinsic toughness and adhesion mechanisms of a glass/epoxy interface," *Journal of the Mechanics and Physics of Solids*, vol. 47, pp. 223–258, Feb. 1999.
- [85] M. Morita, T. Ohmi, E. Hasegawa, M. Kawakami, and M. Ohwada, "Growth of native oxide on a silicon surface," *Journal of Applied Physics*, vol. 68, pp. 1272–1281, June 1990.
- [86] A. Vittadini, A. Selloni, and M. Casarin, "Binding and diffusion of hydroxyl radicals on Si(100): A first-principles study," *Physical Review B*, vol. 52, pp. 5885–5889, Aug. 1995.
- [87] M. Ghanem, M. Göken, and B. Merle, "Plane-strain bulge testing of thin films under compressive residual stresses," *Surface and Coatings Technology*, vol. 327, pp. 167–173, Oct. 2017.
- [88] V. Ziebart, O. Paul, and H. Baltes, "Strongly buckled square micromachined membranes," *Journal of Microelectromechanical Systems*, vol. 8, pp. 423–432, Dec. 1999.

- [89] Z. Cao, L. Tao, D. Akinwande, R. Huang, and K. M. Liechti, "Mixed-mode traction-separation relations between graphene and copper by blister tests," *International Journal of Solids and Structures*, vol. 84, pp. 147–159, May 2016.
- [90] G. Stoney, "The tension of metallic films deposited by electrolysis," *Proceedings of the Royal Society of London. Series A, Containing Papers of a Mathematical and Physical Character*, vol. 82, pp. 172–175, May 1909.
- [91] M. F. Kanninen and C. H. Popelar, *Advanced Fracture Mechanics (Oxford Engineering Science Series)*. 1985.
- [92] A. Agrawal and c. A. M. Karlsson, "Obtaining mode mixity for a bimaterial interface crack using the virtual crack closure technique," *Int J Fract*, vol. 141, pp. 75–98, 2006.
- [93] J. Hu, Y. Wang, D. Li, and Y. T. Cheng, "Effects of adhesion and cohesion on the electrochemical performance and durability of silicon composite electrodes," *Journal of Power Sources*, vol. 397, pp. 223–230, Sept. 2018.
- [94] A. Magasinski, B. Zdyrko, I. Kovalenko, B. Hertzberg, R. Burtovyy, C. F. Huebner, T. F. Fuller, I. Luzinov, and G. Yushin, "Toward efficient binders for Li-ion battery Si-based anodes: Polyacrylic acid," *ACS Applied Materials and Interfaces*, vol. 2, pp. 3004–3010, Nov. 2010.
- [95] M. Yoo, C. W. Frank, S. Mori, and S. Yamaguchi, "Effect of poly(vinylidene fluoride) binder crystallinity and graphite structure on the mechanical strength of the composite anode in a lithium ion battery," *Polymer*, vol. 44, pp. 4197–4204, June 2003.
- [96] M. Yoo, C. W. Frank, S. Mori, and S. Yamaguchi, "Interaction of poly(vinylidene fluoride) with graphite particles. 2. Effect of solvent evaporation kinetics and chemical properties of PVDF on the surface morphology of a composite film and its relation to electrochemical performance," *Chemistry of Materials*, vol. 16, no. 10, pp. 1945–1953, 2004.
- [97] J. Guo, W. Zhai, Q. Sun, Q. Ai, J. Li, J. Cheng, L. Dai, and L. Ci, "Facilely tunable coreshell Si@SiOx nanostructures prepared in aqueous solution for lithium ion battery anode," *Electrochimica Acta*, vol. 342, p. 136068, May 2020.
- [98] E. McCafferty and J. P. Wightman, "Determination of the concentration of surface hydroxyl groups on metal oxide films by a quantitative XPS method," *Surface and Interface Analysis*, vol. 26, no. 8, pp. 549–564, 1998.
- [99] L. T. Zhuravlev, "Concentration of hydroxyl groups on the surface of amorphous silicas," *Langmuir*, vol. 3, pp. 316–318, May 1987.
- [100] M. J. Chon, V. A. Sethuraman, A. McCormick, V. Srinivasan, and P. R. Guduru, "Real-Time Measurement of Stress and Damage Evolution during Initial Lithiation of Crystalline Silicon," *Physical Review Letters*, vol. 107, p. 045503, July 2011.
- [101] S. Rezazadeh-Kalehbasti, L. W. Liu, H. J. Maris, and P. R. Guduru, "In Situ Measurement of Phase Boundary Kinetics during Initial Lithiation of Crystalline Silicon through Picosecond Ultrasonics," *Experimental Mechanics*, vol. 59, pp. 681–689, June 2019.

- [102] I. Yoon, S. Jurng, D. P. Abraham, B. L. Lucht, and P. R. Guduru, "Measurement of mechanical and fracture properties of solid electrolyte interphase on lithium metal anodes in lithium ion batteries," *Energy Storage Materials*, vol. 25, pp. 296–304, Mar. 2020.
- [103] E. P. O'Brien, T. C. Ward, S. Guo, and D. A. Dillard, "Strain energy release rates of a pressure sensitive adhesive measured by the shaft-loaded blister test," *The Journal of Adhesion*, vol. 79, pp. 69–97, Jan. 2003.
- [104] C. Sauter, R. Zahn, and V. Wood, "Understanding Electrolyte Infilling of Lithium Ion Batteries," *Journal of The Electrochemical Society*, vol. 167, p. 100546, Jan. 2020.
- [105] J. Chopin, D. Vella, and A. Boudaoud, "The liquid blister test," *Proceedings of the Royal Society A: Mathematical, Physical and Engineering Sciences*, vol. 464, pp. 2887–2906, Nov. 2008.
- [106] W. R. Liu, M. H. Yang, H. C. Wu, S. M. Chiao, and N. L. Wu, "Enhanced cycle life of Si anode for Li-ion batteries by using modified elastomeric binder," *Electrochemical and Solid-State Letters*, vol. 8, p. A100, Dec. 2005.
- [107] H.-K. Park, B.-S. Kong, and E.-S. Oh, "Effect of high adhesive polyvinyl alcohol binder on the anodes of lithium ion batteries," *Electrochemistry Communications*, vol. 13, pp. 1051–1053, Oct. 2011.
- [108] E. Kröner, "Allgemeine Kontinuumstheorie der Versetzungen und Eigenspannungen," *Archive for Rational Mechanics and Analysis*, vol. 4, pp. 273–334, Jan. 1959.
- [109] E. H. Lee, "Elastic-plastic deformation at finite strains," *Journal of Applied Mechanics, Transactions ASME*, vol. 36, pp. 1–6, Mar. 1964.
- [110] L. Anand, O. Aslan, and S. A. Chester, "A large-deformation gradient theory for elastic-plastic materials: Strain softening and regularization of shear bands," *International Journal of Plasticity*, vol. 30–31, pp. 116–143, 2012.
- [111] L. Baggetto, J. K. Keum, J. F. Browning, and G. M. Veith, "Germanium as negative electrode material for sodium-ion batteries," *Electrochemistry Communications*, vol. 34, pp. 41–44, 2013.
- [112] S. P. Lele and L. Anand, "A large-deformation strain-gradient theory for isotropic viscoplastic materials," *International Journal of Plasticity*, vol. 25, pp. 420–453, Mar. 2009.
- [113] V. A. Sethuraman, M. J. Chon, M. Shimshak, N. Van Winkle, and P. R. Guduru, "In situ measurement of biaxial modulus of Si anode for Li-ion batteries," *Electrochemistry Communications*, vol. 12, pp. 1614–1617, Aug. 2010.
- [114] S. A. Chester and L. Anand, "A coupled theory of fluid permeation and large deformations for elastomeric materials," *Journal of the Mechanics and Physics of Solids*, vol. 58, pp. 1879–1906, Nov. 2010.

- [115] S. A. Chester, C. V. Di Leo, and L. Anand, "A finite element implementation of a coupled diffusion-deformation theory for elastomeric gels," *International Journal of Solids and Structures*, vol. 52, pp. 1–18, Jan. 2015.
- [116] N. Legrand, S. Raël, B. Knosp, M. Hinaje, P. Desprez, and F. Lapicque, "Including double-layer capacitance in lithium-ion battery mathematical models," *Journal of Power Sources*, vol. 251, pp. 370–378, Apr. 2014.
- [117] S. A. Chester and L. Anand, "A thermo-mechanically coupled theory for fluid permeation in elastomeric materials: Application to thermally responsive gels," *Journal of the Mechanics and Physics of Solids*, vol. 59, pp. 1978–2006, Oct. 2011.
- [118] P. R. Abel, Y. M. Lin, T. De Souza, C. Y. Chou, A. Gupta, J. B. Goodenough, G. S. Hwang, A. Heller, and C. B. Mullins, "Nanocolumnar germanium thin films as a high-rate sodium-ion battery anode material," *Journal of Physical Chemistry C*, vol. 117, no. 37, pp. 18885–18890, 2013.
- [119] C. D. Fincher, Y. Zhang, G. M. Pharr, and M. Pharr, "Elastic and Plastic Characteristics of Sodium Metal," *ACS Applied Energy Materials*, vol. 3, no. 2, pp. 1759–1767, 2020.
- [120] R. Tripuraneni and S. P. V. Nadimpalli, "Real-Time Measurement of Biaxial Modulus of Ge Anode for Li Ion Batteries," in *XXIV ICTAM*, 21-26 August 2016, Montreal, Canada, 2016.
- [121] W. Zhang, F. Zhang, F. Ming, and H. N. Alshareef, "Sodium-ion battery anodes: Status and future trends," *EnergyChem*, vol. 1, p. 100012, Sept. 2019.
- [122] N. Jayaprakash, S. K. Das, and L. A. Archer, "The rechargeable aluminum-ion battery," *Chemical Communications*, vol. 47, pp. 12610–12612, Nov. 2011.
- [123] J. C. Burns, N. N. Sinha, D. J. Coyle, G. Jain, C. M. VanElzen, W. M. Lamanna, A. Xiao, E. Scott, J. P. Gardner, and J. R. Dahn, "The Impact of Varying the Concentration of Vinylene Carbonate Electrolyte Additive in Wound Li-Ion Cells," *Journal of The Electrochemical Society*, vol. 159, pp. A85–A90, Dec. 2011.
- [124] R. D. Deshpande, P. Ridgway, Y. Fu, W. Zhang, J. Cai, and V. Battaglia, "The Limited Effect of VC in Graphite/NMC Cells," *Journal of The Electrochemical Society*, vol. 162, pp. A330–A338, Dec. 2015.
- [125] J. Xu, R. D. Deshpande, J. Pan, Y.-T. Cheng, and V. S. Battaglia, "Electrode Side Reactions, Capacity Loss and Mechanical Degradation in Lithium-Ion Batteries," *Journal of The Electrochemical Society*, vol. 162, no. 10, pp. A2026–A2035, 2015.
- [126] R. Deshpande, M. Verbrugge, Y.-T. Cheng, J. Wang, and P. Liu, "Battery Cycle Life Prediction with Coupled Chemical Degradation and Fatigue Mechanics," *Journal of The Electrochemical Society*, vol. 159, pp. A1730–A1738, Aug. 2012.
- [127] R. Mogensen, D. Brandell, and R. Younesi, "Solubility of the Solid Electrolyte Interphase (SEI) in Sodium Ion Batteries," *ACS Energy Letters*, vol. 1, pp. 1173–1178, Dec. 2016.